Lagrangian coherent motions to track particle trajectories in turbulent flows

Ali Rahimi Khojasteh

UNIVERSITÉ DE RENNES 1

THÈSE DE DOCTORAT DE

L'UNIVERSITÉ DE RENNES 1

ÉCOLE DOCTORALE N° 601
Mathématiques et Sciences et Technologies de l'Information et de la Communication
Spécialité : *«Signal, Image, Vision»*

Par

Ali Rahimi Khojasteh

Lagrangian coherent motions to track particle trajectories in turbulent flows

Thèse présentée et soutenue le 26 avril 2022
Unité de recherche : French National Institute for Agriculture, Food, and Environment (INRAE)

Rapporteurs avant soutenance :

Christian J. Kähler	Professor, Universität der Bundeswehr München
Andrea Sciacchitano	Assistant Professor, Technische Universiteit Delft

Composition du Jury :

Examinateurs :	Andreas Schröder	Professor, Brandenburg University of Technology, DLR
	Mickaël Bourgoin	Research Director, Ecole Normale Supérieure de Lyon, CNRS
	Thomas Corpetti	Research Director, LETG, CNRS
	Katharina Zähringer	Group leader, Otto-von-Guericke University of Magdeburg
Dir. de thèse :	Dominique Heitz	Senior research scientist, INRAE

Invité(s) :

Yang Yin	Co-supervisor, research engineer, INRAE

RESUME EN FRANÇAIS

Les progrès récents en vélocimétrie par le suivi tridimensionnel et résolu en temps de particules (4D-PTV) permettent d'explorer la turbulence lagrangienne le long des trajectoires des particules. La présente étude vise à examiner les améliorations possibles des estimations du mouvement lagrangien en ajoutant des éléments physiques significatifs dans le processus de mesure 4D-PTV. Les méthodes telles que Shake-The-box (STB [1]) et Kernelized Lagrangian Particle Tracking (KLPT [2]) reposent sur quatre étapes principales : la reconstruction des particules, l'initialisation, la prédiction et l'optimisation. Les positions 3D reconstruites doivent être initialisées correctement avant le début du processus de prédiction. Ensuite, les positions prédites sont transmises à l'étape d'optimisation et de raffinement de la position, connue sous le nom de "shaking" dans STB. Il convient de noter que ce processus d'optimisation tente de rechercher une position réelle candidate très proche de la position prédite. Si une prédiction erronée se produit, peu importe le nombre de fois que le processus d'optimisation est effectué, la position réelle n'est pas atteinte. D'où l'importance de produire une initialisation appropriée et des prédictions précises. Dans la présente étude, nous nous sommes principalement concentrés sur l'amélioration de la robustesse et de la précision de l'initialisation et de la prédiction, pour une densité élevée de particules (suivant la tendance observée dans la figure 1.4) et des mouvements d'écoulements complexes.

Actuellement, les étapes d'initialisation et de prédiction des techniques PTV se concentrent sur une seule particule, alors que cette particule n'agit pas seule dans le champ d'écoulement. Nous proposons d'améliorer cela en différenciant localement les mouvements cohérents et non cohérents des particules voisines d'une particule considérée. Pour ce faire, nous utilisons le concept de structures cohérentes lagrangiennes (LCS pour en anglais Lagrangian Coherent Structures [3]), pour améliorer l'initialisation ainsi que la précision de la prédiction. Les crêtes des LCS divisent le champ d'écoulement en différentes régions cohérentes agissant comme un squelette de l'écoulement. Grâce à des approches de segmentation de particules, nous pouvons déterminer les crêtes des LCS et qualifier les trajectoires voisines comme cohérentes ou non cohérentes. L'exposant de Lyapunov en temps fini (FTLE [4]) est un paramètre bien établi que nous utilisons lo-

calement sur les trajectoires lagrangiennes éparses. Avec cette approche, nous pouvons déterminer les particules cohérentes voisines de la particule considérée, pour prédire son comportement avec précision et éviter les erreurs d'estimation.

Aperçu des chapitres

Nous décrivons au chapitre 5 le développement de la nouvelle technique d'initialisation de trajectoire lagrangienne et son principe de fonctionnement basé sur les trajectoires voisines cohérentes. De plus, les évaluations de la technique proposée par rapport aux études récentes disponibles sont discutées. Le chapitre 6 présente un aperçu des fonctions de prédiction du point de vue de la minimisation. Nous décrivons une forme générique de la fonction de prédiction, indépendante du cas et de Reynolds. La fonction proposée (c'est-à-dire le prédicteur cohérent) a été évalué de manière détaillée pour trois cas tests synthétiques de simulation numérique directe (DNS). Nous avons également effectué des simulations de Monte Carlo pour quantifier le niveau d'incertitude des fonctions prédicteurs. Le prédicteur cohérent a été étudié avec une expérience de mesure 4D-PTV dans le sillage d'un cylindre lisse à un nombre de Reynolds égal à 3900. Les statistiques lagrangiennes et eulériennes ont pu être calculées dans la zone de similitude du sillage. Enfin, dans le chapitre 8, nous étudions l'application du concept de cohérence lagrangienne dans les expériences classiques de PIV.

Principes fondamentaux de la vélocimétrie tridimensionnelle par le suivi de particules

Dans le chapitre 2, nous donnons tout d'abord un aperçu général du processus 4D-PTV en présentant son principe de fonctionnement basé sur quatre étapes majeures. Le chapitre 3 traite de la manière de calculer une LCS et donne un aperçu des approches actuelles pour calculer les particules voisines cohérentes spatialement et temporellement, à partir de trajectoires lagrangiennes éparses. Les détails des cas d'essai expérimentaux et numériques utilisés dans cette étude sont discutés au chapitre 4. Un nombre total de sept cas d'essai, dont trois expériences, trois simulations synthétiques DNS et une source de données provenant du 1er défi LPT challenge [5], ont été utilisés dans cette thèse pour obtenir des résultats concluants pour les techniques proposées.

Trajectoire cohérente et Initialisation

Au chapitre 5, nous avons proposé une nouvelle technique d'initialisation à quatre (ou plusieurs) images en exploitant la cohérence temporelle et spatiale locale des trajectoires voisines. La technique que nous proposons se nomme LCTI pour "Lagrangian Coherent Track Initialisation" ([6]). L'idée est de contraindre la trajectoire possible d'une particule par les mouvements cohérents limités par les crêtes des LCS, sachant que les trajectoires lagrangiennes ne traversent pas ces crêtes. Il a été constaté que le processus 4D-PTV échoue si le nombre de trajectoires vraies initialisées n'est pas suffisant, en particulier dans les dynamiques d'écoulement complexes. Nous avons montré que les techniques d'initialisation multi-frames perdent leur efficacité si les caractéristiques de l'écoulement, l'échelle temporelle, la concentration de particules et le rapport de bruit, commencent à augmenter. Trois cas d'essai, l'écoulement de sillage de cylindre, l'impact de jet, et l'écoulement de sillage limité par la paroi, ont été employés pour évaluer qualitativement et quantitativement la performance de la méthode proposée. Dans l'étude synthétique du sillage derrière un cylindre, LCTI a montré un comportement robuste et précis en détectant plus de trajectoires vraies avec moins de trajectoires non suivies et de mauvaises pistes. La technique d'initialisation proposée a également été examinée dans une expérience 4D-PTV d'un jet impactant. Un tel cas contient de nombreuses structures d'écoulements complexes depuis le moment où les particules quittent la buse jusqu'à ce qu'elles rebondissent sur la paroi solide. Seules les positions reconstruites ont été utilisées comme entrée pour l'évaluation de cette expérience. LCTI (sans prédiction ni optimisation supplémentaires) a été capable de reconstruire les trajectoires. Des structures complexes d'écoulement par impact de jet, telles que l'anneau tourbillonnaire autour du jet et les tourbillons secondaires, ont été observés à partir de la reconstruction LCTI. Nous avons conclu ce chapitre en notant que la notion de LCS peut aider l'algorithme de suivi à suivre des structures cohérentes même en cas de gradient de vitesse élevé et de dynamique 3D complexe.

Prédiction de la position des particules

Dans le chapitre 6, nous avons montré que les fonctions prédicteurs récentes en 4D-PTV souffrent d'un manque d'informations pour prédire les positions des particules dans les régions à fort gradient de vitesse. Le problème est que ces fonctions se basent uniquement sur l'historique des particules comme seul signal pour estimer la position de la par-

ticule au prochain pas de temps. Dans l'esprit de l'utilisation des mouvements cohérents, une nouvelle fonction de prédiction a été introduite, à savoir le prédicteur cohérent. À cette fin, nous avons d'abord conçu une fonction de coût basée sur trois termes traitant de l'historique, de la vitesse cohérente et de l'accélération cohérente. D'après l'étude synthétique, la fonction de coût proposée a surpassé les fonctions de prédiction récentes avec une erreur de biais plus faible, en particulier dans les régions complexes. Pour quantifier le niveau d'incertitude de la fonction proposée, nous avons effectué des simulations de Monte Carlo. Le prédicteur cohérent a montré une distribution d'incertitude de sortie étroite par rapport au filtre de Wiener et aux prédicteurs polynomiaux de troisième ordre. Les performances des fonctions prédicteurs mentionnées ont été examinées dans une expérience de mesure 4D-PTV dans le sillage d'un cylindre. Les positions prédites par le prédicteur cohérent ont montré une déviation minimale par rapport aux positions estimées par les autres fonctions prédicteurs. Suite aux études synthétiques et expérimentales, on peut dire que le processus de prédiction devient plus précis avec moins d'incertitude lorsque l'on ajoute des valeurs cohérentes de vitesse et d'accélération.

Il est intéressant d'étendre la fonction de coût proposée au chapitre 6 à une forme de prédiction générique. Nous avons donc introduit une fonction de coût non dimensionnelle avec des termes pondérés. Les termes de position, de vitesse et d'accélération ont été adimensionnés sur la base des échelles intégrales turbulentes. De cette manière, il est possible de minimiser une fonction de coût générique applicable à divers écoulements turbulents. Nous avons constaté que l'incertitude de mesure a un impact direct sur la solution optimale de la fonction de coût du prédicteur minimisé. Nous avons utilisé deux cas de turbulences synthétiques, une turbulence isotrope homogène 2D (HIT) et l'écoulement dans le sillage d'un cylindre, avec les mêmes niveaux d'incertitude de mesure. La solution optimale de la fonction de coût pour les deux cas a montré des configurations de pondération similaires. Cela suggère que les paramètres de pondération peuvent être modélisés comme une fonction des incertitudes de mesure. Nous avons donc réalisé d'autres études paramétriques et quantifié un modèle qui tient compte des incertitudes de mesure pour concevoir la fonction de coût optimale.

Les algorithmes de mesure 4D-PTV sont finalement conçus pour explorer la physique des structures cohérentes, les statistiques et les caractéristiques fondamentales de la turbulence dans un cadre lagrangien. Il est intéressant de noter que les récentes avancées dans les expériences lagrangiennes ont ouvert de nouvelles possibilités pour étudier les relations turbulentes fondamentales dans des expériences réelles. Par conséquent, nous avons effec-

tué une analyse statistique lagrangienne de l'expérience d'écoulement de sillage dans le chapitre 6. Nous avons stationnarisé les trajectoires lagrangiennes anisotropes sur la base du flux moyen et de l'écart type local de la vitesse. L'objectif était d'obtenir des caractéristiques turbulentes et de les comparer aux propriétés autosimilaires de l'écoulement de sillage. La décroissance calculée du taux de dissipation eulérien obtenu dans la partie avale d'un écoulement de sillage est conforme avec les résultats des études fondamentales menées pour un écoulement turbulent en cisaillement libre. Nous avons observé des augmentations de l'échelle de longueur turbulente eulérienne, ce qui est cohérent avec l'augmentation constante de la taille du sillage. Plus en aval dans le sillage, la fonction de structure lagrangienne d'ordre deux a montré un bon accord avec les relations fondamentales. Nous avons calculé la constante universelle lagrangienne C_0 pour la dynamique de la portée inertielle. Cette constante dans le cadre lagrangien joue un rôle similaire à celui de la constante de Kolmogorov dans le cadre eulérien. En résumé, nous avons fourni et validé les caractéristiques statistiques turbulentes eulériennes/lagrangiennes de l'écoulement de sillage obtenues expérimentalement par la mesure 4D-PTV.

Application de la cohérence lagrangienne à la PIV

Dans le chapitre 8 nous avons examiné la possibilité d'ajuster la fenêtre d'interrogation en fonction des mouvements cohérents locaux. Les crêtes LCS, également connues sous le nom de squelette de l'écoulement, divisent le champ d'écoulement local en régions de mouvements cohérents. Nous avons façonné la fenêtre d'interrogation pour calculer les champs vectoriels basés uniquement sur les mouvements cohérents. Nous avons examiné localement et globalement la méthode proposée à l'aide d'une simulation synthétique de PIV 2D HIT et de mesures expérimentals de PIV 2D dans l'écoulement de sillage d'un cylindre circulaire. L'évaluation synthétique locale a révélé que la fenêtre d'interrogation ajustable améliore les erreurs de vitesse RMS, angulaire et de vorticité dans les cas classiques tels que les écoulements en vortex, cisaillés et au niveau des points selles. L'amélioration maximale concerne l'estimation de l'erreur angulaire, qui nécessite une fenêtre d'interrogation précise. Les résultats globaux ont également montré des améliorations par rapport aux fenêtres d'interrogation carrées classiques. La technique proposée a été étudiée dans une expérience de PIV 2D. Nous avons observé des améliorations, en particulier dans les régions avec des tourbillons de petite échelle. Les résultats de ce chapitre suggèrent que l'ajustement de la fenêtre d'interrogation basée sur les mouvements cohérents locaux conduit à une meilleure estimation du champ vitesse.

Table of Contents

Chapter 1

Introduction

Humans have created countless works of art to interpret nature through observation and visualisation. In fluid mechanics, we can refer to Leonardo da Vinci's artwork pieces, all dated from 1452 to 1519. In one of his works, for example, the artist sketched how flow behaves downstream of a wake, as shown in Figure 1.1. The flow became visible by drawing hairlike streams with two motion categories, passing behind obstacles (see the review by Marusic and Broomhall [7]). It was an astounding qualitative visualisation that sparked detailed discussions on Leonardo's thinking. Taylor [8] suggested that Leonardo "seems to be thinking about ways to separate flow into steady and turbulent components," and Lumley [9] concluded that the text "seems to be a clear prefiguring of Reynolds decomposition." All these discussions reveal that scientists have been trying to qualify and quantify turbulent flows in nature for a long time. Essentially, better qualification and quantification are necessary for a better interpretation of turbulent flows.

Thinking about quantifying fluid properties, velocity for example, we need to pick fluid elements and measure their displacements for a specific time step. The fundamental difficulty is that the flow field medium is transparent (i.e., invisible). To this end, scientists have been attempting to introduce visible tracer fluid particles or smokes along with the flow field to observe the motion. In fact, there is no term called fluid particles, and we assume that the observed motion is representing the flow dynamics. Ludwig Prandtl carried out one of the earliest flow visualisation experiments using tracer particles in the late 1920s. He succeeded in qualitatively studying unsteady separated flows behind objects in an open surface water channel. In this work, Prandtl integrated single recordings with 20 frames per second acquisition frequency to yield particle streak images. Figure 1.2.ab visualises one of Prandtl's works on vortex creation, introduced by moving an airfoil from right to left [10], [11]. Around the 1980s, researchers were capable of analysing recorded videos, thanks to the filming industry improvements, to obtain quantitative velocity fields. The process was able to study around 10-20 frames using cross-correlation based techniques. Since then, scientists have started visualising the flow problems using

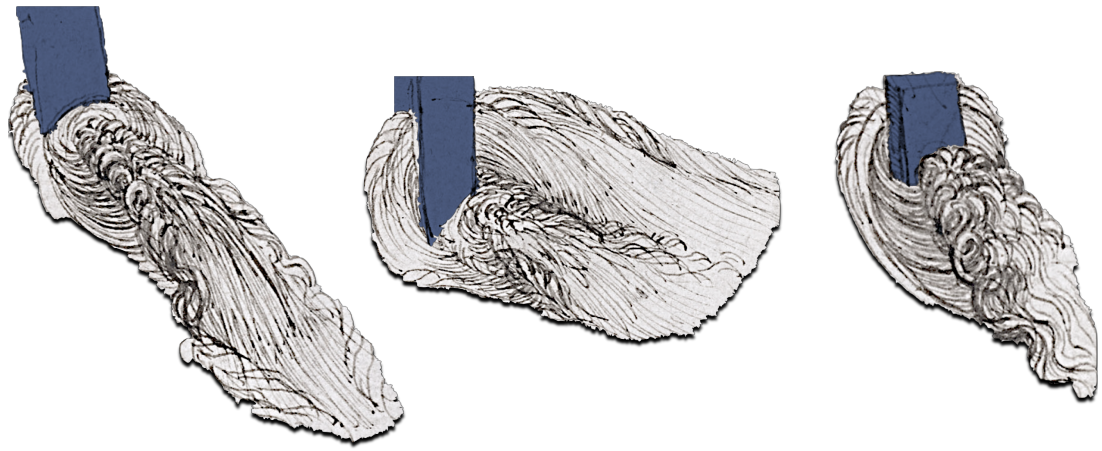

Figure 1.1 – Illustrations of the wake flow by Leonardo da Vinci (adapted from the Sheet RCIN 912579r. Royal Collection Trust, Copyright Her Majesty Queen).

digital facilities. Visualisation can be two-dimensional (2D) or three-dimensional (3D), mainly focusing on qualitative representations. For example, steam injections over a car shape in a form of streamlines that can visualise the stream directions. However, we do not know the velocity magnitudes from the streamlines unless we estimate the relative magnitudes roughly based on the mass conversation hypothesis, which might result in highly uncertain measurement. These visualisations can represent valuable qualitative information, but it becomes complicated (somehow impossible) to estimate quantitative parameters from visualisation in complex flow motions such as 3D unsteady flows. Due to this reason, we need a quantitative approach for complex flows. In the Lagrangian framework, a very early example of particle tracking velocimetry (PTV), additionally known as Lagrangian Particle Tracking (LPT), was done by Utami and Uemo [12] using the double-exposed image of particles. Utami and Uemo [12] tracked randomly located split trajectories with a length of two time steps in a low particle concentration setup over the boundary layer flow. Their tracking experiment failed to reconstruct close to the wall motions since it was challenging to have enough resolution to cover the whole velocity range. Moreover, their 2D measurements were unable to describe the 3D features of the flow. In the 1990s, Digital Particle Image Velocimetry (DPIV [13]) was introduced using CCD cameras. Even Prandtl's recordings can now be recovered using quantitative DPIV computations, as shown in figure 1.2.c [10]. For simplicity, the "D (stands for digital)" letter from DPIV was omitted, and thenceforth the method was denoted as PIV. The

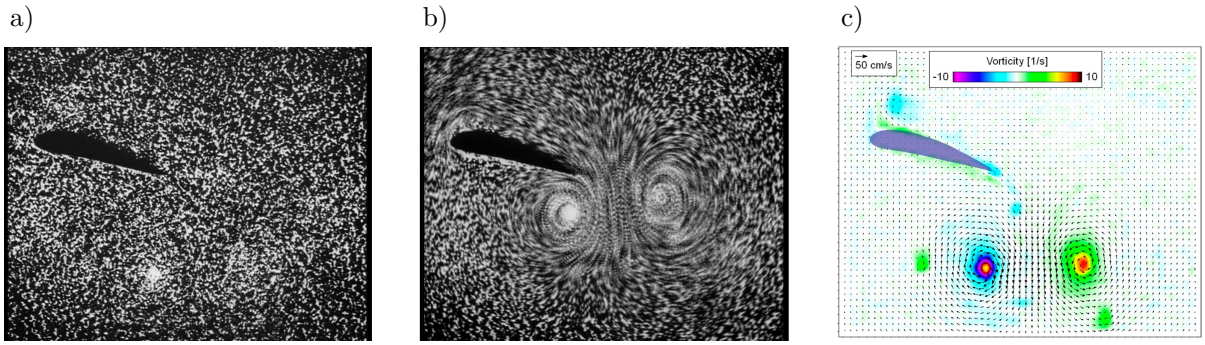

Figure 1.2 – Prandtl's recording of the vortex behind an airfoil translated from right to left. (a) Single frame of the recorded movie. (b) Particle streak image obtained from an ensemble of five continuous frames. (c) Recovered velocity and vorticity fields using DPIV (reprinted from Willert and Kompenhans [11]).

objective of using PIV is to obtain both statistics and instantaneous velocity distributions. With the advances of PIV, it is now possible to measure volumetric regions [14]. PIV mainly gives vector fields on 2D/3D regions with better spatially resolved visualisation than smoke visualisation. PIV marks the fluid with particles and then measures their motions. So the natural trend is to use small particles as marked signatures of flow and track the motion.

1.1 Flow measurement from a single point to volumetric velocimetry

There is a development of spatial components in the evolution of flow measurement techniques. The evolution started from Laser Doppler Anemometry (LDA/LDV) and hot wire anemometry (HWA), which are typically pointwise measurements. LDV is well established in capturing high intensity fluctuations, and HWA is capable of detecting low intensity turbulent flows with high temporal resolution [16]. However, such techniques are only sufficient for discrete flow measurements. To capture flow motions on 2D slices, planar two-component (2D2D) PIV and stereo (3D2C) measurements were introduced by utilising multi camera setups. Measurement of the third spatial component was introduced in 3D-PTV techniques [17]. This was the first volumetric velocimetry technique that succeeded in tracking a small number of Lagrangian particles. Over two decades after the

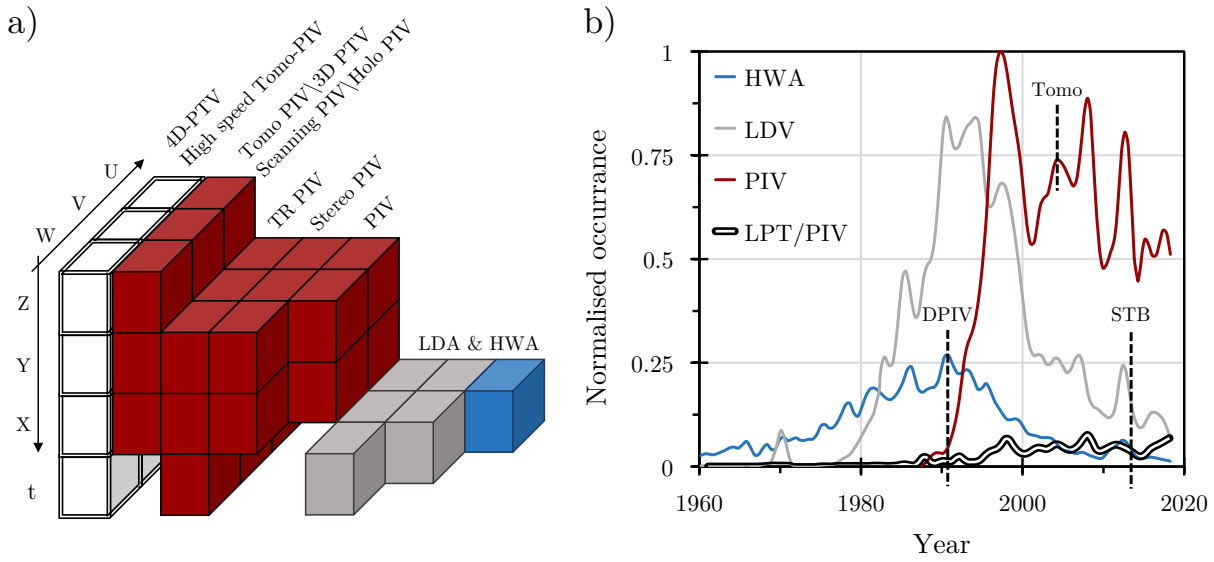

Figure 1.3 – Evolution of the velocimetry techniques. (a) Spatial and temporal measured components of laser velocimetry techniques (adapted from Scarano [15]). (b) The appearance of experiments using the HWA, LDV, PIV, and PTV/LPT measurement techniques mentioned in Google Books between 1960 and 2019 (adapted from Westerweel et al. [16]).

first 3D-PTV experiment, Tomographic PIV (known as Tomo-PIV) introduced by Elsinga et al. [14], became a turning point in history of the volumetric velocimetry techniques. This evolution from a pointwise technique to a fully volumetric laser velocimetry technique has been shown in Figure 1.3.a. In practice, Tomo-PIV starts from voxels to make dense object reconstruction by cross-correlating in 3D voxels to obtain the 3D Cartesian velocity fields. However, it is computationally intensive at reconstruction and correlation steps. The filtering associated with the window limits the Tomo-PIV spatial resolution. The Tomo-PIV concept became hybridised by Novara and Scarano [18] in a technique called Tomo-PTV. This technique still utilises voxels to reconstruct the object by computing sparse particle tracks, but there is no need to have Eulerian domain discretisation in individual voxels. So the data is only stored if a particle exists. Some studies also used spatial information to produce pressure based on the momentum equation [19].

A study from Westerweel et al. [16] showed that the number of PIV experiments jumped significantly compared with HWA and LDV measurement techniques since 1980. Figure 1.3.b shows the number of mentions of velocimetry techniques in Google Books until 2019. It can be emphasised that PIV has become the dominant velocimetry technique in experimental fluid mechanics since mid 1990s. Accordingly, Tomo-PIV outperformed

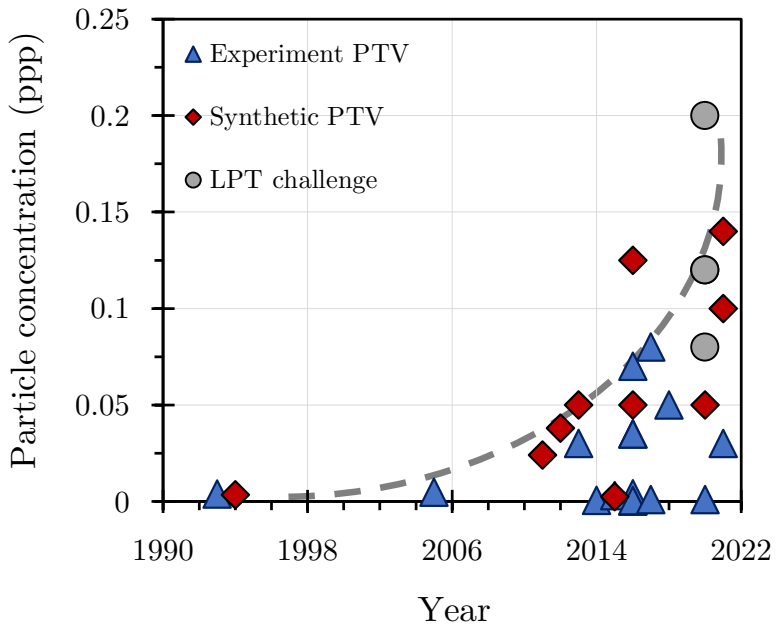

Figure 1.4 – Evolution of spatial resolution (ppp) improvements in PTV techniques. The mentioned studies are listed in table 1.1. Grey dashed line shows the growing trend in higher particle concentration cases.

classic 3D-PTV techniques in volumetric velocimetry [16]. While classic 3D-PTV techniques were severely limited by the particle image seeding density and image quality, Tomo-PIV succeeded in processing an order of magnitude higher densities from 0.005 to 0.05 particle image per pixel (ppp) with lower noisy reconstruction. The PIV/PTV research community is consistently interested in a measurement technique that is applicable in a variety of problems with highly accurate results [10]. Therefore, techniques tend to improve spatial and temporal accuracies. In 2013, a novel iterative particle reconstruction (IPR) idea introduced by Wieneke [20] substantially improved the performance of PTV techniques. IPR was then followed with predictive tracking functions in the form of a method called Shake-The-Box (STB [1]). STB is a time-resolved three-dimensional particle tracking velocimetry technique (known as 4D-PTV) that tries to predict particle positions and optimise the discrepancy of the predicted position with the recorded images under the process named "Shaking". Such a predictive tracking model pushed spatial and temporal limitations of the classic 3D-PTV techniques. Since then, 4D-PTV surpassed Tomo-PIV with less noisy reconstruction, higher spatial resolution and accuracy, and significantly less computational demand.

One of the main motivations of performing volumetric measurements is to characterise Eulerian/Lagrangian coherent structures, statistics, spatial gradients, and measurement of vorticity dynamics (transport, stretching, tilting) in turbulent flows. To capture the spatial and temporal evolution of turbulent flows in experiments, we need to reach sufficient spatial resolution to resolve coherent structures. The evolution of resolved spatial resolution in PTV techniques are shown in figure 1.4 and table 1.1. Maximum achievable particle image density is drastically improved by two order of magnitude from 0.001 ppp in 1993 [17] to 0.2 ppp in 2020 [5] with less than 0.1 pixel position estimation error.

The other issue that needs to be addressed is the measurement size, which is limited by the imaging facility and the seeding system. Majority of volumetric experiments were performed in a very small volumes (maximum $70 \times 11 \times 41$ mm^3 [40]) where the tracer particles were not more than 1 μm. In general, based on a study from Scarano [41], the higher acquisition frequency leads to the smaller measurement volume mainly because the illumination becomes less powerful. Peak intensity received from a particle is proportional to the amount of illumination energy, camera aperture, particle diameter, depth of the measurement dimensions by assuming that the propagation direction is neglected. Helium filled soap bubbles (HFSB) were introduced because pushing volumetric measurement limits required larger seeding particles, higher particle intensity signals, and appropriate response time [41]. Therefore, volumetric laser velocimetry techniques succeeded to increase the size of measurement from scale of $10 \times 10 \times 10$ cm^3 to large scale of $200 \times 200 \times 200$ cm^3 [42].

1.2 Aim of the thesis

The present study seeks to investigate possible improvements in motion estimations by adding meaningful Lagrangian physics into the velocimetry algorithms. Methods like STB and Kernelized Lagrangian Particle Tracking (KLPT [2]) rely on four major steps, particle reconstruction, initialisation, prediction, and optimisation. The reconstructed 3D positions should be initialised properly before the prediction process starts. Then, the predicted positions are passed to the optimisation step and position refinement, known as "shaking" in STB. It should be noted that the "shaking" process tries to look for a candidate true position very close to the predicted position. This implies that if a misprediction happens, the true position is not achievable no matter how many times we perform the "shaking" process. This explains the importance of producing appropriate

Table 1.1 – Evolution of spatial resolution (ppp) improvements in PTV techniques.

	Method	Contributors	Year	ppp	Type
1	Astigmatism, stereoscopic	Fuchs et al. [21]	2014	0.0005	Experiment
2	Defocusing	Fuchs et al. [22]	2016	0.0001	Experiment
3	IPR	Wieneke [20]	2012	0.0300	Experiment
4	Scanning PTV	Hoyer et al. [23]	2005	0.0047	Experiment
5	STB	Novara et al. [24]	2016	0.0350	Experiment
6	STB	Schanz et al. [1]	2016	0.0350	Experiment
7	Tomo-PTV	Schneiders and Scarano [25]	2016	0.0700	Experiment
8	Tomo-PTV	Fuchs et al. [26]	2016	0.0040	Experiment
9	KLPT	Yang and Heitz [2]	2021	0.0300	Experiment
10	LCTI	Khojasteh et al. [6]	2021	0.0300	Experiment
11	Open-LPT	Tan et al. [27]	2020	0.0010	Experiment
12	STB	Huhn et al. [28]	2018	0.0500	Experiment
13	STB	Huhn et al. [29]	2017	0.0800	Experiment
14	Triangulation	Maas et al. [17]	1993	0.0038	Experiment
15	Triangulation	Shirsath et al. [30]	2015	0.0030	Experiment
16	Triangulation	Kim et al. [31]	2016	0.0003	Experiment
17	Triangulation	Janke et al. [32]	2017	0.0010	Experiment
18	Advanced IPR	Jahn et al. [33]	2021	0.1400	Synthetic
19	DIH-PTV	Toloui and Hong [34]	2015	0.0024	Synthetic
20	IPR	Wieneke [20]	2013	0.0500	Synthetic
21	STB	Schanz et al. [1]	2016	0.1250	Synthetic
22	Stereoscopic	Guezennec et al. [35]	1994	0.0034	Synthetic
23	Stereoscopic ACO	Panday et al. [36]	2011	0.0240	Synthetic
24	Tomo-PTV	Doh et al. [37]	2012	0.0380	Synthetic
25	Triangulation with Tomo	Fuchs et al. [26]	2016	0.0500	Synthetic
26	KLPT	Yang and Heitz [2]	2021	0.1000	Synthetic
27	Open-LPT	Tan et al. [27]	2020	0.0500	Synthetic
28	VT-STB	Schanz et al. [38]	2020	0.2000	LPT challenge
29	KLPT	Yang and Heitz [2]	2021	0.0800	LPT challenge
30	LCTI	Khojasteh et al. [6]	2021	0.1200	LPT challenge
31	LaPIV	Yang and Heitz [39]	2020	0.1200	LPT challenge

initialisation and accurate predictions. We primarily focused on improving the initialisation and prediction robustness and accuracy for high particle density (following the observed trend in figure 1.4) and complex flow motions. We argue that initialisation and prediction steps in PTV techniques focus on a single particle individually, while this single particle is not acting alone in the flow field. We propose to locally differentiate coherent and non-coherent motions of neighbour particles around a single particle position using the concept of Lagrangian Coherent Structures (LCS) to improve the initialisation and prediction accuracies. LCS ridges divide the flow field into different coherent regions, acting as a skeleton of flow. We can determine the LCS ridges with particle segmentation approaches and quantify neighbour trajectories as coherent or non-coherent. Finite-time Lyapunov exponent (FTLE) is a well-established parameter to be employed locally over sparse Lagrangian trajectories. With this approach, we can share the information of coherent particles with each neighbour particle to predict its behaviour accurately and avoid misestimations.

1.3 Outline of the thesis

We present here a study that attempts to improve velocimetry algorithms by using the temporal and spatial coherency of Lagrangian particles. As Lagrangian tracer particles move and behave coherently with their neighbours, we constrained the algorithm to comply with physics-based information. In order to determine local coherent motions of turbulent flows, we utilised LCS over sparse Lagrangian trajectories. In 2D/3D flows, LCS has line/surface ridges separating regions with dynamically different trajectories. Based on LCS ridges, we can quantify coherent and non-coherent neighbour trajectories. Three velocimetry algorithms are discussed in this thesis using the idea of local coherent motions of Lagrangian particles. We demonstrated how the track initialisation techniques in 4D-PTV can become more robust through coherent motions. This idea was then used to improve prediction performance. We also explored how to apply this approach to classic PIV algorithms.

We first provide a general overview of the 4D-PTV process with the introduction of its working principle based on four major steps in Chapter 2. The following Chapter 3 addresses how to compute LCS and gives an overview of the current approaches to compute spatially and temporally coherent neighbour particles from sparse Lagrangian trajectories. Details of experimental and numerical test cases used in this study are discussed in

Chapter 4. A total number of seven test cases including three experiments, three Direct Numerical Simulation (DNS) synthetic simulations, and one out-source data from the 1st LPT challenge [43] were employed in this thesis to reach conclusive results for the proposed approach.

We outline the development of the novel Lagrangian track initialisation technique and its working principle based on coherent neighbour trajectories in Chapter 5. Moreover, the assessments of the proposed technique compared with the recently available studies are discussed. Chapter 6 presents an overview of prediction functions with a minimisation point of view. We outline a generic form of the predictor function, which is case and Reynolds independent. The proposed function (i.e., the coherent predictor) was intensively assessed for three DNS synthetic test cases. We also performed Monte Carlo simulations to quantify the uncertainty level of predictor functions. The coherent predictor was studied with a 4D-PTV experiment of the wake behind a smooth cylinder at a Reynolds number equal to 3900. In Chapter 7, we obtained Lagrangian and Eulerian statistics of the wake flow as a self-similar turbulent case. In Chapter 8, application of the Lagrangian coherency concept in classic PIV experiments is studied. We showed that adjusting the interrogation window based on coherent motions of particles can locally and globally improve the velocity estimation accuracy. In this way, the interrogation window temporally and spatially changes to follow the flow motion instead of being fixed square windows.

Chapter 2

Time-resolved 3D Particle Tracking Velocimetry (4D-PTV)

Recent developments in the Shake-The-Box (STB [1]) approach have led to a renewed attention on time-resolved three-dimensional Particle Tracking Velocimetry (4D-PTV) for the study of turbulent flows. STB introduced a fast and efficient tracking idea based on a particle position prediction step followed by an image space optimisation scheme solved with "Shaking". STB was first initiated and shaped after the Iterative Particle Reconstruction (IPR) concept proposed by Wieneke [20]. The 4D-PTV experiment essentially can be done such as Tomo-PIV by adding tracer particles into the flow. Similarly, we illuminate the volumetric region of interest to record the projections of the tracer particles on multi-camera images. These tracer particles can represent Lagrangian flow motions. If we are able to extract the majority of trajectories of these particles, then we have valuable Lagrangian data of the flow motion. It is desirable to have particles with high concentrations because more particles should lead to better-resolved flow structures. Earlier techniques such as 3D-PTV [17] were severely limited by the seeding density of the experiments. Tomo-PIV introduces spatial smoothening because of using cross-correlation techniques. As mentioned in Chapter 1, the computation demand of Tomo-PIV is considerably high. So it would be desirable to do PTV in high tracer concentrations. This chapter addresses the 4D-PTV working principles, including particle reconstruction, track initialisation, position prediction, and position optimisation.

2.1 4D-PTV working principle

A typical 4D-PTV technique comprises four recursive steps inspired by STB. These steps are particle reconstruction, track initialisation, prediction, and optimisation, as shown in figure 2.1. Particle reconstruction with triangulation is a process that converts multi-view 2D particle images to particle positions in a 3D domain. However, the trian-

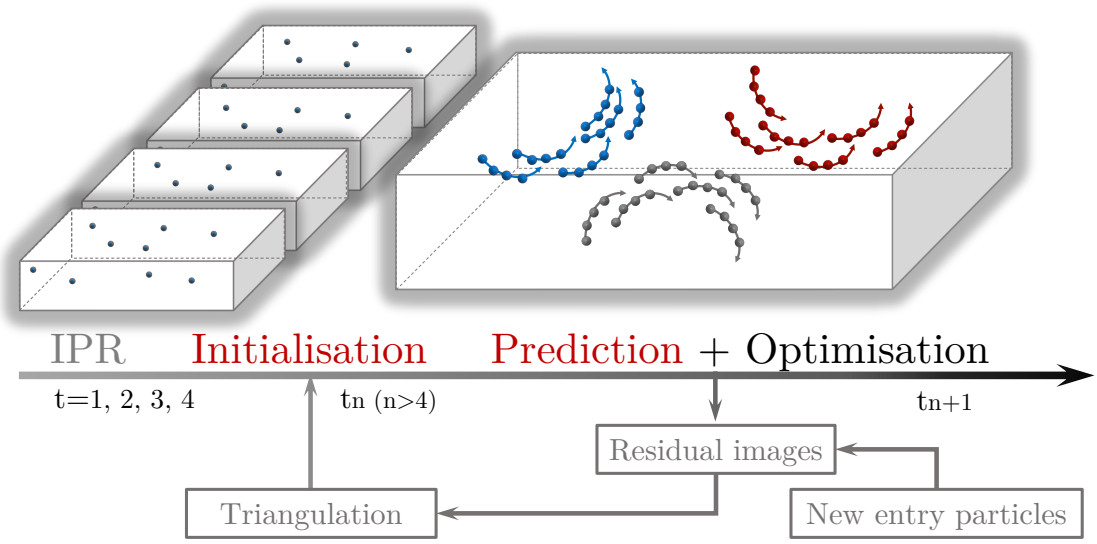

Figure 2.1 – 4D-PTV flowchart starting from particle reconstructions in four frames using IPR [20] followed initialisation, prediction, and optimisation.

gulation only works for sparse particle concentrations lower than 0.001 particles per pixel (ppp). Due to overlapping particles, the number of ghost particles drastically increases in triangulation for higher particle concentrations. Hence, Wieneke [20] proposed IPR with an additional step to overcome the triangulation inaccuracy. In IPR, the triangulation is followed by an iterative optimisation procedure that searches for the best particle position, minimising the intensity discrepancy between the original and the reprojected particle image. The reconstructed 3D positions from IPR are thereafter fed into the initialisation part (see figure 2.1). After the tracklets of the first few frames are built, the prediction function then estimates positions of the next time step (t_{n+1}) using polynomial or Wiener filter predictors [1], [27]. The optimisation takes part from the predicted positions until the optimal positions at t_{n+1} are found. During the prediction-optimisation phase, particles continuously enter the domain. Those new entry trajectories must be fed into the tracked poll; otherwise, there would eventually be no tracks left since all tracked particles would have left the domain for a flow with the main advection. In complex flow motions or with high particle concentrations, some particles lose their trajectories due to optimisation failure. In this scenario, the lost particles are kept in the residual

images, but their tracks will be removed from the tracked poll (see figure 2.1). It is vital to reconstruct those lost particles and build tracklets since an increasing number of lost tracks will lead to the divergence of the tracking algorithm. To this end, the track initialisation attempts to build tracklets for three types of particles, particles in the first four/five frames, new entries, and lost particles. The following sections in this chapter cover details of the mentioned steps in 4D-PTV.

2.2 Particle reconstruction

2.2.1 Particle triangulation

Triangulation is a method to determine 3D particle position from the projection of the particle tracers on multi-camera images. We are searching for a point in 3D space that lines of sights (LOS) of intensity peaks from the camera images to reach one point (as shown in figure 2.2). Worth mentioning that the intensity peaks in each camera are identified by an image processing algorithm called peak finder. A particle position is reconstructed if these lines of sights reach together to a region that is below a certain threshold (i.e., allowed triangulation error). This reconstruction approach is applicable in low particle concentration cases. As a rule of thumb, the allowed triangulation error should be less than one-pixel [20]. However, this approach fails if the number of particles increases by creating more ghost particles as shown in figure 2.2. To reach higher particle concentrations, we start reconstruction from a single camera image and try to find particle intensity correspondences in other camera images [20], [44]. This means that we start from one intensity peak (probably representing a true particle) on camera 0, as shown in figure 2.3. Then we follow the LOS of the red dot (i.e., peak intensity) through the volume to have a line in 3D space (see figure 2.3). After that, the line is back-projected into the camera 1, capturing the same volume of interest from another position. As shown in figure 2.3, the red line in the back projection of the LOS of the target intensity in camera 0. This red line is known as the epipolar line. All the particle peaks around the epipolar line with a specific search radius epsilon (allowed triangulation error) potentially represent images of the same tracer particle (red dot in the camera 0 shows). We use images from other cameras to further filter these potential candidates to precisely determine the 3D intersection points by following the LOSs of candidates. The 3D intersection point is the closest point in space to both cameras' LOSs. Moreover, we can back-project on other

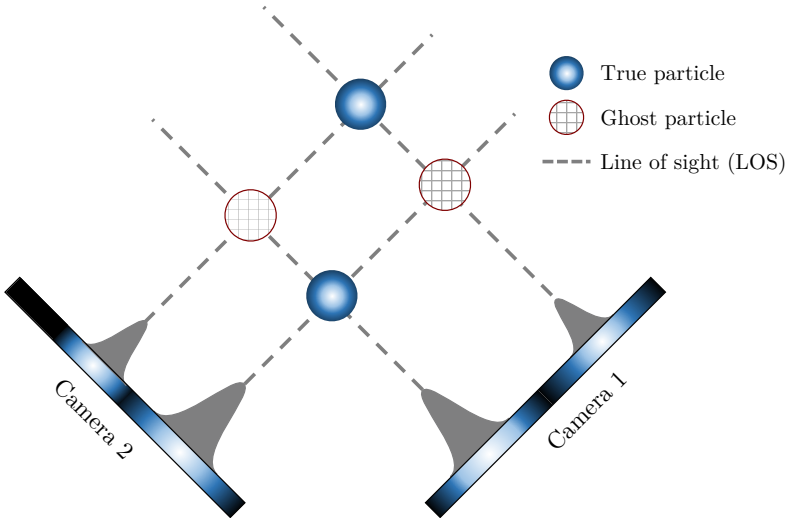

Figure 2.2 – Particle triangulation for a stereo configuration. Grey peaks are recorded by two cameras. The triangulation process gives two true (blue) and ghost (red) reconstructions on the LOS intersections.

cameras (camera 2 and camera 3) from these 3D points. A potential 3D position of a true particle is reconstructed only if there is a peak within a certain threshold (epsilon) around the back-projected point in all cameras.

2.2.2 Ghost particles

Ghost particles result from false particle reconstruction in the triangulation step. Assuming there are two particles in a stereo configuration, we are interested in triangulation. As shown in figure 2.2, two particles are projected in two cameras, producing two peaks on each camera. Ghost particles are created by triangulating these recorded peaks from the camera images to the object space. The triangulation result contains real particles and false reconstructions. The falsely reconstructed particles can get resolved if there is an additional camera by reducing the ambiguity of candidates during the triangulation process. Theoretically, additional cameras are needed if the particle concentration increases. It should be noted that a ghost particle has no coherent motion and decorrelates in time. Moreover, ghost particles have less intensity signals than true particles. It means auxiliary image processing functions in supplement with an additional camera can reduce false reconstructions.

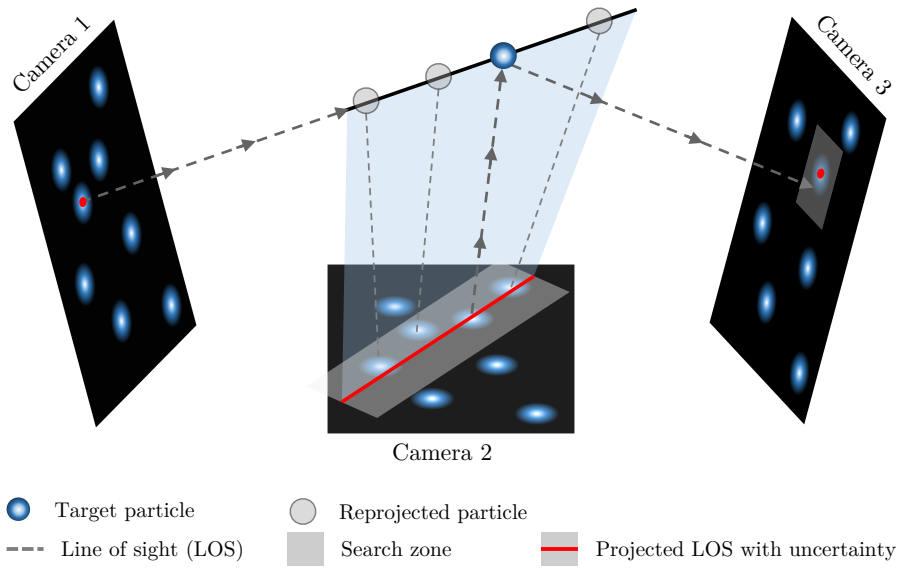

Figure 2.3 – Modified triangulation process, starting from a camera and looking for possible matches on the other cameras.

2.2.3 Iterative Particle Reconstruction (IPR)

Iterative Particle Reconstruction (IPR [20]) is a method that works with two outer and inner loops. The process has five main steps after taking measurement images. The first step is to detect intensity peaks on the captured images using the peak finder function. With the intensity peaks, we can triangulate particles. The triangulated particles are either true or ghost particles. Then we feed those particles into the state vector of IPR. We can perform the position optimisation process "Shaking" with the state vector. In the meantime, we want to remove ghost particles by knowing that typically the intensity of a ghost particle is less than a true particle. So, IPR filters ghost particles by a certain threshold of intensity. As shown in figure 2.4, IPR performs an iterative process by returning to optimisation and shaking steps. This shaking and filtering iteration is called the inner loop (or Shake iteration). The next step is to create the residual images after finishing the inner loop. The residual images are rendered by back-projecting the reconstructed positions using the optical transfer function (OTF). The image model employed in the tracking algorithm is a super-composition of OTF and the camera model. This model translates the 3D positions of particle p at time k (X_p^k) to the image local patch as

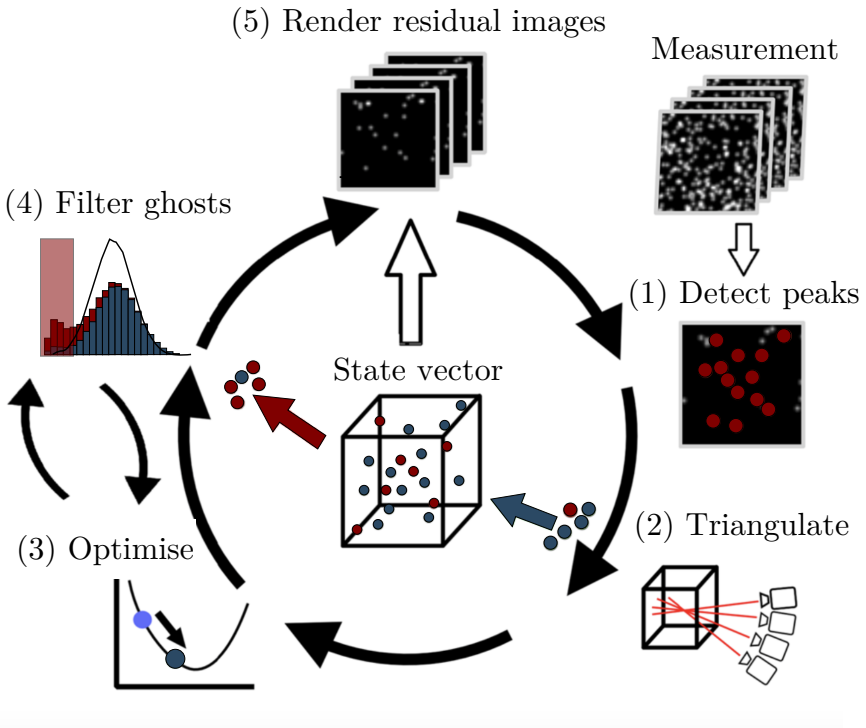

Figure 2.4 – IPR working principle, including two inner and outer loops (reprinted from [20], [33]).

$$I_p^{k,i} = \mathcal{I}_p^i\left(X_p^k, E_p^k\right) + \epsilon_p^k. \tag{2.1}$$

Then we subtract the back-projected intensities with the original recorded images at the same time step. These residual images are considered as the inputs for the next outer loop IPR iteration. The IPR iteration process can be continued multiple times depending on the seeding density. Wieneke [20] showed that IPR is at least as efficient as Tomo-PIV in terms of the fraction of ghost particles for densities up to 0.05 ppp. Although IPR outperforms the Tomo-PIV and classic 3D-PTV techniques for higher particle concentrations, the fraction of ghost particles jumps quickly for densities higher than 0.05 ppp, resulting in the tracking failure. Due to this major issue, Schanz [1] proposed STB technique with additional steps to extend capabilities of IPR in higher densities. STB adds temporal information to reduce the reconstruction complexities of each time step. In this thesis, we employed IPR for all the image-based assessments.

2.3 Track initialisation

4D-PTV methods like STB and Kernelized Lagrangian Particle Tracking (KLPT, [2]) require an appropriate and reliable number of initialised true tracks at every time step. Otherwise, the tracking process fails to reconstruct trajectories for the majority of particles [1], [6]. Such a failure illustrates the importance of implementing a robust multi-frame track initialisation technique to prevent 4D-PTV divergence, particularly in dense and complex situations.

The idea of initialising a possible track in four frames, known as four frame best estimate (4BE), has been widely used in LPT/PTV studies [37], [45]–[48]. Four frame tracking methods with simple nearest neighbour particle matching have been introduced for low density and smooth flow behaviours [47]. However, the nearest neighbour fails to reconstruct true trajectories in high particle concentrations if the length between neighbour particles has the same order of their trajectory displacement within two time steps. New studies recently improved four frame track initialisation performance, including four-frame best estimate (4BE-NNI) method [45] by looking for the nearest neighbours in sequential frames until a unique solution is found or Enhanced Track Initialisation (4BE-ETI) method [46] by looking for all track possibilities with an adjustable search volume (see also [48]). Dou et al. [37] proposed initialising with two nearest candidates in a similar spirit, then kept predicting and particle matching in the next two following time steps (four frames in total) until a unique match is found. Cierpka et al. [49] have shown that the four frame methodology could be extended to multi-frame tracking with the combination of neighbour possibility and temporal prediction in sequential steps. The most straightforward prediction function is the linear predictor that can be calculated from the position difference of every two possible matches. The use of a linear predictor improved the probability of finding true tracks as well as reducing the computation time by having a targeted search volume [49]. Some studies also suggest applying the prior PIV velocity field as a predictor [1], [26], [50]. Although this idea is applicable to 2D and 3D studies, extracting a 3D-PIV velocity field is expensive due to its spatial resolution, uncertainty, and complex experimental issues.

For complex flow motions and experiments with high particle densities, a further step for the track validity check is required to avoid false detection. Guezennec et al. [35] originated this validity check as a self-coherency algorithm with the concept of path coherence. Their technique minimises a penalty function from all possibilities in five frames. In their

study, a possible track is a coherent path if it is a smooth trajectory in position, velocity, acceleration, and rate of acceleration. This spatial and temporal self-consistency penalty function only focuses on a single track behaviour. Recent four frame based techniques also performed similar self-consistency approaches. As an example, [37] checked if the velocity differences between two frames exceed a certain threshold to validate a possible track. With a comparative approach, [45] controlled the acceleration change instead of velocity. Likewise, the self-consistency approach is used in two frame based tracking techniques [51]. These treatments rely on spatial and temporal filtering of the trajectories to avoid false tracks. However, as complex flows often feature high gradient motions, over-smoothing dynamics could lead to a quality degeneration of the reconstructed field. The degeneration problem is that there is no direct learning based on the physics of flow included in the classical four frame schemes, which brings more challenges for complex and high-density flow motions. In Chapter 5, we address a novel initialisation technique based on learning from neighbour trajectories to increase its robustness and efficiency in terms of particle concentration, temporal scale, and noise ratio.

2.4 Position prediction

The initialisation step is followed by the prediction function [52]–[54]. Briefly, it is assumed that particle positions are known for n time steps (four to five). Afterwards, a mathematical prediction function is implemented to estimate particle positions for time-step $n+1$. The predicted particle positions are given to the optimisation process for further corrections. The optimisation can deal with slight deviations between the predicted and true positions. However, the optimisation fails to find the true position if the deviation is large enough to have multi-candidates for a single particle at the next time step. On the other hand, a small prediction error reduces the probability of picking the wrong particle from the surroundings in the optimisation process of 4D-PTV. This shows the importance of having an appropriate prediction in dense and complex motions. In Chapter 6, we address how to predict the particle position at the next time step. We also discuss a novel approach in particle position prediction over space and time based on coherent motions of particles.

2.5 Position optimisation

2.5.1 Shake-the-Box (STB)

STB employs an optimisation process called "Shaking" to correct the predicted positions based on recorded images. The objective of "Shaking" is to find 3D coordinates that minimise the residual image matrices. So the STB cost function can be written as

$$\mathcal{J}\left(X_p^k\right) = \frac{1}{2}\sum_i \left\| I_p^{k,i} - \mathcal{I}_p^i\left(X_p^k . E_p^k\right)\right\|^2 . \tag{2.2}$$

The tracking issue is implicitly embedded in a predictor function to reach the minimised cost function. In the optimisation process, we just optimise the function $\mathcal{J}$ around the predicted position, assuming that the predicted position is close to the true position. So the problem is finding 3D coordinates that best fit recorded image data. STB algorithm can be summarised in two main steps. The first one is IPR. As discussed in section 2.2, IPR is a method that combines triangulations and subsequent position optimisation of the triangulated particles ("shaking" the particles) in an iterative process. By using IPR alone, it is possible to extend the range of processable seeding densities up to 0.05 ppp. The next step in STB is utilizing the temporal information. This step helps to maintain tracks and increases the capability of tracking more densities. STB initialises tracks, and then these particles are extended to the next time step by predicting their following positions (see section 2.4). Since the prediction contains errors due to acceleration and measurement uncertainties, the predicted positions need to be corrected by minimising equation (2.2).

Another problem with triangulation is creation of ghost particles. A ghost particle is a 3D position that is falsely reconstructed. Therefore, we need IPR to improve reconstruction accuracy up to a specific limit. For triangulation, it is often the case that the 3D position of the particle is slightly displaced with respect to the true particle position. This might be due to the measurement noise or peak finder. For example, the peak finder can introduce an error when there is an overlap between two particles, so the peak can not be adequately identified. However, it is possible to optimise the position and the intensity of particles by assessing the 3D position with the camera images. Figure 2.5 shows a schematic view of particle position optimisation by image matching (i.e., "Shaking") for a single camera. In the optimisation process, we back-project the reconstructed position into cameras. Then we can compute the residual image by subtracting the recorded peak

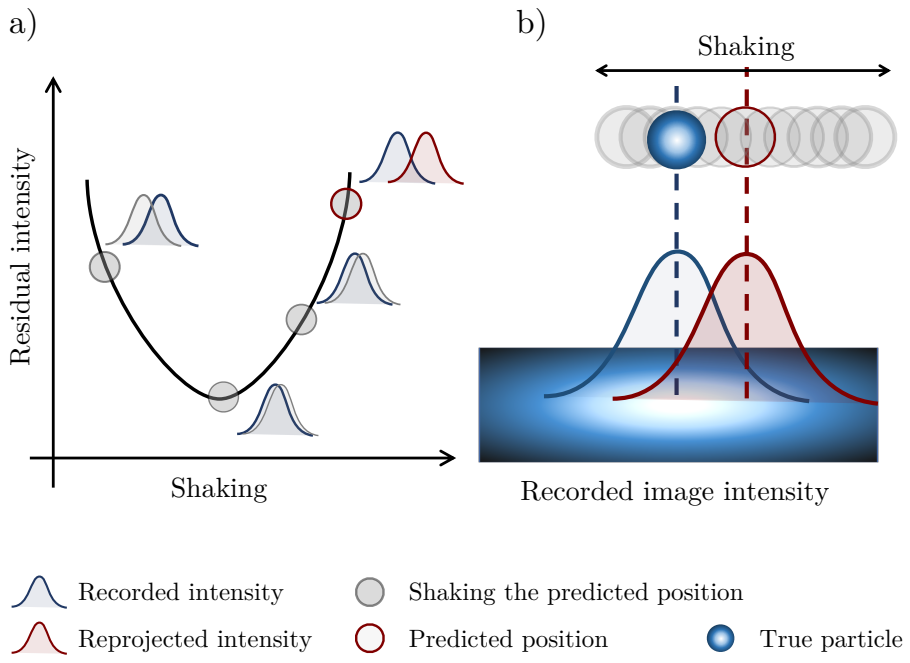

Figure 2.5 – Particle position optimisation. (a) Minimising residual of the recorded and the reprojected intensities. (b) "Shaking" process in a single camera.

(original image) and the back-projected intensity (reprojected image). Due to subtraction, some positive and negative regions will be in the residual image. This residual image should be minimised to reach accurate 3D position estimation. Sum over the magnitude of two peaks (back-projected + recorded) indicates the deviation of two reconstructed and original positions of the particle. This indication can be used as a cost function in the minimisation problem. The more displaced reconstructed particle with respect to the original position will cause more residuals and a higher sum of the magnitudes. In a multi-camera measurement, the cost function should be the sum of the residual images of all the cameras for each particle. Moreover, we have to find the direction in space to move the reconstructed particle to minimise the cost function. This direction is given by the gradient of the cost function (total residuals in figure 2.5.a). Furthermore, the task is to determine the gradient. Wieneke [20] computed the gradient numerically by displacing the reconstructed position in every direction in space and basically sampled the cost function and then moved the particle in the direction of the minimum. Jahn et al. [33] proposed an analytical solution for this optimisation problem. As mentioned earlier, OTF is a process that links the camera images to the 3D space geometries. OTF plays a

crucial role in the whole reconstruction procedure. It is essential to know what the shape of particle images look like. Ideally, the particle should be imaged as a circle. However, it might occur in an experiment that particles are astigmatically distorted, and there is more ellipse shape. This problem should be tackled by the OTF calibration process; otherwise, it will impact the residual optimisation process. In this way, it is possible to optimise the particle's position and simultaneously update the intensity of the optimised position.

Working principle of Shake-The-Box

STB requires a time-resolved series of camera images. STB receives the initialised first four frame images. In the initialisation step, we apply IPR to each of the four frames to reconstruct true and ghost particles. We know that true particles behave in reasonable trajectories, while ghost particles appear in random places. Another point about ghost particles is that they disappear or become uncorrelated in time. STB assumes that particles with low deviations can be true particles to separate them with ghost particles. In the next time step, we can predict the position of particles based on their histories. Thereafter, the deviation between the predicted positions and the original images caused by flow gradients or measurement noises should be optimised in further steps. Similar to the IPR process, STB applies shaking to correct small displacements of predicted particles. Now we end up with a particle distribution (tracked polls) that already has the majority of particles without the necessity of doing the triangulation. This improves the computation cost of the whole tracking process since primary triangulation is only needed for the first few frames. This process continues over all time steps. The same process applies to the new entry particles. As a result, STB extends the IPR capabilities to densities over 0.2 ppp (40 times larger than classic 3D-PTV). Based on synthetic analyses, the accuracy of STB was determined around 0.02 px which is 10 times better than Tomo-PIV with 1/20 computation demand [1].

Variable time step Shake-the-Box

Variable Time step Shake-The-Box (VT-STB) is a novel additional processing loop of the classic STB algorithm, particularly suited for flows with high dynamic velocity ranges. If relative movements of particles are small (frozen motion domains), ghost particles also keep staying in the same region. In such a condition, suppressing ghost particles would be challenging since there are no significant motions of particles to be distinguished from ghost particles. Except for the ghost elimination challenge, projection of close particles in

the camera images creates overlapping intensities in such a region (quiescent flows), which can bias the particle position estimation in the "Shaking" step. On the other hand, the optimisation process can not determine the correct peak when two particle images overlap. To tackle the mentioned challenges, Schanz et al. [38] proposed adaptive timescale selections in VT-STB. The adopted timescale should be optimal for different dynamic regions. For example, for the cylinder wake flow case, the flow motion outside the cylinder is relatively higher than inside the wake. In such a scenario, VT-STB starts tracking the slowest particles by choosing large timescales. Thereafter, the iteration starts with a finer temporal resolution. This process continues up to maximum acquired frequency when the fastest particles are tracked. As a result, this method showed improved performance in reducing the number of false trajectories by adding one more iterative loop on the original STB and adopting the acquired timescale after each iteration.

2.5.2 Kernelized Lagrangian Particle Tracking (KLPT)

In 4D-PTV, we are interested in following the same particles at different acquisition times over a series of particle images. There is no challenge if the particle concentration is low with a high acquisition frequency. However, Kernelized Lagrangian Particle Tracking (KLPT [2]) was proposed to track particles with low temporal information and high particle concentrations. KLPT computes objective matrices to reconstruct the trajectories. Methods like STB need to minimise the kinematic measurement metrics, such as acceleration change minimisation. KLPT proposed a tracking algorithm by detection paradigm, which is a well-known term in the computer vision community. We first define a backward nonlinear function $f : \mathbb{I}_p \rightarrow X_p$ that maps local image patches from a series of particle images to 3D coordinates. In KLPT, our objective is to find f that minimises the regularised empirical risk (standard formulation in machine learning),

$$R(f) = \sum_{j=1}^{N} \|X_p - f\left(\mathbb{I}_p\right)\|^2 + \lambda \|f\|^2_{\mathcal{H}_K}, \tag{2.3}$$

where the first term measures the discrepancy in terms of an approximated function over N sample pairs. Each sample represents a possible state of the particle p. The second term is regularisation on nonlinear function in reduced kernel hyperspace. Therefore, we can learn f with N samples to compute the corresponding particle coordinate as $\hat{\mathrm{X}}_p = \mathrm{f}\left(\mathbb{I}^{rec}_{p*}\right)$. KLPT performs random sampling instead of dense sampling (like as Tomo-PIV) inspired by ensemble data assimilation techniques due to its lower computation demand. So KLPT

samples particle peaks in the object space (3D coordinate) to be predicted to the next step. Then we obtain image local patches from OTF. With these sample pairs, we can solve the empirical risk minimisation problem. The Representer theorem can obtain the closed-form solution. So the nonlinear function f can be solved as a linear combination of the Kernel functions ($\overline{\overline{\kappa}}$),

$$f(\mathbb{I}) = \sum_{j}^{N} \overline{\overline{\kappa}} \left(\mathbb{I}_p^j, \mathbb{I} \right) \vec{\alpha}^j, \tag{2.4}$$

where $\vec{\alpha}^j$ is a weighting vector. The Kernel function compares similarities between a sample $\mathbb{I}_p^j$ and another candidate (local image patches). The tracking problem in KLPT is divided into two stages, learning weighting vector and detecting unknown particle positions. The weighting vector $\vec{\alpha}^j$ is derived as

$$\vec{\alpha} = \left(\overline{\overline{K}} + \lambda I_{dN} \right)^{-1} \left[\left(X_p^1 \right)^T \ldots, \left(X_p^N \right)^T \right]^T. \tag{2.5}$$

So we have a linear optimisation problem by knowing f in equation (2.3) resulting in particle reconstruction as

$$\hat{X}_p = f \left(\mathbb{I}_{p*}^{rec} \right). \tag{2.6}$$

Worth mentioning that this solution is similar to ensemble data assimilation formulations based on learning and detecting processes. Yang and Heitz [2] showed linear optimisation formulation in KLPT is a fast and robust algorithm if the temporal resolution is sparse or complex turbulent motions such as the wake flow exists where the prediction is uncertain. In general, KLPT is an adapted version of the original STB algorithm that replaced the optimisation step. The rest of the process, including reconstruction, initialisation, and prediction, follows the STB algorithm. It was found that KLPT can capture longer tracks and provides more detailed flow reconstruction at highly turbulent regions than STB [2].

Chapter 3

Lagrangian Coherent Structures (LCS)

We have known for a long time that the flow is featured by coherent structures. Coherent structure detection techniques mainly focused on regions with high vortices in the Eulerian framework. In contrast, Lagrangian Coherent Structures (LCS) introduced by Haller and Yuan [55] are moving along the time in the Lagrangian framework. There are all kinds of coherent structures in nature that appear in complex flow fields. For example, the atmospheric flows passing around an island represent coherent structures (see figure 3.1). The cloud visualisation allows the illustrating formation of von Kármán vortex street downstream of the object.

Haller and Yuan [55] showed how to compute objective LCS (invariant manifolds) from noisy velocity fields obtained from experiments. This finding led to more investigations in applying classic nonlinear dynamical systems into fluid flows. Later on, Shadden [56] studied how finite-time Lyapunov exponents (FTLE) ridges are the same as LCS material lines and barriers of coherent motions. Application of using LCS to full three-dimensional turbulent flow fields such as channel flows was performed by Green et al. [57]. Haller [3] reviewed using LCS in classical dynamical systems such as saddle fixed point and chaos for time-varying fluid flows. FTLE is a quantifiable value that determines how to extract coherent structures in the Lagrangian framework. To start, we model the fluid flow as a dynamical system as

$$\frac{d}{dt}X = U(X,t), \tag{3.1}$$

where U is unsteady fluid flow as a function of space and time, and X is the particle position. We are interested in knowing how tracer particles move along the fluid with FTLE. Tracer particle means that it is passive and neutrally buoyant, and all the inertial effects are neglected. This chapter introduces how to compute the FTLE value and its derivation based on sparse trajectories. Then we will discuss how to quantify coherent or

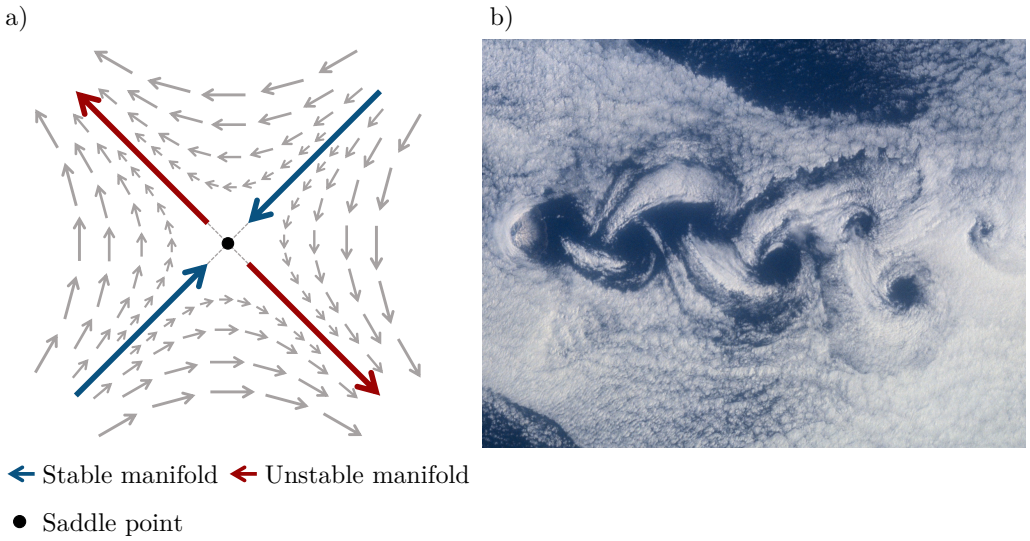

Figure 3.1 – Lagrangian coherent structures (LCS). (a) Classical dynamical structures representing a hyperbolic flow patterns. (b) Coherent Lagrangian patterns in nature, Rishiri Island, Japan (reprinted from NASA STS-130 Mission).

non-coherent neighbour trajectories by locally computing FTLE values.

3.1 Finite Time Lyapunov Exponent

To compute FTLE, we assume that the local flow map is the particle trajectory in finite time from t_0 to t_0+T (in this study $T \geqslant 4$) in the Lagrangian framework. The flow map takes an initial condition at time zero and maps it forward over the interval time to the final position. In the Eulerian framework, particles are integrated along vector fields to create the flow map. The starting positions of random synthetic particles would be the initial condition at time zero. Then we can integrate the particles' positions by numerical time-stepping techniques such as forward Euler and Runge-Kutta integrators. In the Lagrangian frame, we take the nearest neighbours around every single particle in the domain of interest. After that, FTLE examines how flow maps of the nearest neighbours deform in time. Therefore, the idea is simplified to analyse spatial displacements between the target particle and its neighbours over time. In general, two neighbour trajectories can extract (stretch), contract, or rotate in time. Worth mentioning that the area around a group of neighbour trajectories at the starting point of the FTLE computation must be the same area of their deformed shape at their final positions in incompressible flows.

The flow map of a single particle can be formulated as

$$\Phi_{t_0}^{t_0+T}(x):\ x(t_0)\ \rightarrow\ x(t_0+T), \tag{3.2}$$

where $x(t_0)$ is the starting position of the interval time T, and $x(t_0+T)$ is the final position. Therefore, we compute flow maps of all particles through time. Schematically, Lyapunov exponent is a term from classical dynamical systems that highlight regions with the most stretches if the interval time is positive (forward). Differences between the flow maps of the target particle $\Phi_{t_0}^{t}(x_0^p)$ and its neighbour $\Phi_{t_0}^{t}(x_0^n)$ would result in a vector displacement as following

$$\delta x(t) = \Phi_{t_0}^{t}(x_0^p) - \Phi_{t_0}^{t}(x_0^n). \tag{3.3}$$

This vector displacement contains transformations between the initial and final positions of two particles. In classic dynamical systems, if we add a perturbation ϵ to the starting position x_0 of a particle, we can Taylor expand how the particle behaves forward in time ($T > 0$). Then the final position of the perturbed particle will be the sum of its original position and the amplification factor

$$\Phi(x+\epsilon) \approx \Phi(x) + \mathbf{D}\Phi(x)\cdot\epsilon, \tag{3.4}$$

where the derivative of the flow map gives this amplification, the largest amplification factor occurs in regions with the largest FTLE value. So, equation (3.4) can be linearized by using the first term of the Taylor series of $\Phi_{t_0}^{t}(x_0^n)$ expanded around x_0^p

$$\delta x(t) \approx \frac{\partial \Phi_{t_0}^{t}(x_0^p)}{\partial x_0}\delta x_0, \tag{3.5}$$

where $\delta x_0 = x_0^p - x_0^n$. The state-transition matrix $\partial\Phi_{t_0}^{t}(x_0^p)/\partial x_0$ is also known as deformation gradient tensor $\nabla\Phi_{t_0}^{t}(x_0)$ [56]. The deformation tensor carries valuable information including the rate of expansion, compression and rotation. The magnitude of $\delta x(t)$ is

$$|\delta x(t)| = \sqrt{\delta x(t)\delta x(t)} = \sqrt{(\nabla\Phi_{t_0}^{t}(x_0)\delta x_0)(\nabla\Phi_{t_0}^{t}(x_0)\delta x_0)} = \sqrt{\delta x_0(\nabla\Phi_{t_0}^{t}(x_0)\nabla\Phi_{t_0}^{t}(x_0))\delta x_0},$$

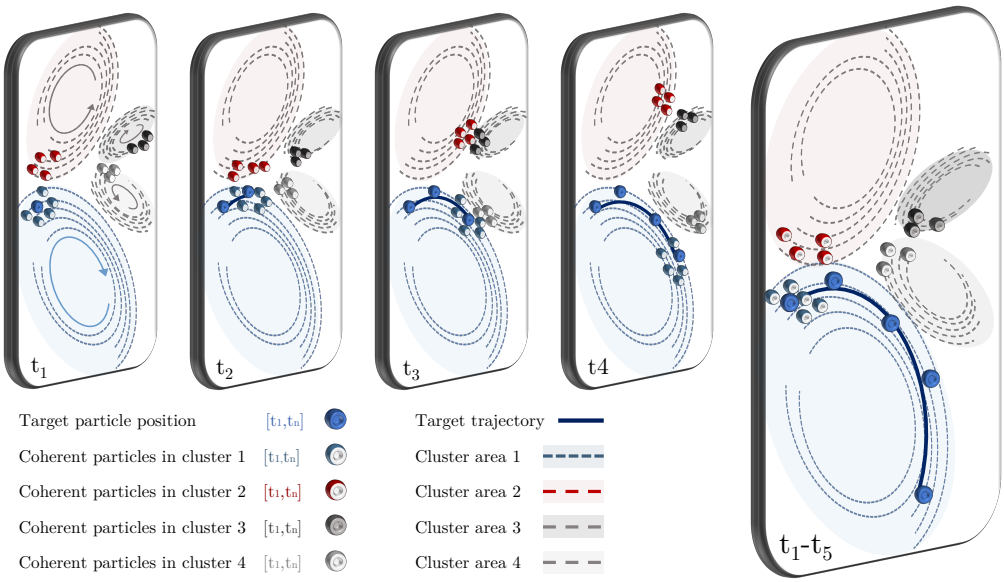

Figure 3.2 – Schematic of particle trajectories in 2D pair vortices starting from t_1 to t_5. (t_1) The target particle with coherent neighbour particles located in a clockwise vortex (blue cluster), non-coherent particles belong to different clusters. (t_2) The target particle trajectory (dark blue line) approaches the particles in the red cluster. (t_3) The target particle separation with non-coherent particles in the red cluster and approaching to the particles in the grey cluster. (t_4) Separation of non-coherent particles in the grey cluster with the target particle. ($t_1 - t_5$) Full trajectory view of the target particle alongside coherent particles in the blue cluster.

where we define

$$\Delta = \nabla\Phi_{t_0}^{t}(x_0)\nabla\Phi_{t_0}^{t}(x_0). \tag{3.6}$$

Δ is a symmetric positive definite matrix, also known as the right Cauchy-Green deformation tensor [56] with three real and positive eigenvalues in a 3D domain over finite time. As mentioned before, FTLE measures the stretching rate between the target particle and its neighbour. The maximum eigenvalue (the largest singular value) of the Cauchy-Green tensor $\lambda_{max}(\Delta)$ shows the maximum amount that can be possibly stretched (expansion or separation) in finite time. On the other hand, these fields also represent how the flow field is sensitive to perturbation. Furthermore, the eigenvector corresponding to $\lambda_{max}(\Delta)$ represents the direction of the separation. Eventually, the magnitude of the maximum displacement can be written as

$$|\delta x(t)_{max}| = \sqrt{\delta x_0 \lambda_{max}\left(\Delta\right) \delta x_0} = \sqrt{\lambda_{max}\left(\Delta\right)}|\delta x_0|, \tag{3.7}$$

and the FTLE value $\Lambda_{t_0}^t$ is defined by scaling the magnitude of the maximum displacement as

$$\Lambda_{t_0}^t = \frac{1}{|T|}\sqrt{\lambda_{max}\left(\Delta\right)} = \frac{1}{|T|} log\left(\frac{\delta x(t)}{\delta x(t_0)}\right). \tag{3.8}$$

Forward-FTLE means that the interval time is positive, and we assess forward flow maps. Moreover, negative interval time leads to backward-FTLE values, so particles that stretch more in backwards time accumulate material in forwarding time. In experimental fluid mechanics, smoke visualisations that are very intuitive to human eyes illustrate backward-FTLE structures by accumulating the smoke through thin lines in forwarding time, theoretically stretching in backwards. Both backwards-forward values provide essential information of the Lyapunov exponent field. Regions that stretch the most forward and backward times determine stable and unstable manifolds over the computed time. High values in the FTLE field show the existence of ridges that divide the local area into different clusters of coherent particles. Particles that start on one side of a ridge tend to stay on the same side. So the FTLE ridges are almost like invariant manifolds where the particles are not able to pass through them. A lower FTLE value means the neighbouring particle acts similarly, with no sign of separation from the target particle over the finite time. So, the FTLE ridges provide a direct analogue of stable and unstable (see the figure 3.1.a) manifolds for classic dynamical systems. Stable and unstable manifolds are used to understand nonlinear differential equations. Assuming a nonlinear differential equation, we need to determine the fixed points to find eigenvalues and eigenvectors to check if they are stable fixed points or saddle points. We can take the eigenvectors associated with eigenvalues will show subspaces where the dynamics are invariant. Moreover, by continuing along those subspaces, we sweep out these manifolds where if a point starts on one side of the manifolds, it will stay on that side forever. It is a way of segmenting the phase space into different coherent regions. FTLE gives determined time-varying information of these stable and unstable manifolds in unsteady flow fields. This formulation makes it possible to index a group of neighbour particles as coherent or non-coherent with the target particle.

3.1.1 FTLE ridge detection

To quantify a threshold for the FTLE ridge detection, we assessed the FTLE map for the case of 2D homogeneous isotropic turbulence given by DNS. We found that values above the threshold 0.25 are optimal criteria to estimate the FTLE ridge positions. This

threshold was in agreement with studies using global FTLE ridge calculation in the range of $50\% - 80\%$ of the maximum FTLE value [58]. Ridge detection algorithms search for spatial places with zero derivatives and the highest curvature of the FTLE fields. There are valuable studies in ridge detection algorithms with extensive computation costs that can be employed instead of using a constant FTLE threshold (see, e.g., Shadden et al. [56]).

3.2 Coherent and non-coherent clusters

In the present study, the ultimate goal of using LCS is to locally determine coherent and non-coherent neighbour trajectories. We use FTLE, as it is the most commonly used method of quantifying boundaries between separated regions [59]. A study from Hadjighasem et al. [60] globally compared twelve techniques to detect coherent Lagrangian structures in 2D flows. It was found that FTLE is a simple and objective algorithm with suitable performance of capturing hyperbolic LCS. However, the technique becomes unreliable in elliptic LCS structures. More research is needed to understand and track clusters of coherent particles in real experiments. For further investigations, the FTLE function can be replaced with advanced LCS detection algorithms (see, e.g., [61]) or other coherent motion detection techniques such as Coherent Structure Colouring (CSC [62]). In the following sections, we address three local segmentation techniques to be compared locally.

3.2.1 Local segmentation by FTLE

This section explains segmenting the phase space into different coherent regions, knowing that every single particle is spatially and temporally coherent with a specific cluster of other particles following the same behaviour [6]. Figure 3.2 shows a schematic of coherent and non-coherent groups of neighbour particles in different colours evolving by time $(t_1 - t_5)$. A particle can spatially meet a group of other particles in which there is no coherency link between them. There are many available concepts to identify LCS from looking for separatrix lines or surfaces which divide structures into different coherent regions [3]. To use the benefits of the FTLE map, we need to quantify the deformation matrix over sparse Lagrangian trajectories. In the Lagrangian frame, a derivate of flow maps representing sensitivity to small perturbations can be approximated by the Jacobian

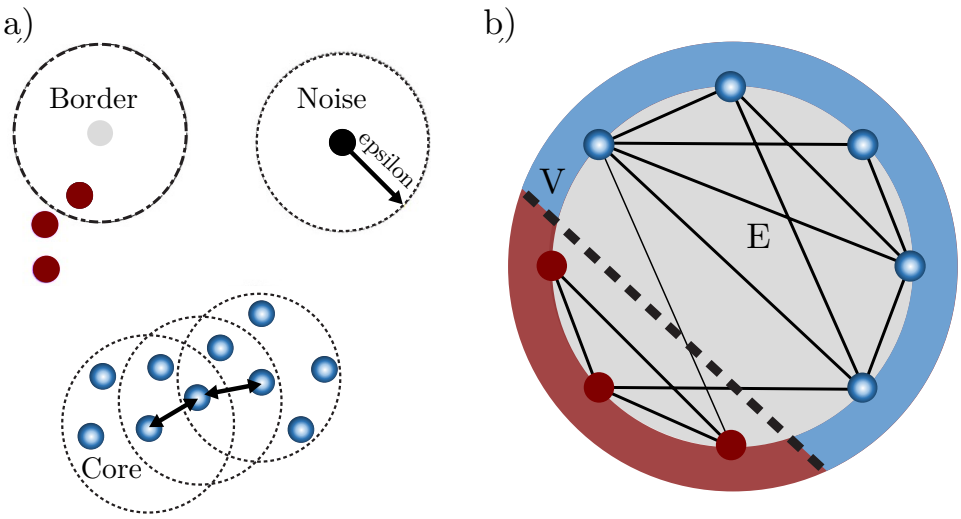

Figure 3.3 – Schematic of particle segmentation methods. (a) Density based spatial clustering of applications with noise (DBSCAN). (b) Spectral clustering technique. The black dashed line shows the solution (cut) of graph nodes with similarity, reprinted from Hadjighasem et al. [63].

operator in time and space. Therefore, the spatial derivative of flow maps in 2D condition will become

$$D\Phi_0^T \approx \begin{bmatrix} \frac{\Delta x(T)}{\Delta x(0)} & \frac{\Delta x(T)}{\Delta y(0)} \\ \\ \frac{\Delta y(T)}{\Delta x(0)} & \frac{\Delta y(T)}{\Delta y(0)} \end{bmatrix} = \begin{bmatrix} \frac{x_{i+1,j}(T)-x_{i-1,j}(T)}{x_{i+1,j}(0)-x_{i-1,j}(0)} & \frac{x_{i,j+1}(T)-x_{i,j-1}(T)}{y_{i+1,1}(0)-y_{i,j-1}(0)} \\ \\ \frac{y_{i+1,j}(T)-y_{i-1,j}(T)}{x_{i+1,j}(0)-x_{i-1,j}(0)} & \frac{y_{i,j+1}(T)-y_{i,j-1}(T)}{y_{j+1}(0)-y_{i,j-1}(0)} \end{bmatrix}. \tag{3.9}$$

The Jacobian matrix computes the finite ΔX at the final time over ΔX at the initial time. So it will become the spatial derivatives (deformations) from the starting to the final points. Any stretching and deformation in flow will impact the Jacobian matrix. Similar to the Eulerian framework, the eigenvectors and eigenvalues of this Jacobian of the flow map represent the most stretching, contracting, or rotating directions. Worth mentioning that the determinant of this matrix should be ideally one for incompressible flows. So for every particle, we compute the finite difference derivative matrix to identify how much trajectories stretch in finite time. This follows by computing the maximum stretching that can occur between neighbour trajectories, resulting in the finite-time Lyapunov exponent value. Finally, every single trajectory will be indexed by the FTLE value for further processes.

To perform local segmentation, we defined a local Eulerian frame around each particle,

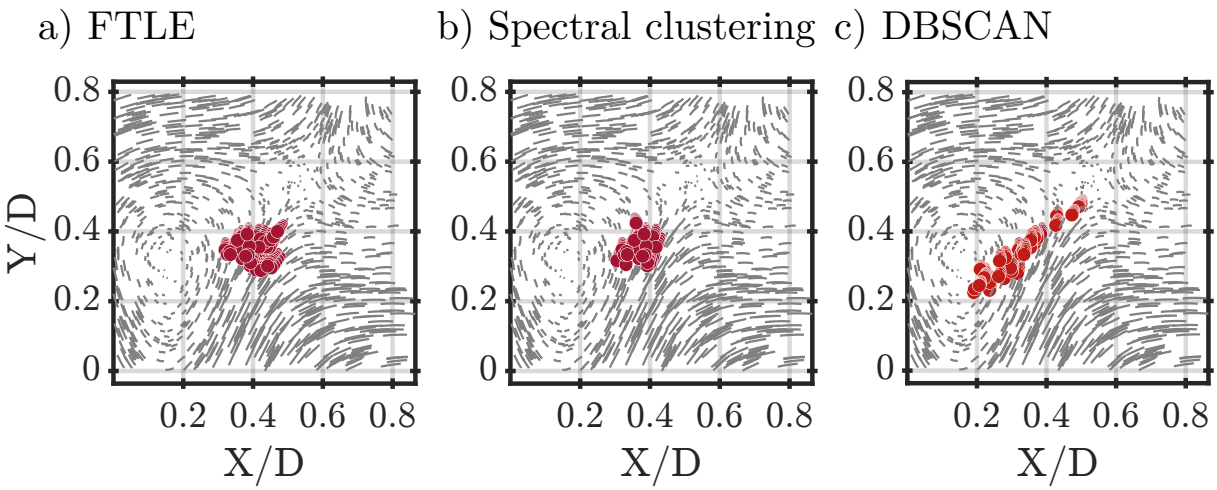

Figure 3.4 – A local segmentation snapshot of 2D-HIT flow. (a) FTLE. (b) Spectral clustering. (c) DSCAN.

while all neighbourhood particles inside this area must be classified as coherent or non-coherent with the target particle. This frame is fixed during a series of time-steps that provide an Eulerian view of the neighbourhood behaviour. Velocity values of the target particle are used to quantify the Eulerian frame size in each direction. If 2D/3D velocity values are equal in each direction, the shape would be a circle/sphere around the target particle. All particles inside the Eulerian frame in the same phase or with phase delay are considered neighbourhoods. A lower FTLE value means a neighbouring particle is coherent and acts in the same behaviour with the target particle spatially over a specific temporal scale. We introduced such a concept for the track initialisation in 4D-PTV studies (see Chapter 5).

3.2.2 Density-based spatial clustering

Density-Based Spatial Clustering of Applications with Noise (DBSCAN) [64] detects data outliers (clustered data) and arbitrarily shaped clusters (clustered data). DBSCAN retrieves cluster indices and a vector indicating which observations are core points (points inside clusters). There is no need to know the number of clusters beforehand, and clusters are not necessarily spheroidal. In addition, DBSCAN can also be used to detect cluster-free points because it finds those that are not associated with any cluster. A Lagrangian particle must be associated with a cluster if it satisfies the condition that at least a certain number of neighbours are present in its epsilon neighbourhood. In either case,

the particle can be within the epsilon neighbourhood of another particle that satisfies both the epsilon and the minimum number of neighbours requirements. The DBSCAN algorithm can identify three kinds of core, border, and noise particles. A core particle is a particle within a cluster with the minimum number of neighbours in its epsilon neighbourhood. The border particle belongs to a cluster whose epsilon neighbourhood contains fewer neighbours than the minimum. A noise particle is an outlier that does not come from any cluster. For specified values of the neighbourhood epsilon and the minimum number of neighbours required for a core point, the DBSCAN function can be implemented. From the input data set of Lagrangian positions X, DBSCAN selects the first unlabelled observation x_1 as the current point, and initialises the first cluster label C to 1. Then we find the set of points within the epsilon neighbourhood of the current point, as showed in figure 3.3. If the number of neighbours is less than a certain threshold, the algorithm labels the current point as a noise point (or an outlier). The process continues until the first cluster is indexed to label the target particle as a core point belonging to the cluster C_1. DBSCAN is an iterative process over each neighbour particles until no new neighbours are found that can be indexed as belonging to the current cluster.

3.2.3 Spectral clustering

Spectral clustering is a graph-based algorithm for partitioning data points, or observations, according to similarity between Lagrangian trajectories. The spectral cluster requires specifying the number of clusters k [61], [63] . The technique involves representing the data in a low dimension where clusters are more widely separated, enabling to use k-means or k-medoids clustering algorithms [65] . This low dimension is based on the eigenvectors corresponding to the number of clusters, the smallest eigenvalues of a Laplacian matrix. However, it is possible to estimate the number of clusters by counting the number of zero eigenvalues of the Laplacian matrix. A Laplacian matrix is one way of representing a similarity graph that models the local neighbourhood relationships between data points as an undirected graph, as illustrated in figure 3.3.b. The spectral clustering algorithm derives a similarity matrix of a similarity graph from the data, finds the Laplacian matrix and uses the Laplacian matrix to find k eigenvectors for splitting the similarity graph into k partitions. By default, the algorithm for spectral cluster computes the normalised random-walk Laplacian matrix using the method described by Shi and Malik [66] . The spectral cluster also supports the unnormalised Laplacian matrix and the normalised symmetric Laplacian matrix, which uses the Ng-Jordan-Weiss method

[67].

3.2.4 Local segmentation results

We examined local segmentations of FTLE, DBSCAN and spectral clustering techniques for the synthetic 2D homogeneous isotropic turbulent (HIT) flow. Details of the synthetic dataset are discussed in section 4.3. It was found that the DBSCAN technique is severely sensitive to the search radius and the minimum number of neighbours, at least in turbulent flows. However, it works fairly fast and is acceptable if it is well-tuned, which can be challenging in real experiments. In the clustering approach, to estimate the number of clusters, we initialised the k value by 50, knowing that 2D-HIT has few small scale clusters locally, to determine how many of the eigenvalues are nearly zero. This represents the number of connected components in the similarity graph (see figure 3.3.b). Therefore, the number of nearly zero eigenvalues in the optimal value for k. One snapshot of the local clustering in shown in figure 3.4. Both spectral clustering and FTLE based functions are almost robust compared with DBSCAN, but they still require optimal tunings which is case dependent. As mentioned earlier, FTLE is the most straightforward technique to detect LCS [59] and local segmentations results from FTLE were in agreement with the global comparison from Hadjighasem et al. [60]. In this thesis, we employ FTLE for the rest of assessments mainly because it is a well established technique.

Chapter 4

Experimental and Numerical Data Creation

We employed a series of numerical synthetic and experimental velocimetry measurements to validate and assess our proposed methods in this thesis. A total number of seven datasets are provided to be used as test cases of the following sections. The details of these cases are shown in table 4.1. We address two 4D-PTV experiments of the jet impingement and the wake behind a cylinder in section 4.1. These two experiments are employed for tracking assessments in Chapters 5 and 6, respectively. In addition to the assessment in Chapter 5, we examined our algorithms with the 4D-PTV data from the LPT challenge [43] in which the performance results were provided by the challenge committee. The third experiment was 2D planar PIV of the cylinder wake flow (see section 4.3). To quantify the tracking performance, we created 2D and 3D synthetic datasets obtained from Direct Numerical Simulation (DNS), discussed in section 4.3.

Table 4.1 – Test cases of the present study

	Case	Data type	Reynolds	Application
4D-PTV	Cylinder wake flow	experiment	3900	Chapter 6, 7
	Jet impingement	experiment	2500	Chapter 5
	Wall bounded wake	LPT challenge	4500	Chapter 5
	Cylinder wake flow	DNS numerical	3900	Chapters 5, 6
	Cylinder wake flow	DNS numerical	300	Chapter 6
2D-PTV	HIT	DNS numerical	3000	Chapters 6, 8
2D-PIV	Cylinder wake flow	experiment	3900	Chapter 8

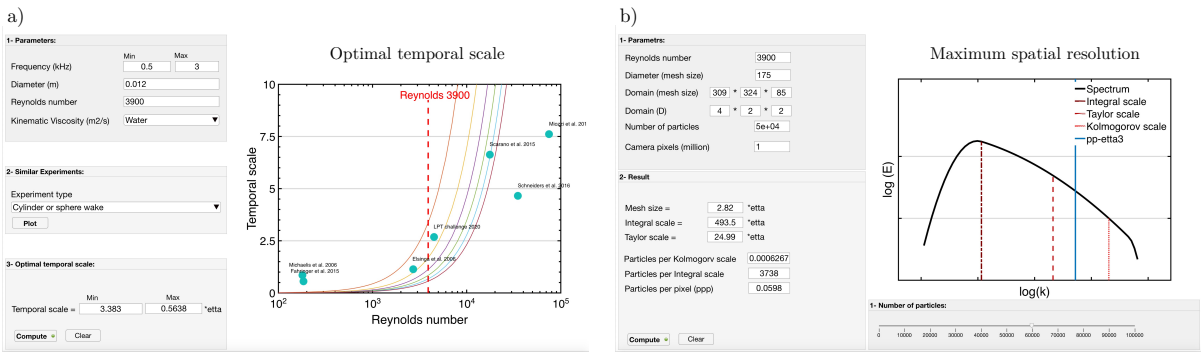

Figure 4.1 – 4D-PTV experiment setup design. (a) Acquisition frequency selection as a function of hardware facility and flow properties. Comparison was made with similar volumetric experiments. (b) Desired particle concentration with respect to the turbulent length scales.

4.1 4D-PTV experiments

A volumetric velocimetry experiment requires three major steps, experiment design, data acquisition, data processing. This section addresses details of designing volumetric experiments in a wind tunnel and introductory remarks on performing the experiment. Then we discuss jet impingement and the cylinder wake flow setup designs and the acquisition procedure. Processing of the acquired data will be discussed in later Chapters 5, 6 and 7.

4.1.1 Experiment setup design

The first parameter that needs to be defined before performing a volumetric experiment is the acquisition frequency (i.e., temporal scale). The sampling rate is a crucial parameter that must resolve minimum convective motion and be estimated in advance. It is perpetually desirable to reach a higher sampling rate (i.e., the acquisition frequency) to resolve higher temporal resolution in turbulent flows. Furthermore, the observation time needs to be long enough to follow the dynamical evolution of structures. A large number of observations might be necessary in the case of performing statistical analysis or machine learning studies. As the Reynolds number increases, the particle displacement jumps, and therefore, 4D-PTV algorithms fail after a limit depending on the maximum available acquisition frequency (hardware limitation). This means that the temporal scale

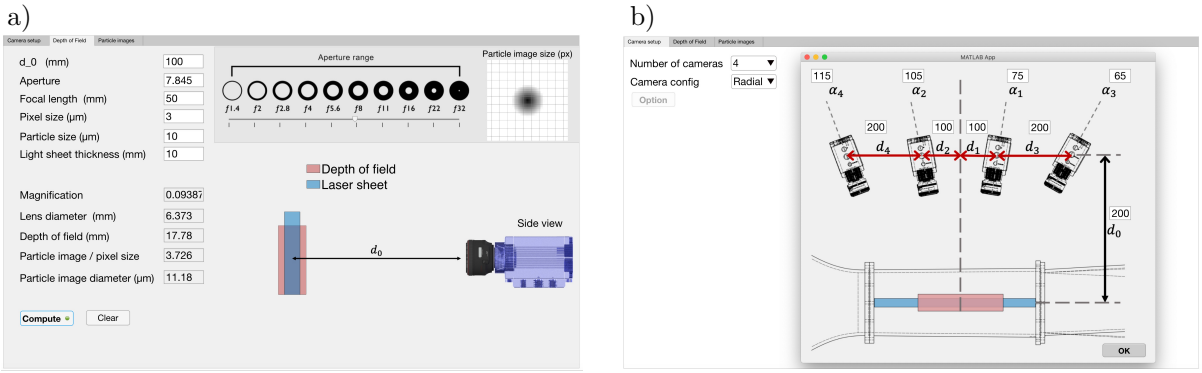

Figure 4.2 – Velocimetry camera setting design. (a) Computation of the desired depth of field based on camera properties. (b) Multi camera setup design.

and the mean particle displacement should be computed before starting any acquisition, particularly in wind tunnel experiments. We designed an open-access software package in Graphic User Interface (GUI) to roughly estimate the minimum parameters required to perform an experiment. Figure 4.1.a shows one snapshot of optimising the temporal scale in an experiment based on flow properties and recent similar experiments. The achievable range for the temporal scale can be tuned as a function of the Reynolds number, turbulent length scale and hardware acquisition facilities. The selected temporal scale should be in the same range as similar volumetric studies, as shown in figure 4.1.a. The second parameter is to determine the maximum achievable spatial resolution. It is possible to compute particle concentration based on a rough estimation of the volume of interest and number of particles if we assume that the seeding particles are distributed homogeneously in the domain. Figure 4.1.b shows of snapshot of particle concentration sizing as a function of turbulent length scales. Average number of particles per volume of turbulent length scales (Kolmogorov, for example) determines the maximum achievable spatial resolution of the experiment. As a result, we can roughly estimate the optimal temporal scale and spatial resolution to perform a volumetric measurement.

The next step is to compute the optical parameters. Depending on the type of camera, the pixel size is known. Therefore, the magnification factor can be identified as a function of camera distance to the domain of interest. The camera depth of focus must be larger than the illumination depth to assure focused projections of the illuminated particles. Therefore, we can adjust the optimal aperture, magnification factor, and focal length to tune the depth of focus value as shown in figure 4.2.a. The particle image size

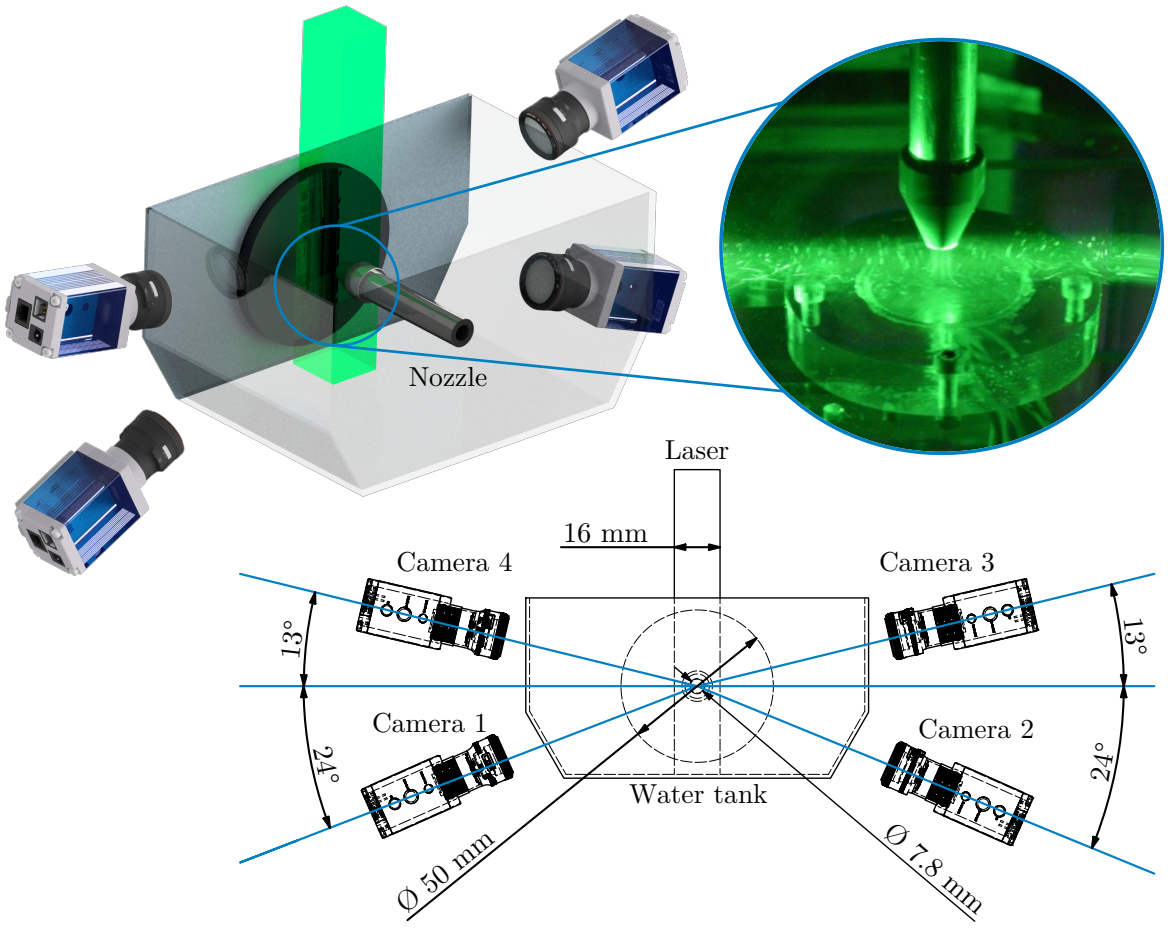

Figure 4.3 – 3D schematic view of the jet impingement experimental, with snapshot of the experiment in zoom balloon.

is another crucial parameter needs to be computed. The optimum particle image size for such experiments should be around 2-3 pixels to avoid peak locking and having an immense particle image size. We can obtain the estimated particle image size in pixel as a function of camera aperture and magnification factor as shown in figure 4.2.a. 4D-PTV algorithms need a minimum of three cameras to reconstruct true particles and suppress ghost reconstructions (see section 2.2. The software package is a graphic calculator that computes required optical parameters for a range of typical multi-camera setups, including radial, X (double stereo in two sides), and arc configurations as shown in figure 4.2.b. Eventually, we can design the experiment optical parameters based on available facilities and the experiment geometry.

4.1.2 Jet impingement experiments

We used the data from a volumetric experiment of liquid-liquid jet impingement on a circular wall at a Reynolds number equal to 2500. Perpendicular impinging the jet into the wall creates significant deceleration inside the jet core. The deceleration and directional 3D motions of particles are featured by multi-vortex rings around the jet and secondary vortex structures after the impingement. Figure 4.3 shows the schematic view of the experiment setup. Four Phantom $M310$ cameras with 1200×800 resolution and the maximum frequency of 3.26 kHz are empowered (see table 4.2). Nikon 105 mm macro F2.8 (aperture was set to F22) lenses were adjusted by the double angle Scheimpflug adaptors.

As shown in figure 4.3, two cameras were positioned in 24 degree with forward scatter light, and the other two cameras were in backward scattering at 13 degree. 15 mJ LDY 300 laser and a mirror at the bottom of the water tank were set for the illumination with 0.5 kHz frequency ($dt/\tau_\eta = 2.18$) and converted into the rectangular light volume. In the water tank, prisms were used to reduce the distortion caused by the air-glass-water interfaces. A mirror at the bottom of the tank back-reflected the laser beam throughout the measurement volume. The measurement volume was 16 mm $\times$ 51 mm $\times$ 35 mm (29 cm^3). The distance between the nozzle exit and the ground was 24 mm (3D). The seeding particles were hollow glass spheres with $9 - 13$ μm diameter, and 1.1 g/cm^3 density. The particle concentration was approximately 0.03 ppp that was equivalent to 2×10^{-6} ppη^3. The calibration error was less than 0.03 pixel. The measurement uncertainty due to the displacement and global bias errors was estimated to be in $2.0 - 3.5$ % of the boundary layer in the wall jet region.

4.1.3 Cylinder wake flow experiments

Volumetric measurement

An experimental study of the cylinder wake flow at Reynolds number equal to 3900 (same value as the synthetic data) was performed. Experiments were carried out in the wind tunnel equipped with a centrifugal fan, a diffuser, a plenum chamber with honeycomb and grids, a contraction section decreasing by 4, and an area with transparent walls for testing. With the aid of hot wire anemometry, the velocity profile at the wind tunnel entrance was checked to ensure uniformity. The free-stream turbulence intensity level was found to be less than 0.2 %. The cross-section of the testing zone is square, with

Table 4.2 – Jet impingement experiment setup parameters.

Setup	Value
Lenses	4× Nikon 105 mm
Cameras	4× Phantom $M310$
Resolution	1200×800
Pixel size	20 μm
Exposure time	250 μs
Illumination volume	16 mm × 51 mm × 35 mm
Acquisition frequency	0.5 kHz
Particle concentration	0.03 ppp
Number of images per experiments	2000 frames

a width of 28 cm and a length of 100 cm. It has a slightly tilted upper wall to reduce longitudinal pressure gradients. It is possible to choose a continuous flow velocity of 1 to 8 m/s.

In this classic wake flow case, the complexity of the flow topology is captured by preserving the areas where turbulence is produced. There are three such regions on an obstacle: the boundary layer, the two shear layers at the limit of the recirculation region, and the wake. We designed an experimental setup with four cameras as shown in Figure 4.4.a. Four CMOS SpeedSense DANTEC cameras with a resolution of 1280×800 pixels and the maximum frequency of 3 kHz are empowered. Cameras are equipped with Nikon 105 mm lenses. The first two cameras are positioned in backward light scattering, while the second two cameras receive maximum intensity signal in forward scattering. The calibration error was lower than 0.06 pixel and reduced to 0.04 after the volume self-calibration. The volume of interest was 280 mm × 160 mm × 46 mm starting from roughly $4D$ downstream of the cylinder, knowing that the vortex formation zone ends at $4D$. The aperture was set at 11 to achieve 46 mm depth of focus. We used an LED system to illuminate this large volume. The acquisition was long enough to observe dynamic evolutions of the von Kármán vortex streets downstream of the cylinder.

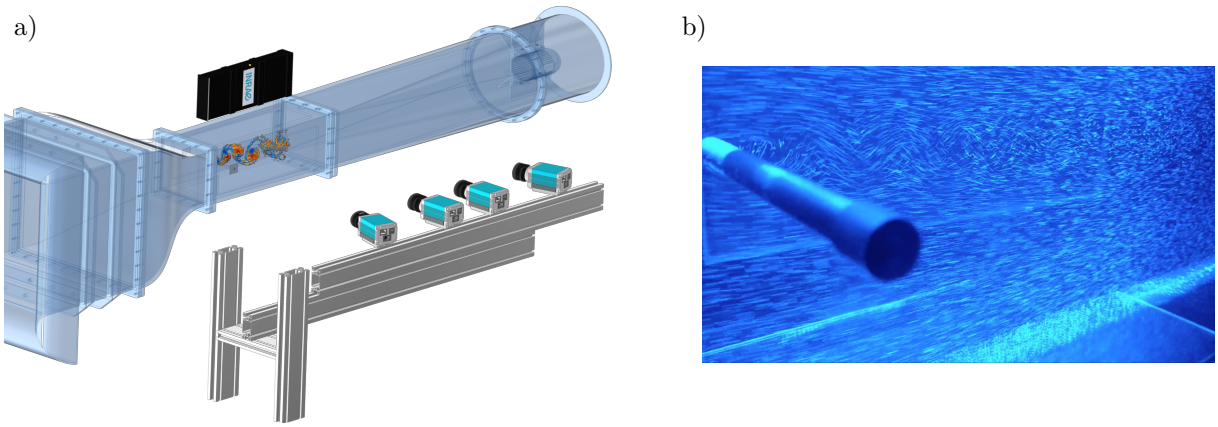

Figure 4.4 – Experiment setup design for the cylinder wake flow at Reynolds 3900. (a) Schematic of the camera setup design. (b) One snapshot of HFSB tracer particles passing downstream of the cylinder.

Seeding particles

As mentioned in Chapter 1, Helium Filled Soap Bubbles (HFSB) are key ingredients of performing large-scale volumetric experiments in air. Soap bubbles are the only tracers with a size significantly larger than 10 μm, leading to sufficient light scattering in the Large-scale volumetric measurements. Smaller particles such as oil droplets can create a very dense particle concentration and follow the flow accurately, but they scatter very little light. For this reason, volumetric measurements using these small seeding particles are restricted to small measurement volumes. Therefore, in the present experiment, the seeding particles were HFSB, resulting in desired intensity signal with appropriate particle size. In a similar experiment, Scarano et al. [41] studied application of using HFSB in the wake flow past a cylinder in a volume of $20 \times 20 \times 12$ cm^3 (4800 cm^3).

Based on a study carried out by Caridi et al. [68], HFSB was determined to have roughly $I_B/I_{\text{fog}} \sim (d_B/d_{\text{fog}})^2 \sim 10^5$ times more intensity compared with intensity of fog droplets. Particle time-response $\boldsymbol{\tau}_p$ is a value that determines how particles follow the flow with fidelity. Time-response is directly linked with the particle diameter and its mass density discrepancy to the air in wind tunnel experiments. Due to this reason, large fog droplets ($> 10 - 20$ μm) do not follow the flow with enough fidelity because of their poor time-response value. However, the mass density discrepancy is close to zero since HFSB particles are filled with Helium (lighter than air). As a result, the particle time-response for HSFB becomes small enough to follow the flow with fidelity. Accordingly, Scarano et al. [41] reported that the HFSB time-response is maintained well below 100 μs, which

means that particles should adequately follow the flow in low-speed experiments. So, large size particles with favourable time-response values provide the ability to perform large-scale measurement volumes [19].

However, bubbles are limited by three main factors in the wind tunnel experiments, including generation rate, lifetime, and image glare points. Due to these limitations, HFSB for large scale volumetric measurements inside the wind tunnel leads to low particle concentration (approximately 1 particle/cm^3). One of the earliest studies of using HFSB reported ppp < 0.01 for the seeding density, which could only resolve Karman vortices and unable to capture turbulent small scales [41]. Improved particle density was achieved by reserving particles in a chamber over time before running the acquisitions and releasing them during the experiment (Caridi et al. [68]). In 2018, Gibeau and Ghaaemi [69] reached to 1.6 particle/cm^3 with the idea of having multi-wing seeding system. The impact of the multi-wing generator on the flow stream is found to be at most 1.9 % of the turbulence intensity with a negligible deficit on the mean flow. Gibeau et al. [70] demonstrated to achieve 0.02 ppp over a volume of $20,000$ cm^3 using full-scale HFSB generator with 48 nozzles.

In the present study, we placed 50 bubble generator nozzles with airfoil-shaped structures inside the wind tunnel chamber. The nozzles were far upstream of the measurement section (in the settling chamber) to ensure a sufficient number of bubbles were created, and the main flow field was not disturbed by the existence of nozzles. The bubble lifetime is very short (less than $2-3$ minutes) inside the wind tunnel, mainly because they explode by passing through honeycomb layers. To overcome this issue, we injected bubbles inside the chamber for up to 5 minutes when the wind tunnel is off before starting the acquisition. We found that particles larger than three pixels create two glare points on two sides of the bubble when the illumination is LED. This requires more image treatments before running the 4D-PTV algorithm to avoid false particle reconstruction. However, the intensity of two glare points can diffuse and merge if the particle size is around two pixels. Therefore, we adjusted the camera magnification to reach particles with two pixel image sizes on average to surpass the glare point issue. Figure 4.4.a shows homogeneous distribution of tracer particles during the experiment.

4.2 2D-PIV experiments

We performed 2D-PIV experiments for the wake behind a smooth cylinder at the same Reynolds number as the volumetric experiment in section 4.1.3. PIV measurements were conducted at $z = 0$, just downstream of the circular cylinder. NewWave laser Solo3 based on neodymium-doped yttrium aluminium garnet (Nd: YAG) with an energy pulse of 50 mJ was employed to illuminate the region of interest. The diameter of the seeded particles is less than 10 μm (diluted Polyethylene glycol in water).

The Imager sCMOS camera (2560 $\times$ 2160 resolution) was equipped with a 50 mm lens and an aperture of 5.6. The Reynolds number was set at 3900 by adjusting the free stream velocity to 4.8 ms^{-1}. With a time interval between two successive images of 25 μs, 5000 image pairs are obtained. The circular cylinder has a diameter of 12 mm and a length of 280 mm. Two thin rectangular end plates are included, which meet Stansby's specifications [71]. In this case, the distance between the end plates is 240 mm, which results in an aspect ratio of 20. The space between the walls and the endplates is about 20 mm, which is larger than the boundary layer thickness. It has a blockage ratio of 4.3%. In the test zone, the circular cylinder is located horizontally at 3.5 D. Processing of the acquired 2D-PIV images is discussed in Chapter 8.

4.3 Direct Numerical Simulations (DNS)

4.3.1 Cylinder wake flow numerical dataset

The PIV/PTV community consistently requires synthetic datasets to assess and validate developed image-based methods. The EUROPIV Synthetic Image Generator (SIG) developed a standardised synthetic dataset framework for the PIV/PTV community [72]. SIG targeted three objectives: algorithm performance assessment, algorithm sensitivity analysis as a function of characteristic parameters, and algorithm comparison. Characteristic parameters refer to particle concentration (i.e., density), temporal scale, and noise ratio to determine how the synthetic dataset is similar to a real experiment. Since then, by increasing capabilities of the PIV/PTV techniques, algorithm assessments constantly require datasets of flows with relatively complex and high gradient regions associated with 3D directional dynamics. That was the motivation to generate a database of Eulerian velocity and pressure fields with Lagrangian trajectories for the wake carrying complex flow motions downstream of a smooth cylinder. Applications of the current dataset can be

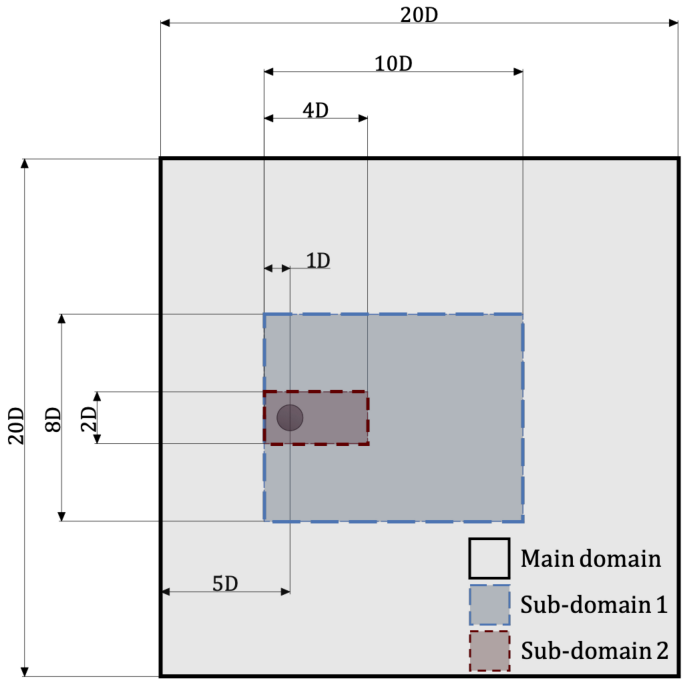

Figure 4.5 – Dimensions of two sub-domains from the flow over a smooth cylinder at subcritical Reynolds number 3900.

summarised in table 4.3. In this section, We first describe the creation of the Lagrangian data by transporting the synthetic particles in the Eulerian velocity volume. After that, we discuss how to set characteristic parameters for the synthetic data, including 1- Particle concentration, 2- Temporal scale, and 3- Noise level.

A highly-resolved DNS of the flow over a smooth cylinder at a subcritical Reynolds number 3900 (based on the diameter D of the cylinder and the free-stream velocity) was performed to generate the data. Double-precision Eulerian and Lagrangian fields for two sub-domains were collected, as shown in Figure 4.5. The dimensions of Sub-domain 1 are $10D \times 8D \times 6D$. Data were saved every 10 DNS time steps for Sub-domain 1 due to online cloud storage limitation (saving every time step would have required roughly 30 Tb of storage per vortex shedding). 1000 snapshots were also collected for a smaller sub-domain with dimensions of $4D \times 2D \times 2D$ (i.e., Sub-domain 2) for every DNS time step. Sub-domain 2 is suitable for studies requiring the highest possible temporal resolution. Details of two sub-domains can be found in table 4.4. One Eulerian snapshot of the current wake flow is shown in Figure 4.6. Lagrangian trajectories are provided for

Table 4.3 – Application of the current dataset in PIV / PTV community.

Dataset application	Trajectories	3D velocity	2D velocity	Pressure	Target studies
4D-PTV algorithm	✓	✗	✗	✗	[1], [6], [27]
Flow field reconstruction	✓	✓	✗	✗	[25]
Pressure from PTV	✓	✗	✗	✓	[73], [74]
Lagrangian physics	✓	✗	✗	✗	[53], [62]
Machine learning	✓	✗	✓	✗	[75], [76]
Eulerian physics	✗	✓	✓	✗	-
Data assimilation	✓	✓	✗	✓	[77]
CFD assessment	✗	✓	✗	✓	-
2D2C-2D3C-PIV	✓	✓	✗	✗	[14]
Tomo-PIV	✓	✓	✗	✗	[14], [78]

roughly $200,000$ synthetic particles for both sub-domains. Reading tutorial of the dataset is addressed in Appendix A.

Eulerian simulation and Lagrangian transport

The computations are carried out with the open-source flow solver named `Incompact3d` [79], [80] based on sixth-order finite-difference compact schemes for the spatial discretisation on a Cartesian grid. The simplicity of the Cartesian grid offers the ability to implement higher order spectral schemes for spatial discretisation. For the current simulation, the time advancement was performed with an explicit third-order Adams Bashforth scheme. The governing equations are solved with a fractional step method to treat the incompressibility constraint, which requires solving an additional projection step, the Poisson equation. This Poisson equation is fully solved in spectral space using three-dimensional Fast Fourier Transforms (FFTs). In the present work, the smooth cylinder is modelled using a customised immersed boundary method (IMB) with an artificial flow inside the cylinder to ensure the smoothness of the velocity field while imposing a no-slip boundary condition at the cylinder. More details about the flow solver can be found in Laizet and Lamballais [79]. `Incompact3d` is built with a powerful 2D domain decomposition for simulations on super-computers. The computational domain is split into a number of sub-regions (pencils) which are each assigned to an MPI process. The derivatives and interpolations in the x-direction (y-direction, z-direction) are performed in X-pencils (Y-pencils, Z-pencils), respectively. The 3D FFTs required by the Poisson solver are also

Table 4.4 – Specifications of two sub-domains from the flow over a smooth cylinder at subcritical Reynolds number 3900.

Domain	Dimension			Grid size			Time step	Size
	x	y	z	nx	ny	nz	dt (D/U_∞)	
Computation Domain	20D	20D	6D	1537	1025	256	0.00075	12.9 Gb
Sub-domain 1	(4-14)D	(6-14)D	6D	769	777	256	0.00075	4.8 Gb
Sub-domain 2	(4-8)D	(9-11)D	(2-4)D	308	328	87	0.0075	256 Mb

Table 4.5 – Synthetic particle concentration selection in terms of particles per cubic Kolmogorov and integral scales.

Case	particles	ppη^3	ppD^3
Low	$2,000$	10^{-5}	139
Moderate	$20,000$	10^{-4}	1386
High	$200,000$	10^{-3}	13861

broken down as a series of 1D FFTs computed in one direction at a time. Global transpositions to switch from one pencil to another are performed with the MPI command `MPI_ALLTOALL(V)`. `Incompact3d` can scale well with up to hundreds of thousands of MPI processes for simulations with several billion grid nodes [80]. Inflow/outflow boundary conditions are implemented along the streamwise direction with free-slip and periodic boundary conditions along the vertical and spanwise directions, respectively. The simulation was performed on nearly 4×10^{10} grid points (see table 4.4). The grid was uniform in the streamwise and spanwise directions, while a non-uniform grid was used in the vertical direction, with a grid refinement towards the centre of the cylinder. The finest grid size in the vertical direction was $\Delta y_{\min} = 0.00563D$. The dimensional DNS time step was 0.00075 D/U_∞ (where U_∞ is the free-stream velocity). It takes 6667 DNS time steps to simulate one vortex shedding. It should also be mentioned that 1333 DNS time steps correspond to one integral temporal scale D/U_∞.

Lagrangian transport accuracy

A comparison was made between the transport of particles at every 10 DNS time step (i.e., temporal scale of Sub-domain 1) with the transport of particles at every DNS time

a) Pressure Iso_Surface

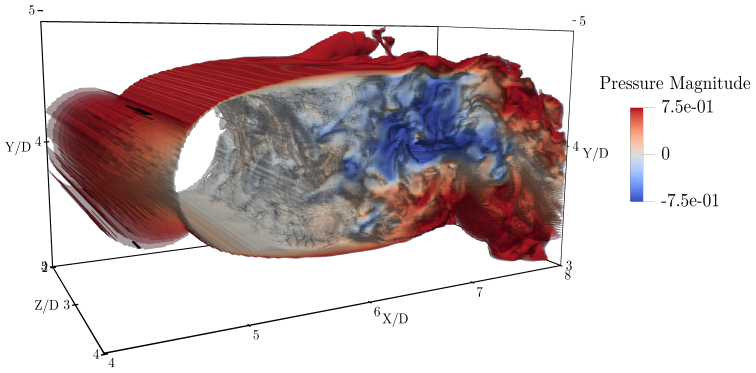

b) Lagrangian Trajectory

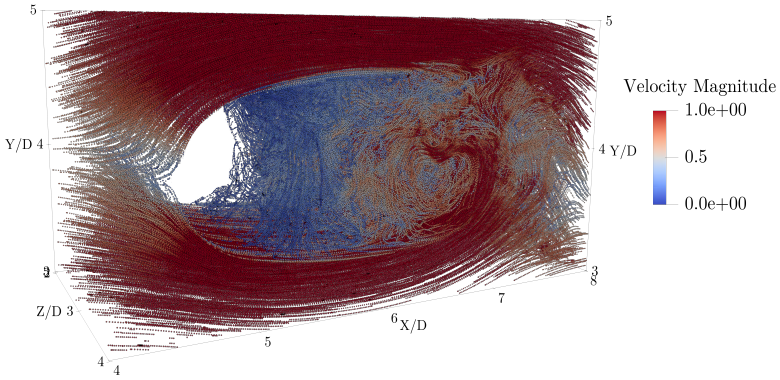

c) Q criterion Iso_Surface

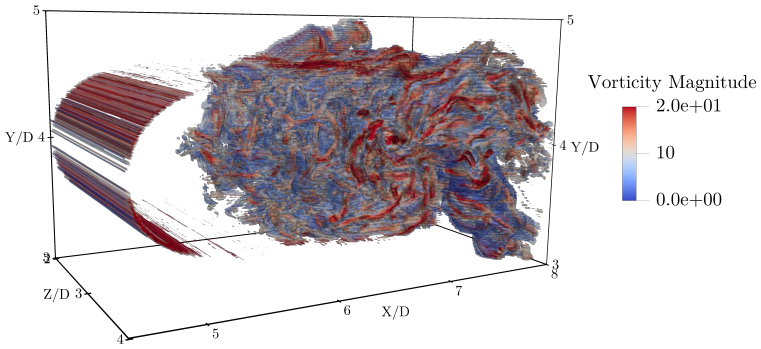

Figure 4.6 – Snapshot view of Sub-domain 2. (a) Pressure iso-surface coloured by the magnitude of pressure. (b) Lagrangian trajectories of 20,000 particles after 1000 DNS time step, coloured by the velocity magnitude. (c) Q criterion representation of the Eulerian flow structures coloured by the vorticity magnitude.

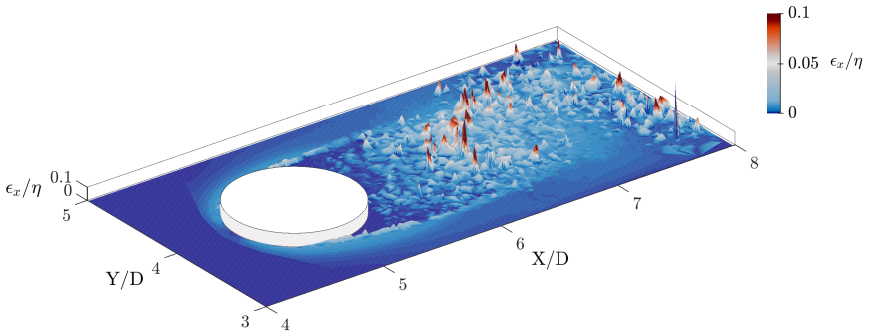

Figure 4.7 – 2D map of the non dimensional position error of Lagrangian transport computed every 10 DNS time step after 1000 time steps and after an average in the spanwise direction.

step in Sub-domain 2, to quantify the uncertainty level of trajectories in Sub-domain 1. As a result, the mean deviation of the trajectories between two temporal scales after 1000 DNS time steps in the larger domain is equal to 3.28 η, with η the Kolmogorov spatial scale. The standard deviation of position error is $\sigma_\epsilon = 0.017\ \eta$. Figure 4.7 shows a 2D map of the non-dimensional position deviation ϵ/η between two temporal scales averaged in the spanwise direction. Therefore, it is recommended to use the data from Sub-domain 2 for studies requiring accurate trajectories inside the wake region, while the data from Sub-domain 1 are better suited for studies focusing on large scale motions.

Particle concentration

In most PIV/PTV studies, particle concentration refers to the number of particles per pixel (ppp) that is principally an image-related parameter. The relation between the particle concentration and the turbulence length scales determines the maximum achievable spatial resolution. Therefore, it is crucial to address the number of particles corresponding to Kolmogorov (η), Taylor (l), and Integral (D) length scales. To quantify these relations, we used two volumetric metrics, namely, particles per cubic Kolmogorov scale (ppη^3) and particles per cubic Integral scale (ppD^3), instead of ppp. We chose three low, moderate, and high particle concentrations, respectively equal to $2,000$, $20,000$,

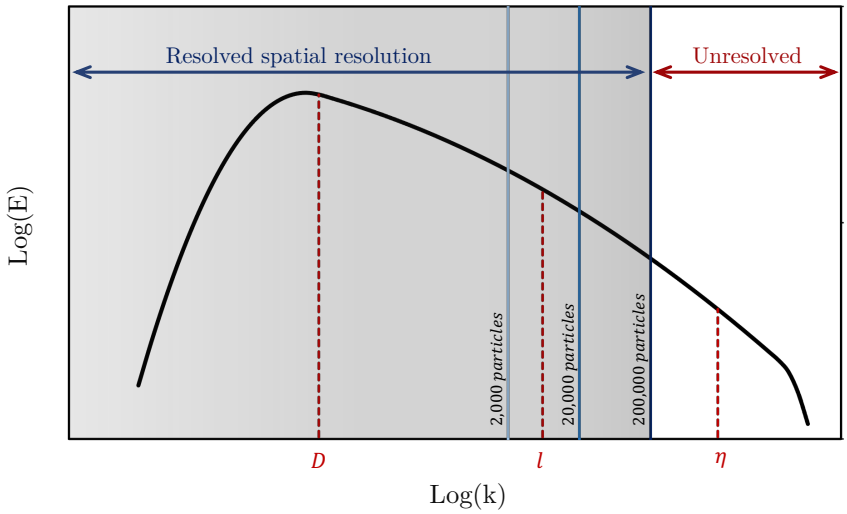

Figure 4.8 – Schematic view of energy spectrum in turbulence. Resolved and unresolved spatial resolutions of $2,000$, $20,000$, $200,000$ particles in blue lines with respect to integral (D), Taylor (l) and Kolmogorov (η) length scales in red dash-lines.

and $200,000$ particles (see table 4.5). It is possible to assess cases with more particles and reach the particle concentration up to the DNS spatial resolution numerically, but very few PTV experimental studies have reached more than $200,000$ particles in practice due to the PTV seeding and the 4D-PTV limitations. One limitation can be the IPR reconstruction that fails for higher particle concentrations [20], and therefore the whole 4D-PTV process diverges. figure 4.8 shows the turbulence energy spectrum marked by the three particle concentrations (blue lines) compared with the turbulence length scales (red dash lines). We estimated the Kolmogorov length scale as $D/\eta \sim Re^{3/4}$ that is almost 2.8 times smaller than the average mesh size in the y-direction. Since the cylinder is inside our domain, it is necessary to subtract the volume of the cylinder before computing ppη^3. Accordingly, the spatial resolution for the case with 2000 particles leads to unresolved Taylor and Kolmogorov scales. However, there are enough particles to resolve the large flow motions. Taylor length scales can be resolved by adding an order of magnitude more particles, but the smallest scales are still unresolved with 10^{-4} ppη^3. As shown in figure 4.8, in our case, even $200,000$ particles with 10^{-3} ppη^3 are not enough to resolve the smallest turbulence length scale at Reynolds number equals to 3900.

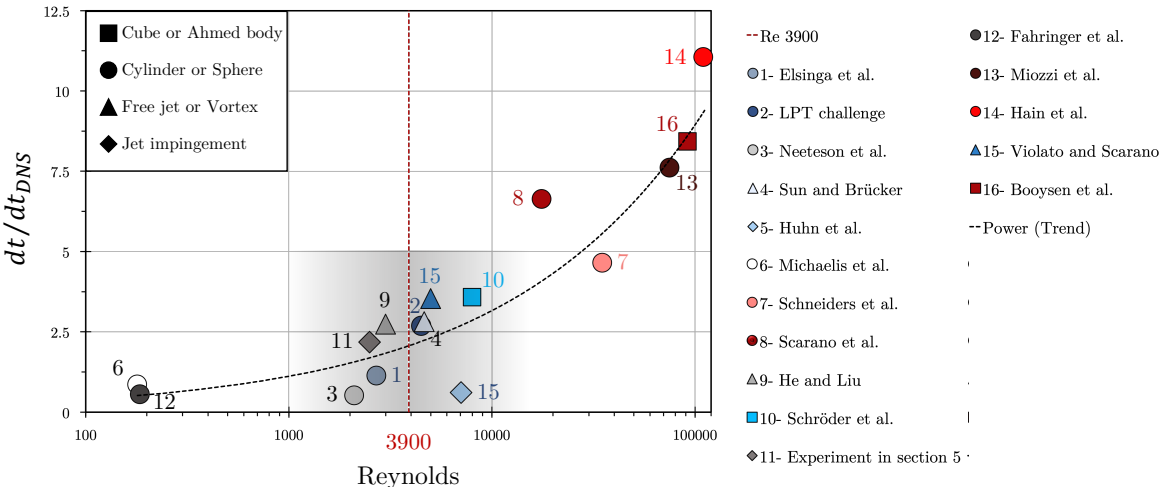

Figure 4.9 – Synthetic time scale selection with respect to recent similar wake flow experimental studies and different Reynolds numbers. Each symbol represents a family of flow configuration [14], [19], [28], [41], [81]–[91].

Temporal scale

Schanz et al. [1] computed the temporal scale as a function of the original experiment time sampling rate, resulting in a mean 3D particle displacement of around 6 pixels for the synthetic data analysis. However, the temporal scale selection requires satisfying the real experiment condition and should be characterised by flow physics. We defined the temporal resolution as a ratio of turbulence time scales. The non-dimensional form of the temporal scales can be written as dt/dt_{DNS}, dt/τ_η, and dt/T_D, where dt is the temporal scale for either synthetic or experiment study, and dt_{DNS}, τ_η and T_D are the DNS, Kolmogorov and integral time scales, respectively. By defining $T_D = D/U_\infty$, we estimate the Kolmogorov time scale from ratio of the largest to the smallest time scales as $T_D/\tau_\eta \sim Re^{1/2}$. To mimic the real experiment condition, we gathered similar wake flow studies (mainly cylinder wake flows) and plotted the relations of dt/τ_η with their Reynolds numbers in figure 4.9. It is shown that low Reynolds number experiments can resolve the Kolmogorov time scale [81]. The achievable temporal scale increases with the Reynolds number, mainly because the data acquisition frequency limits the experiments with the order of $1-3$ kHz for the majority of studies mentioned in figure 4.9. The DNS time step is roughly 20 times smaller than the Kolmogorov time scale. Such a case with every 10 DNS time step ($dt/\tau_\eta = 0.47$) can resolve the Kolmogorov time scale, but it is unlikely to achieve such a high acquisition rate in practice, particularly when the fluid is

Table 4.6 – Synthetic time step selection in terms of DNS, Kolmogorov, and integral time scales.

Case	dt/dt_{DNS}	dt/τ_η	dt/T_D
Low	10	0.47	0.01
Moderate	50	2.34	0.04
High	100	4.68	0.08

air. Particle trajectories are very smooth with small displacements in this case. However, according to figure 4.9, the temporal scale dt/τ_η stays relatively large, between 2.5 and 5 for studies close to a Reynolds number of 3900 that approximately equals to every 50 and 100 DNS time steps. As listed in table 4.6, we chose three low, moderate, and high time steps starting from every 10, 50, and 100 DNS time steps. It is worth mentioning that it takes 1333 and 6667 DNS time steps to reach one integral time scale and one vortex shedding, respectively.

Noise ratio

In this paper, we created noise (i.e., false particles) in the vicinity of true positions. A false particle is randomly distributed around the true position with a maximum displacement radius. Noise ratio (NR) of 0.1 means 10% of true particles at every time step have false particles in their vicinities. A false particle around a single track also impacts the track detection accuracy for other neighbour tracks, particularly in dense and intersection situations. In this study, we created three noise ratios, 0, 0.1, and 0.2.

4.3.2 2D Homogenous Isotropic Turbulent (HIT)

We transported synthetic particles for 2D Homogenous Isotropic Turbulent (HIT) flow obtained from DNS at a Reynolds number equal to 3000. The Navier-Stokes equation was solved using incompressible condition ($\boldsymbol{\nabla} \cdot \boldsymbol{u} = 0$). Tracer particles were transported for every DNS time step using Euler transport as,

$$\frac{d\boldsymbol{x}}{dt} = \boldsymbol{u_p}, \tag{4.1}$$

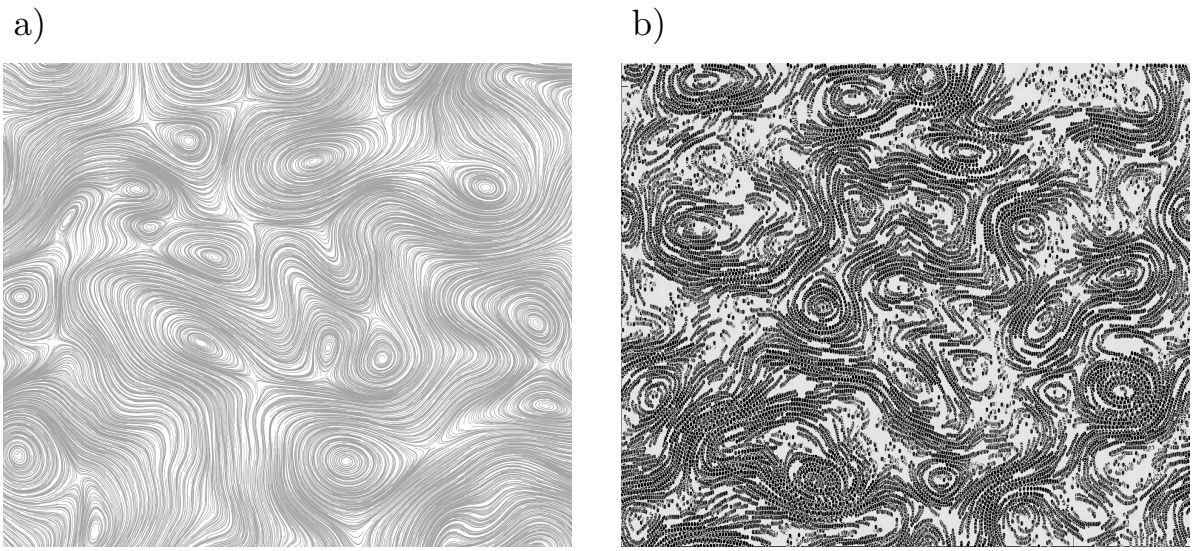

Figure 4.10 – One snapshot of 2D homogenous isotropic turbulent (HIT) flow. (a) Eulerian streamline. (b) Lagrangian trajectories.

where interpolation over four nearest mesh nodes were used to estimate the velocity of tracer particles u_p. The square domain of interest $2\pi \times 2\pi$ was discretized into 256×256 node elements with periodic boundary condition in four boundaries. This means that a particle enters in one side of the domain if a particle leaves on the opposite side at the same mirrored position. The non-dimensional DNS time step was set at 0.01 D/U. We collected particle transport of 1000 DNS time steps. Figure 4.10 shows a snapshot of both Eulerian streamline and Lagrangian trajectories. The current data set is used in further assessments in Chapter 8.

Chapter 5

Coherent Track Initialization

This section seeks to increase the track initialisation accuracy and robustness in flows with high particle concentration, large temporal scale, and noisy reconstruction featured by complex motions such as high velocity and acceleration gradients. Therefore, we propose a novel Lagrangian Coherent Track Initialisation (LCTI) technique to find tracks in four (or multi) frames belonging to clusters of coherent motions. We apply Lagrangian Coherent Structures (LCS [3]) to distinguish coherent and non-coherent neighbour trajectories. The LCS, also known as the skeleton of flow, determines separatrix lines or surfaces that divide flow structures into different coherent regions. We use finite-time Lyapunov exponent (FTLE), which is the most common method in quantifying these separatrices boundaries [59].

We argue that when a track can not be reconstructed solely due to ambiguities caused by overlapping and multiple possibilities, it is always beneficial to extract more information from its neighbourhood. If the reconstructed tracks are available in the neighbourhood, we can use this information to gain a better insight into the target particle's potential behaviour and eventually solve the ambiguity problematic associated with the initialisation. As we are dealing with the fluid flow, assuming a constant solid local rigid neighbourhood is naive and erroneous, it is essential to consider a coherent neighbourhood where both the target particle and neighbour particles share the coherent motion.

We first applied the LCTI algorithm to synthetic data as an effective tool with three specific objectives including, algorithm performance assessment, algorithm sensitivity analysis as a function of characteristic parameters, and algorithm comparison [72]. This approach has been utilised widely in recent algorithm developments of PIV/PTV studies [27], [46], [92], [93]. This section considers a set of synthetic data for the wake flow downstream of a smooth cylinder. Performance of the proposed method based on three characteristic parameters, temporal scale, particle concentration (i.e., density), and noise ratio, showed robust behaviour in finding true tracks compared to the recent initialisation algorithms. Sensitivity of LCTI to the number of untracked and wrong tracks are also

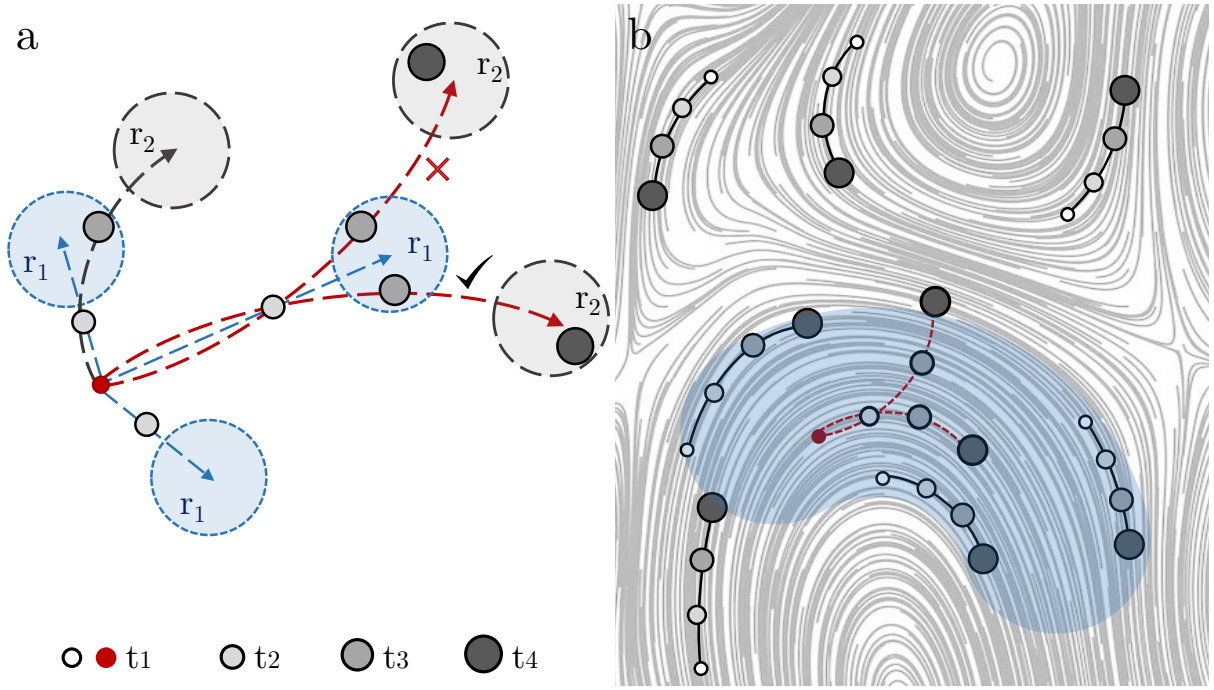

Figure 5.1 – Schematic view of the LCTI algorithm when two possible four frame solutions exist. (a) LCTI four frame algorithm considering all possible neighbour candidates at t_2 followed by linear predictions (blue dash line arrows). Candidate matching at time step t_3 inside first search volume (blue circle r_1). Second order prediction (red and black dash line arrows) to match possible candidates at t_4 inside second search volume (grey circle r_2). (b) Coherency check between two possible track matches and neighbour coherent motion.

discussed. We address the capability of using the proposed method as a function of a 4D-PTV scheme in the Lagrangian Particle Tracking (LPT) challenge for the wall-bounded wake flow behind the cylinder [5]. We showed that LCTI prevents 4D-PTV divergence in flows with high particle concentrations. Finally, the LCTI behaviour was demonstrated in a jet impingement experiment. LCTI was found to be a reliable tracking tool in complex flow motions, with a strength revealed for flows with high velocity and acceleration gradients.

5.1 Track initialisation methodology

The current initialisation technique tries to find coherent tracklets in four frames as a complementary part of 4D-PTV. It should be noted that particles of a cluster are coherent

if they spatially behave together over a finite time. A starting step is required in LCTI for the first time step t_1, where there is no neighbour track information. It can be done by a classic four-frame scheme with a narrow threshold to index the most reliable tracks. A track is assumed to be reliable if it has relatively small velocity and acceleration standard deviations in four time steps to avoid false tracks. The standard deviation of the particle image intensity can also determine whether a possible track is reliable. In practice, the LCTI steps can be listed as the following algorithm,

Algorithm 1: LCTI

1: Index possible candidates inside the search volume at t_2;
2: Two consecutive predictions and candidate matching for t_3 and t_4;
3: Index possible tracks from t_1 to t_4;
4: Coherency check with neighbour tracks for each possible track;
5: Index the most coherent track.

Referring to the LCTI algorithm 1, we need to define the search volumes to index possible candidates at each time step. Clark et al.[46] enhanced the probability of finding true tracks by applying adjustable anisotropic search volumes as a function of mean flow direction. Anisotropic means that if the mean flow (obtained from the predicted velocity) is dominant in one direction, the search volume in that direction is larger than in the other directions. Adjustable search volumes introduce local spatial motions (i.e., physics-based information) into four frame schemes, which can significantly tackle the high gradient threshold issues. On the other hand, using the adjustable search volume limits the number of possible candidates, avoiding non-coherent solutions by following the local spatial motion. The search volume in LCTI is based on the local maximum displacement map calculated from neighbour particles. Therefore, the first search volume is computed as a function of neighbour maximum displacements in each spatial direction between t_1 and t_2 as shown in figure 5.1.a. Then, every neighbour particle inside the search volume at t_2 is a candidate. These candidates are in one of the following categories: the true position of the target particle at t_2, the true position of other undetected tracks, and noise (i.e., false particle). Afterwards, a linear predictor (blue dash line arrows in figure 5.1.a) between the target particle at t_1 and the possible candidate at t_2 is performed for every possible match. Similarly, the second search volume around the predicted position determines which particles are more likely to be in the true position at t_3. A possible track is removed if there is no candidate inside the search volume. The process is repeated for the next time step with a higher order prediction function (red and black dash line arrows in figure 5.1.a).

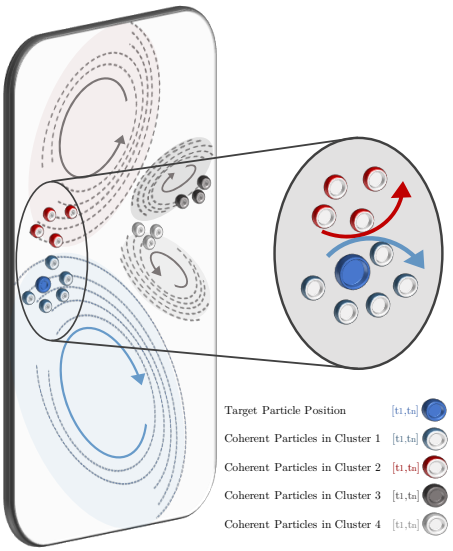

Figure 5.2 – 2D schematic of particle motions inside vortices. Each colour belongs to a group of coherent clusters. The target dark blue particle with coherent neighbour particles is located in a clockwise vortex (blue cluster), while non-coherent particles belong to different clusters. The target particle is non-coherent with neighbour particles in the red cluster.

A unique four frame solution is expected for flows with low velocity and acceleration gradients or low particle concentrations. When more than one solution exists, LCTI selects the most coherent track to solve the ambiguities, as shown in figure 5.1.b. Otherwise, a particle can spatially meet a group of other particles with no coherency link between them. We recall that coherent refers to a group of particles with the same Lagrangian behaviour spatially and temporally. A function is therefore required to determine coherent and non-coherent clusters of particles locally. More details and principles on the coherent motion of particles are discussed in Section 5.2.

5.2 Coherent track detection

Recently, LCSs have been applied in PIV/PTV experiments for flow structure analyses [94]–[97]. However, to the best of our knowledge, previous studies have not yet combined the LCS extraction with the velocimetry algorithms and primarily focused on using LCS as a post-processing tool. Several methods have been proposed to identify LCS by looking for separatrix regions in time [3], [63]. Separatrices exist in boundaries (i.e., ridges) between

different structures. A schematic view of the boundaries between vortices in a 2D isotropic homogeneous turbulent flow is shown in figure 5.2. Multi clusters of particles spatially exist in the vicinity of the target particle (the dark blue particle in figure 5.2). All red and blue particles are neighbours of the target particle. However, the trajectories of each coloured cluster temporally evolve in separated directions. LCS can be used to determine if a spatially neighbour particle is coherent or non-coherent over a temporal scale.

Suppose the flow is dominated by coherent structures such as in a 2D isotropic homogeneous turbulence illustrated in figure 5.2, the global LCS analysis can extract meaningful boundaries between structures. However, difficulties in interpretation arise when the flow carries 3D complex motions and numerous local structures. We, therefore, suggest local coherent structure extractions instead of a global calculation for which only coherent clusters and boundaries over neighbour trajectories are computed. Therefore, the complexity of the global LCS view is simplified into a small number of clusters around the target particle, such as in figure 5.2. In the local view, curve or surface boundaries divide the local spatial area into discrete regions with different dynamic motions, and motions across these boundaries are negligible [56]. Furthermore, the LCS boundaries can move, evolve, and vanish in spatial space as the flow pattern changes temporally.

In the local Lagrangian frame, separatrices can be obtained from FTLE by measuring the amount of stretching between the target particle and its neighbour particles over finite time [4], [98]. Raben et al. [4] showed that the normalised average error and normalised root-mean-squared (RMS) error of the FTLE map decreases with increased particle concentration. This trend is favourable because ongoing PIV/PTV experiments consistently succeed in achieving higher particle concentrations. Meanwhile, it is less likely to have ambiguities due to multi possible solutions in low particle concentration cases. As a result, there is no critical need for the coherency check in low particle concentration cases. As discussed in section 5.1, if a possible track is coherent with its neighbour tracks, it will be indexed into the tracked poll. As we discussed in section 5.1, the LCTI algorithm checks if the Lagrangian coherency is valid for each possible four frame tracks to avoid non-coherent reconstructions. Assuming two possible matches exist for the target particle (see figure 5.1.b), we start by fitting a smooth curve over each known neighbour track to reduce the noisy reconstruction effect on the coherency detection. Then LCTI locally computes the FTLE map over the fitted tracks without considering two possible matches. If the FTLE map shows local separations, neighbour tracks in the same cluster with the target particle are classified as coherent neighbours. As illustrated in figure 5.2, the local

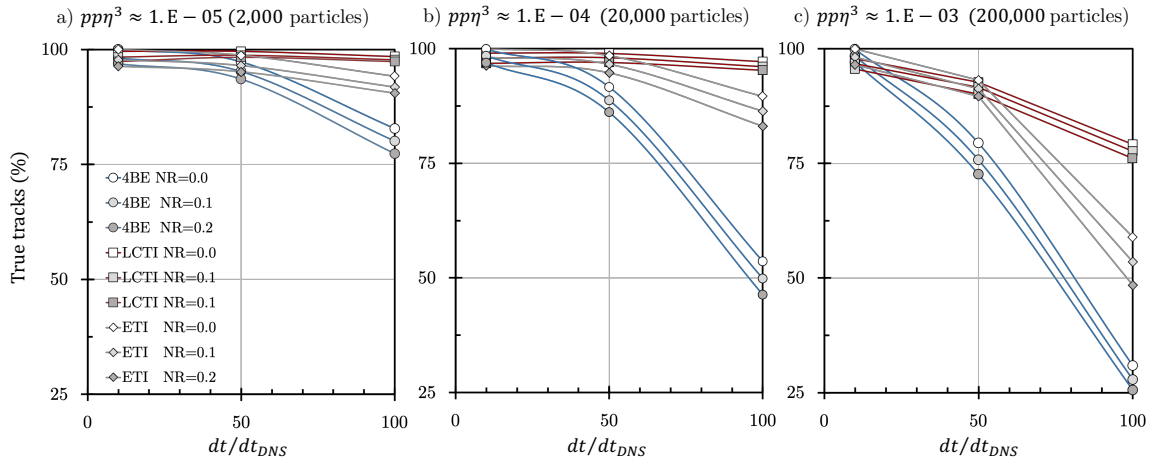

Figure 5.3 – Comparison performances of three track initialisation techniques in terms of fraction of true particle detection by changing each characteristic parameter. Particle concentration is increasing from (a) to (c).

region is divided into two blue and red clusters. Only the neighbouring tracks inside the blue cluster are coherent with the target particle. All neighbour tracks are coherent neighbours if no separation is detected. After the coherent neighbour determination, LCTI checks the FTLE value for each possible match and neighbours. Finally, the most coherent match with the coherent neighbours will be indexed. This process continues iteratively until no track is found to be coherent with the tracked poll.

5.3 Evaluation and sensitivity analyses

In this section, the performance of the LCTI is assessed and compared against ETI and 4BE-NNI methods. Quantitative accuracy and sensitivity analyses are performed for different particle concentrations, temporal scales, and noise ratios compared to the ground truth trajectories. After the initialisation step, the trajectory of each particle is classified as either untracked, wrong, or true track. A dominant number of true tracks would ease the 4D-PTV process to converge within short time steps. It is worth mentioning that a 4D-PTV process is converged if all particles inside the domain are tracked.

Figure 5.3 compares the ratio of detected true tracks obtained from LCTI, ETI, and 4BE-NNI techniques with different characteristic parameters of ppη^3, dt/τ_η, and NR. We assessed each technique based on $3 \times 3 \times 3$ scenarios representing low, moderate

and high levels of each characteristic parameter (see table 4.5 and table 4.6). The 3D view of particle trajectories for the current assessment is shown in figure 5.8.c. All three techniques performed equally well for low particle concentration and small temporal scale by reconstructing over 95% of true tracks (see figure 5.3.a). Tracking is not difficult under such scenarios characterised by small particle displacement with a relatively large spatial distance between neighbour tracks. By increasing dt/τ_η in low particle concentration cases, the ratio of detected true tracks drops down to approximately 90% and 75% in ETI and 4BE-NNI techniques, respectively, whereas LCTI remains stable. Due to low particle concentration, the large relative distance between neighbour trajectories reduces the ambiguity in finding possible tracks. Results of low particle concentration cases for all three techniques show that the 4D-PTV process has to recover less than 25% of remaining untracked particles to converge in the worst case; thereafter, a short convergence time is expected. The ratio of true tracks drops linearly by increasing the noise ratio (NR) for all techniques with approximately the same order of magnitude. We found that the drop in the detected true tracks caused by the noise ratio (NR) is nearly independent of the other two characteristic parameters. Comparing the three characteristic parameters reveals that the temporal scale has the most deterministic impact on the detected true tracks for all techniques. If dt/τ_η stays low, all techniques can cover over 95% of true tracks, regardless of the noise ratio and the particle concentration. Low temporal scale value means that particle displacements are minimal. Even two frame nearest neighbour techniques can reconstruct the majority of true tracks. However, in more realistic conditions, when the temporal scale dt/τ_η is high, LCTI performed significantly better than the other two techniques. Particle concentration also plays an essential role in the initialisation performance. The ratio of detected true tracks for LCTI stays consistently above 95% in particle concentrations of $10^{-4}\text{pp}\eta^3$ (see figure 5.3.b). In a worse scenario, when the particle concentration is $10^{-3}\text{pp}\eta^3$ associated with large temporal scale, LCTI still can recover over 75% of true tracks that is considerably higher than ETI and 4BE-NNI with roughly 50% and 25% true tracks, respectively (see figure 5.3.c).

The synthetic data evaluation showed that LCTI systematically outperforms other competing techniques. However, it should be mentioned that the cost of this achievement is expensive because it computes the coherency for every possible tracklet. We found that LCTI requires roughly 4 times more computation time on a single CPU core than a classic four frame based initialisation technique without any post-treatment. To this end, an appropriate initialisation technique should be chosen depending on the measure-

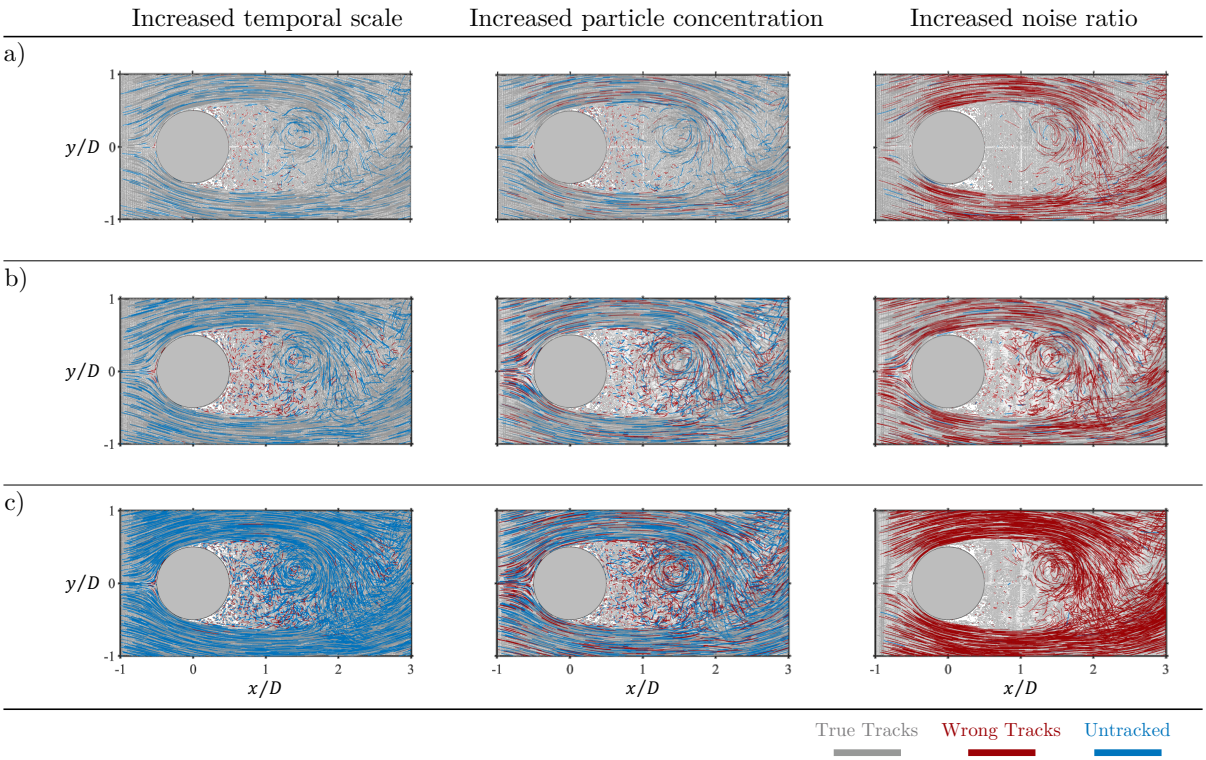

Figure 5.4 – Sensitivity analysis of (a) LCTI, (b) ETI, and (c) 4BE-NNI compared with DNS ground truth by increasing temporal scale, particle concentrations, and noise level from top to bottom. Tracks in blue and red colour represent untracked and wrong trajectories, respectively. Grey tracks are true trajectories that the algorithm built (numbers of grey tracks are scaled down for having a clear view of red and blue tracks).

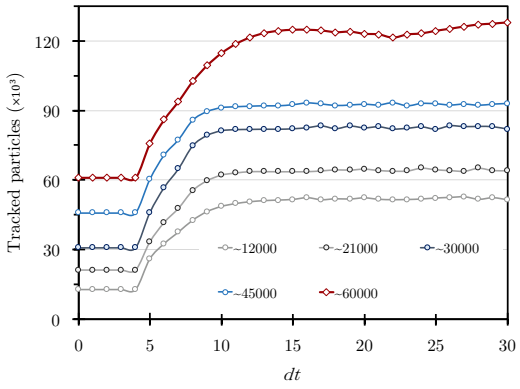

Figure 5.5 – Sensitivity of the 4D-PTV convergence to the number of initialised tracks for the LPT challenge high-density case at 0.12 ppp over first 30 time steps. The number of initialised tracks after the first four frames varies from $\sim 12,000$ to $\sim 60,000$.

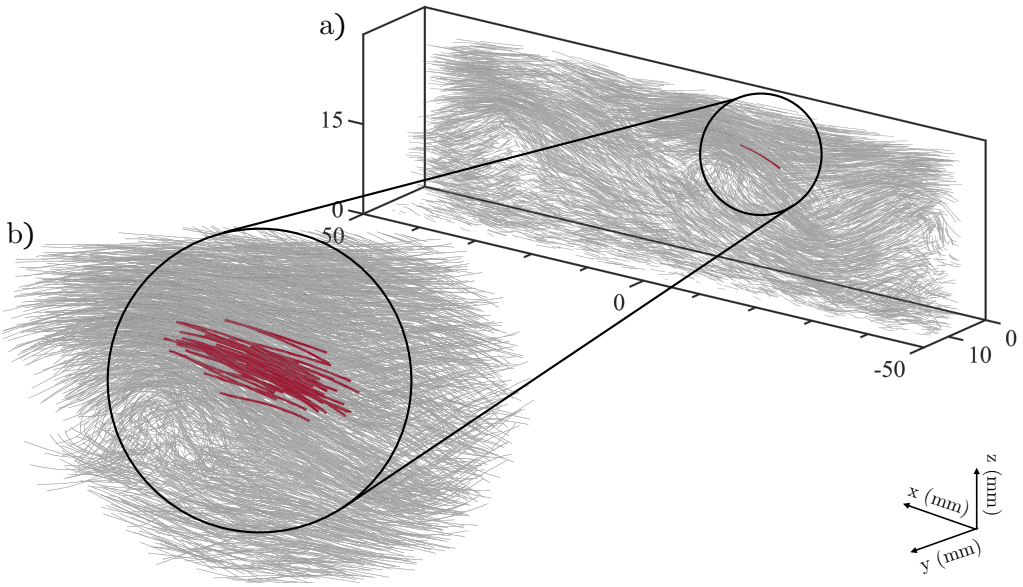

Figure 5.6 – LCTI trajectory results for the LPT challenge wake flow at 0.12 ppp ([86], [99]). (a) slice view in y direction of particle trajectories in grey and the target track in red. (b) A cluster of coherent tracks with the target track in red.

ment condition. As an example, there is no need to perform a sophisticated initialisation technique if the temporal scale (i.e., sampling rate) and the particle concentration are low in comparison with the turbulence scales. It is important to note that using sophisticated initialisation techniques such as LCTI is crucial to prevent 4D-PTV failure in challenging cases with a large temporal scale and high particle concentration. Apart from the initialisation performance based on the number of true tracks, we performed further parametric analyses on each technique to determine how untracked and wrong trajectories are sensitive to the characteristic parameters. We started LCTI from a base case with 10^{-4} ppη^3 particle concentration, $dt/\tau_\eta = 2.34$, and zero noise ratio. Afterwards, we increased each parameter separately until the fraction of true tracks dropped down to 80%. The remaining 20% is a mix of untracked and wrong trajectories. Then we performed the same parameters on 4BE-NNI and ETI techniques. Lagrangian flow maps for increasing each characteristic parameter are shown in figure 5.4. If we increase the temporal scale, both untracked and wrong tracks increase as the number of true tracks drops. Under such a scenario, the particle displacements are large and comparable with local distances between the neighbour particles. Therefore, less information between two-time steps is available, which drastically increases the possibility of having untracked particles.

Depending on the region of the flow, the majority of untracked trajectories (blue colour in figure 5.4) exist around the two high shear sides of the wake region. Although the number of untracked trajectories dominates the whole Lagrangian flow map, more wrong tracks (red colour in figure 5.4) than untracked trajectories are observed inside the wake region. By increasing the particle concentration, both untracked and wrong trajectories raise homogeneously with nearly the same proportion through the Lagrangian flow map for all three techniques. Interestingly, the number of wrong tracks is still comparably larger than the number of untracked particles inside the wake region. It shows that regional flow behaviours can directly impact the initialisation performance. The impact of increasing the noise ratio is also shown in figure 5.4. We found a dominated number of wrong tracks in all regions with an increased noise ratio. In this study, we created the noise (i.e., false particles) in the vicinity of true particles that causes more initialisation ambiguities. Due to this reason, LCTI yields more wrong trajectories with an increased noise ratio. Besides, wrong indexing of a track takes away at least one true or false particle that may propagate the wrong detection to another neighbour track too. In practice, for 4D-PTV, wrong initialised tracks increase the failure risk and need to be appropriately eliminated in a subsequent prediction-optimisation step. The untracked particles, on the other hand, require more iteration and convergence time.

Sensitivity analysis in figure 5.4.a implies that LCTI is likely to have more wrong tracks inside the wake region with increased noise ratio, particle concentration, and temporal scale. However, different behaviours have been seen depending on the characteristic parameters in overall. The high turbulence intensity level at Reynolds 3900 creates small flow structures inside the wake region. Consequently, particles inside this region are coherent with a small number of neighbours and quickly change to different coherent clusters. This behaviour brings more complexity for the coherency detection, which might be the reason for having a dominating number of wrong tracks, despite relatively small particle displacements. Schanz et al. [38] observed a similar issue when particles of a specific region move slowly compared to the rest of the domain. One approach for improving trajectory in such regions is performing temporal filtering schemes by adjusting the temporal scale to track the slowest particles [38]. Comparing the LCTI sensitivity with the other two techniques shows that both 4BE-NNI and ETI have similar behaviours to each characteristic parameter with higher proportions of untracked and wrong trajectories (see figure 5.4.b.c). The reason for having a higher mix of untracked and wrong trajectories can be found in figure 5.3. A drop in the number of true tracks with increased character-

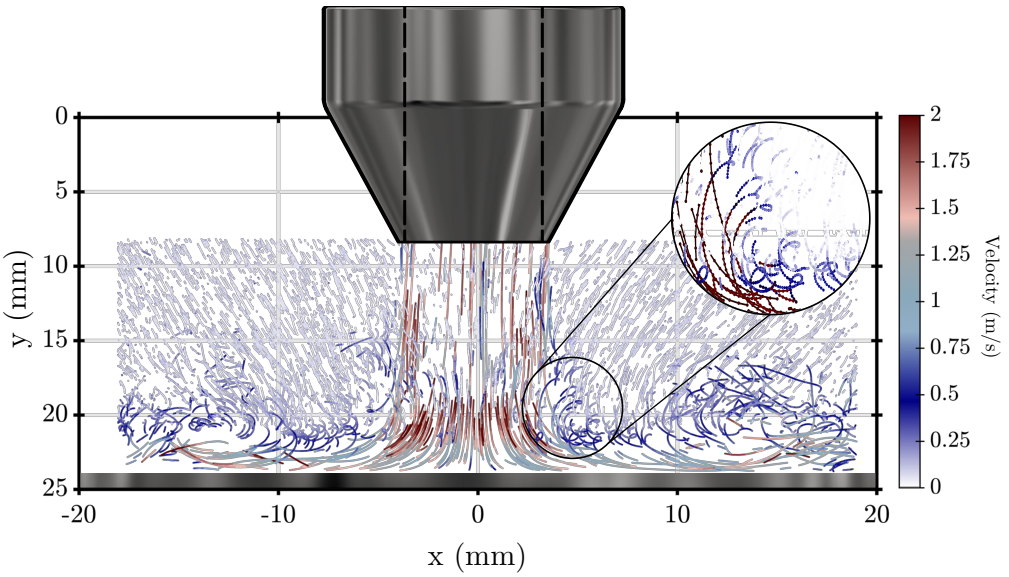

Figure 5.7 – Side view of the trajectories, coloured by their velocity magnitudes at 0.03 ppp. Low-velocity tracks away from the jet core are filtered for clear qualitative view thanks to the colour bar.

istic parameters leads to more untracked and wrong trajectories, which is in agreement with findings of figure 5.4.

5.3.1 LPT challenge

LCTI was implemented into KLPT [2] to run the whole 4D-PTV process (see figure 2.1). KLPT featured by LCTI (KLPT-LCTI) was examined on the time-resolved data from the LPT challenge [86], [99] at four particle densities (i.e., concentrations) from 0.005 ppp up to 0.08 ppp. The challenge cases were obtained from the wall-bounded wake flow behind a cylinder at a momentum thickness Reynolds number Re_θ of around 4500. In terms of turbulence length scales, particle concentration of the mentioned four cases varied between 2×10^{-7} ppη^3 and 3×10^{-6} ppη^3. The domain of interest was set at 100 mm $\times$ 50 mm $\times$ 30 mm downstream of the cylinder. The image acquisition rate was equal to 600 μs, resulting in $dt/\tau_\eta = 2.68$ temporal scale. At the lowest ppp, the proposed method managed to reconstruct over 99% of true particles accurately. Percentage of true particles maintained over 99% for higher densities (i.e., 0.025, 0.05, and 0.08 ppp). Accordingly, missed and ghost particles were less than 1%. The case studies of the LPT challenge revealed that the positional Root-Mean-Square error (RMSE) of KLPT-LCTI

increased linearly with ppp, but it remained below 0.0041 mm for all four particle densities. This illustrates the reliable performance of the LCTI at particle densities lower than 0.08 ppp, knowing that most of the 4D-PTV real experiments perform at 0.05 ppp particle density or lower.

For densities higher than 0.08 ppp, a more accurate initialisation technique could prevent the 4D-PTV algorithm from failing or improve its convergence speed. We highlighted that KLPT featuring LCTI succeeded in reconstructing tracks at the density of 0.12 ppp while KLPT featuring NNI failed to converge. figure 5.6 shows an example of coherent motion detection by LCTI at the density of 0.12 ppp. The particle trajectories obtained from the proposed method are shown in figure 5.8.a. Questions have been raised about the 4D-PTV sensitivity to the number of initialised particles at the beginning. We illustrated this issue in the LPT challenge case with 0.12 ppp and over $120,000$ particles. As shown in figure 5.5, the KLPT-LCTI process reaches no more than $85,000$ (i.e., 70%) final tracks if the process starts with any number below $30,000$ initialised tracks. However, starting with $60,000$ initialised tracks leads to cover over 99% of final trajectories after 30 time steps at 0.12 ppp. The evidence from this study indicates that the number of initialised tracks is one deterministic contributor to the 4D-PTV convergence at high-density scenarios. Without a proper track initialisation algorithm, a 4D-PTV scheme would not be able to recover the majority of tracks eventually.

5.4 Experiment demonstration

In this section, we performed the 4D-PTV process without prediction and optimisation parts to particularly demonstrate the LCTI performance. Therefore, the reconstructed particle positions with 1 pixel allowed triangulation error by IPR were employed in 20 consecutive time steps followed by multi four-frame LCTI processes. Trajectory results obtained from LCTI are shown in figure 5.7 and figure 5.8.b. Away from the jet impingement region, the trajectories are relatively smooth with small displacements. As explained earlier in section 5.3, there is no critical issue in such regions, and a simple initialisation technique can track the majority of particles. Small trajectories away from the jet, therefore, are omitted in figure 5.7 to concentrate on the most complex regions. As the jet impinges on the wall, trajectories decelerate highly, turn alongside the wall, but still tend to keep their coherent local motions. The proposed method effectively detected these coherent trajectories, although complex behaviours exist. We found that the

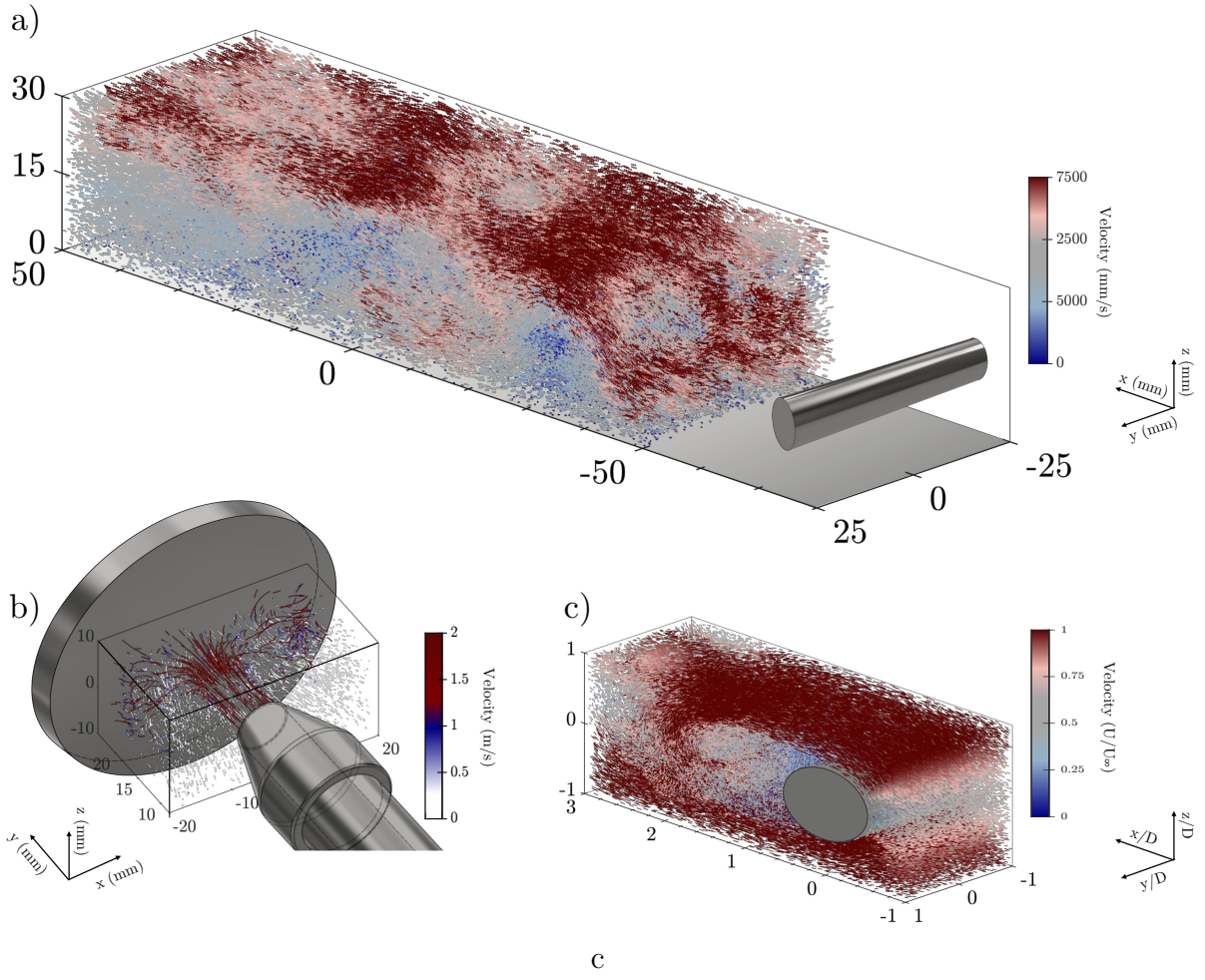

c

Figure 5.8 – 3D view of particle trajectories. (a) The LPT challenge downstream trajectories of the wall bounded flow in the wake of a cylinder at ppp = 0.12. (b) Jet impingement experiment case study. (c) Synthetic case for the wake behind a smooth cylinder.

trajectories around the jet tend to circulate (see the zoom balloon in figure 5.7). This reveals strong evidence of the particle coherent motions impacted by the vortex rings. Near wall trajectory reconstructions show signatures of the secondary vortices where particles bounce back. The results of this experiment test case support the idea that each particle can temporally and spatially behave in coherence with a group of other neighbour particles. The second significant finding was that the proposed initialisation technique could cover most tracks in complex and high gradient regions associated with 3D directional dynamics.

5.5 Conclusions

We proposed a novel technique to reconstruct tracklets from four (or multi) frames by leveraging temporal and local spatial coherency of neighbour tracks. These tracks should be consistent with the neighbour coherent motions bounded by LCS ridges. To assess the LCTI performance in various conditions, we have created an open-access synthetic dataset for the wake flow downstream of a smooth cylinder obtained from DNS at a Reynolds number equal to 3900. Future studies by interested readers should focus on using the current open access Eulerian velocity and pressure data as well as synthetic Lagrangian trajectories for algorithm evaluation purposes (see Chapter 4). We transported particles using the trilinear spatial interpolation scheme followed by the fourth order Runge Kutta temporal integration. In the current dataset, temporal and spatial scales are reported based on turbulence length and time scales. As a result of the parametric study in section 5.3, we found that a 4D-PTV process requires more sophisticated initialisation techniques if either one of the following conditions meets:

— Particle displacements between two time steps are relatively large (i.e. $dt/\tau_\eta > 2.34$) due to either sparse temporal acquisition frequency or high dynamic gradients of particles (velocity and accelerations);
— The particle concentration is high enough to have a length between neighbour particles with the same order of their trajectory displacement lengths that can be quantified as $\mathrm{pp}\eta^3 > 10^{-3}$ in this study;
— The reconstructed particle field is noisy (NR$>$ 0.2).

Under these conditions, LCTI tends to detect more true tracks than recent ETI and 4BE-NNI techniques. We found that the temporal scale severely impacts the true track detection yielded by any initialisation techniques. We also analysed the proportions of

untracked and wrong trajectories. The main results indicate that the noise ratio creates more wrong tracks, the particle concentration homogeneously increases both untracked and wrong tracks, and finally, the temporal scale causes more untracked trajectories. Regardless of the characteristic parameters, we found more wrong trajectories than untracked particles inside the wake region.

We also applied LCTI to the time-resolved dataset in the LPT challenge after integrating LCTI to a 4D-PTV scheme, KLPT. Our KLPT-LCTI scheme has achieved state-of-the-art performance. The positional Root-Mean-Square error (RMSE) of the proposed method stayed between 0.0020 mm and 0.0041 mm for particle densities of 0.005 ppp up to 0.08 ppp [86], [99]. LCTI is helpful for high particle density data where the portion of initialised tracks after the initialisation stage directly impacts the 4D-PTV's convergence performance. At ppp = 0.12, KLPT featuring a simple nearest neighbour initialisation scheme fails to yield any valid results. LCTI, on the contrary, can recover much more tracks from the starting four frames, therefore providing a more accurate initialised track field. Besides, LCTI also contributes to following every frame by bringing more new tracklets (length less than 4) from triangulated particles on residual images into the tracked poll (see figure 2.1). This finding agrees with the synthetic analysis part in section 5.3 showing the importance of having an advanced initialisation for dense (i.e., high particle concentration) conditions.

LCTI was then tested on the jet impingement experiment. Although the flow was characterised by complexities such as 3D directional motion and trajectory intersections, LCTI successfully reconstructed the majority of tracks solely on particle fields reconstructed by IPR, without the necessity of further prediction and optimisation processes. The trajectory results also showed particles coherent motions in large scale flow motions such as vortex rings, impinging area, and secondary vortices. This comprehensive study has demonstrated that coherency based track initialisation is a robust approach to reconstruct tracks even in complex situations. In conclusion, the proposed technique can be used either as an embedded module for the 4D-PTV process or as a standalone four-frame-based tracker. LCTI showed that additional physics-based information increases the accuracy and robustness of the initialisation part.

Chapter 6

Particle Position Prediction

In Chapter 5, we showed that adding temporal and spatial information of coherent motions around the target particle can improve the initialisation robustness and efficiency. This chapter addresses how to predict Lagrangian particle positions from the initialised trajectories as the next step of the 4D-PTV process (see section 2.1). The key improvement in STB [1] compared with the original IPR [20] is adding a prediction function that receives 3D reconstructed positions and estimates positions of the next time step. A simple prediction approach is a polynomial function, suggested by Schanz et al. [54], resulting in reasonable predictions and 3D trajectory reconstructions in simple flows [52]–[54]. However, significant off prediction occurs in case of flow associated with complexities such as high turbulence level and high Reynolds number [100]. In such conditions, even by increasing the order of the polynomial predictor functions from 3 to 10, off prediction stays remained [100]. The solution for this challenge is implementing optimal temporal filtering such as the Wiener filter, which has been first examined in 4D-PTV experiments by Schröder et al. [53]. Since then, this concept became consistent in the STB studies due to its high robustness and accurate motion estimations [100], [101]. As mentioned, the Wiener filter showed robust behaviour in prediction with complex flows such as inside the turbulent boundary layer [102], but still suffers in high motion gradients. This implies that the prediction function sticks out from a lack of information to estimate the dynamics of particles. These prediction-based tracking techniques rely on one particle individually, excluding it from surroundings. All the information we know from an individual particle is its history. Even if we implement filtering and smoothing schemes such as STB using Wiener filter [101], our information is limited by the history of the target particle, ignoring that every particle is spatially and temporally coherent with a specific group of other particles following the same behaviour.

Essentially, position histories of already tracked and newly initialised particles are the main input ingredients of the prediction process, as shown in figure 6.1.a.b. Then, the predictor fits a smooth curve over the noisy history $\{t_1, \cdots, t_n\}$ of the target particle

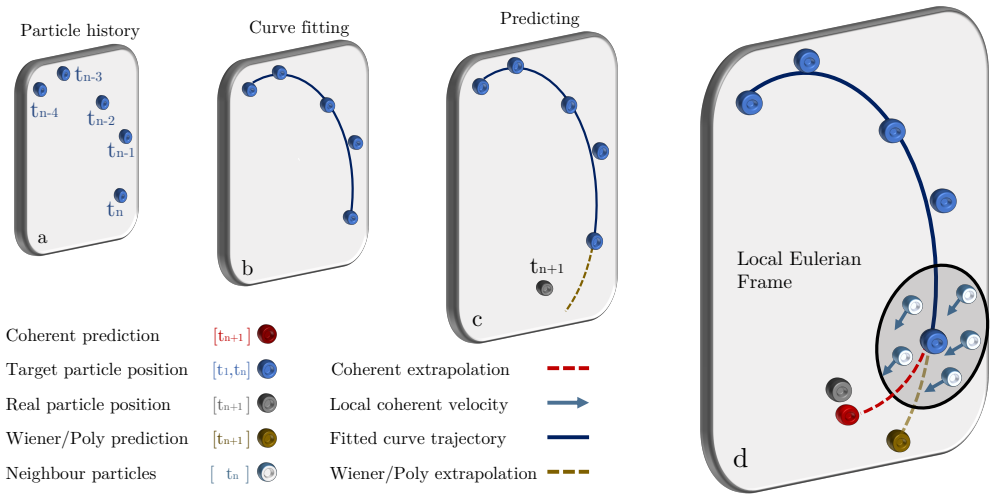

Figure 6.1 – Particle position prediction scenario from t_n to t_{n+1}. (a) Known particle positions from history starting from t_{n-4} up to t_n (particle size is increasing gradually by time step). (b) The trajectory (dark blue line) obtained from filtered curve fitting of known particle positions. (c) Prediction based on extrapolating of the fitted trajectory (golden dashed line) from t_n to t_{n+1}. (d) Modified prediction (red dashed line) using velocity and acceleration information of coherent neighbours of the target particle at t_n.

and estimates its possible position at time step t_{n+1} (see figure 6.1.c). The predicted particle positions are then given to the optimisation process for further corrections. The optimisation can deal with slight deviations between the predicted and true positions (see figure 2.5). However, the optimisation fails to find the true position if the deviation is large enough to have multi-candidates for a single particle at the next time step. This shows the importance of appropriate prediction in dense and complex motions. Following the success in utilising LCS in the initialisation step, we can extend the coherent motion applicability to the prediction step. To this end, we propose to locally determine information of coherent and non-coherent particles during the tracking procedure by using the FTLE or particle clustering schemes as shown in figure 6.1.d. We found that even a weak signal from coherent neighbour motions improves particle prediction accuracy in complex flow regions. Synthetic analysis of homogeneous isotropic turbulent (HIT) flow at a Reynolds number equal to 3000, and the wake behind a smooth cylinder at a Reynolds number equal to 3900 showed enhanced estimation compared with the recent predictor functions employed in 4D-PTV. More details of predictor functions are discussed in section 6.1. In the following sections 6.2 and 6.3, we study and evaluate our proposed technique using 2D and 3D synthetic case studies. After that, we address the generic cost function to

optimally predict particle positions and its minimisation procedure in section 6.4. The proposed predictor function is examined in a real 4D-PTV experiment in section 6.5. Results of the experimental study of the same wake flow configuration are reported. We compared predicted positions with the optimised final positions of STB. It was found that the Lagrangian coherent predictor succeeded in estimating particle positions with minimum deviation to the optimised positions.

6.1 Prediction function

The prediction function is a set of coefficients and independent variables. The coefficients are employed to predict the outcome of a dependent variable, which can be written in the form of a cost function. Therefore, the objective is to minimise the cost function to reach the optimal prediction at time t_{n+1}. Depending on the predictor function, the minimisation process can be complicated. We classify recently available prediction functions, based on the input information they require, into two categories of position based and variational cost functions. Details of these cost functions are discussed in the following sections.

6.1.1 Position based cost function

Two main position-based methods have been reported in the 4D-PTV algorithms, polynomial and Wiener filter predictors [1], [2], [27]. Both techniques only rely on the history of the target particle. Polynomial predictor tries to minimise the least mean square of the history to find the optimal polynomial coefficients, then extrapolate the function with the same coefficients to the next time step. The polynomial function is one of the most straightforward predictors used in the time-resolved particle tracking techniques. In the Wiener filter approach, we design and adjust filter parameters based on history and then shift the designed filter solution to the next time step. Both Wiener filter and polynomial predictor functions require two parameters to set. The polynomial (or filter) order and the length of history that we consider for the computation to perform the Linear regression analysis. The regression window length (history) should be determined by the desired integral time T. Then, we should select the order of the polynomial (or Wiener) function.

The polynomial coefficients must be determined optimally by minimising mean square

error, such that the corresponding polynomial curve with an order of ℓ best fits the given positions. This can be written as

$$\sum_{j=0}^{\ell} a_j.t_n^j = X_n, \tag{6.1}$$

where $\{a_0, \cdots, a_l\}$ are unknown coefficients of the predictor function and X_n is the polynomial position estimation at time step n. Therefore, the least square cost function is

$$\mathcal{J} = \underbrace{\frac{1}{m} \sum_{i=(n-m)}^{n} (X_i - y_i)^2}_{\text{particle history}}, \tag{6.2}$$

where y_i are m known observed positions (history) of the last finite frames (in this study, $m \geqslant 4$). For simplicity, observation starts from the first time step for the rest of derivations $\therefore\ i = \{1, \cdots, n\}$. The objective is to find unknown polynomial coefficients by minimising the cost function in equation (6.2) as

$$\begin{cases} \mathbf{a} = \arg\min_{\mathbf{a}} \mathcal{J}(\mathbf{X}, \mathbf{y}), \\ \mathbf{X} = \{X_1, \cdots, X_n\}, \\ \mathbf{y} = \{y_1, \cdots, y_n\}, \\ \mathbf{a} = \{a_0, \cdots, a_l\}. \end{cases} \tag{6.3}$$

In the finite impulse response (FIR) Wiener filter approach, as a short-term linear prediction model, we first design a linear estimator (filter) for history of the target particle. Consider the signal u_n is given to a Wiener filter of order ℓ as

$$\sum_{j=1}^{\ell} w_j.u_n = X_n, \tag{6.4}$$

where w_j are the filter parameters and the filter output is indicated by X_n. The objective is to minimise a quadratic cost function with the mean square error (MSE)

$$\mathcal{J} = \underbrace{\sum_{i=1}^{n} (X_i - y_i)^2}_{\text{particle history}}, \tag{6.5}$$

with respect to the parameters w_i. Similar to the polynomial solution in equation (6.3),

the objective is to find $\{w_1, \cdots, w_\ell\}$ filter parameters that minimises equation (6.5). The resulting Wiener filter in equation (6.5) is a linear minimum mean square error (LMMSE) estimator. Then we predict the future signal value (i.e., particle position) with the designed filter parameters at t_{n+1}. Predicting a signal from its past samples depends on the autocorrelation function in equation (6.4), or equivalently the bandwidth and the power spectrum of the signal. Schanz et al., [1] showed that the Wiener filter is able to predict Lagrangian trajectories by employing the mentioned autocorrelation functions. On the other hand, a Wiener filter forecasts the amplitude of a signal at a short time using a linearly weighted combination of past samples (i.e., history).

6.1.2 Variational cost function

A variational cost function adds information obtained from temporal and local spatial Lagrangian coherent motions to come up with extra constraints for the position based cost function in equation 6.2. Each particle carries sets of information, including position, first and higher-order derivative values (i.e., velocity and acceleration). Assuming positions of at least four time steps n are known. We impose each coherent particle position's first and second-order derivatives into the prediction function. Therefore, the cost function of each particle will end up with the weighted average of local coherent velocity and acceleration values ($\dot{y}_n^c$, $\ddot{y}_n^c$). We can take a minimum of four-time step histories of particles to minimise the cost function and predict the next step. Imposed coherent velocity and acceleration terms create additional constraints to equation (6.2). Therefore, the modified cost function, called coherent predictor in the present study, can be written as

$$\mathcal{J} = \frac{1}{n}\sum_{i=1}^{n}(X_i - y_i)^2 + \underbrace{\left(\dot{X}_n - \dot{y}_n^c\right)^2}_{\text{coherent velocity}} + \underbrace{\left(\ddot{X}_n - \ddot{y}_n^c\right)^2}_{\text{coherent acceleration}} \quad . \tag{6.6}$$

In the worst-case scenario where there is no coherent neighbour information, the prediction function is just a simple polynomial predictor without additional constraints. It is worth mentioning that the velocity constraint controls the direction of the estimated position. In contrast, a second-order constraint controls how far or near the prediction can go in the same direction in the case of high acceleration variations. If all three terms of equation (6.6) have exact weights, the linear solution of the prediction function is in three sets of equations as

$$\begin{cases} \sum_{j=0}^{\ell} a_j.t_i^j = y_i, \qquad i = 1, \cdots, n, \\ \\ \sum_{j=1}^{\ell} a_j.(j).t_n^{j-1} = \dot{y}_n^c, \\ \\ \sum_{j=2}^{\ell} a_j.(j).(j-1).t_n^{j-2} = \ddot{y}_n^c. \end{cases} \tag{6.7}$$

The first sets are rows of particle position history for n time step observations. The second and third sets are additional coherency based constraints. Therefore, the solution for the cost function in equation (6.7) is not only smooth on the history of the target particle but also satisfies local coherent variational dynamics of the flow. To obtain two coherent $\dot{y}_n^c$, $\ddot{y}_n^c$ terms, neighbour trajectories need to be identified as coherent or non-coherent with the target particle. In Chapter 5, we employed LCS metric locally for particle segmentations and coherent neighbour identifications over sparse trajectories. Computation of coherent neighbour trajectories is also addressed in section 3.2. As a result, we can first identify coherent neighbour trajectories and then obtain the weighted averaged values of the first and second-order derivatives over all coherent neighbours based on their FTLE values and inverse of their Euclidean distances to the target particle.

Multi-pass prediction

Referring to the 4D-PTV working principle in section 2.1, the predicted particle positions are followed by shaking or other optimisation techniques [1] [2]. Therefore, all particles are eventually either tracked or untracked, except for inlet and outlet trajectories. In every time step, untracked particles are like additive noises and might gradually cause collapsing the whole trajectory process. Therefore, untracked particles must be reconstructed by other complementary treatments.

As discussed in section 3.2, coherent predictor indexes neighbour trajectories as coherent or non-coherent within the same interval time from t_1 to t_n. In the present study, these trajectories are called primary spatial/temporal coherent neighbours. As shown in figure 6.2.a, primary coherent neighbours follow a similar path with the target particle during the same period (same phase). However, there is still the possibility of having a secondary group of coherent particles with a phase delay. Secondary refers to neighbours that were coherent with the target particle with the phase delay. Schematics of secondary coherent neighbours with one and two time step phase delays are shown in figure 6.2.b.c. The multi-pass approach computes these secondary coherent neighbours. One and two

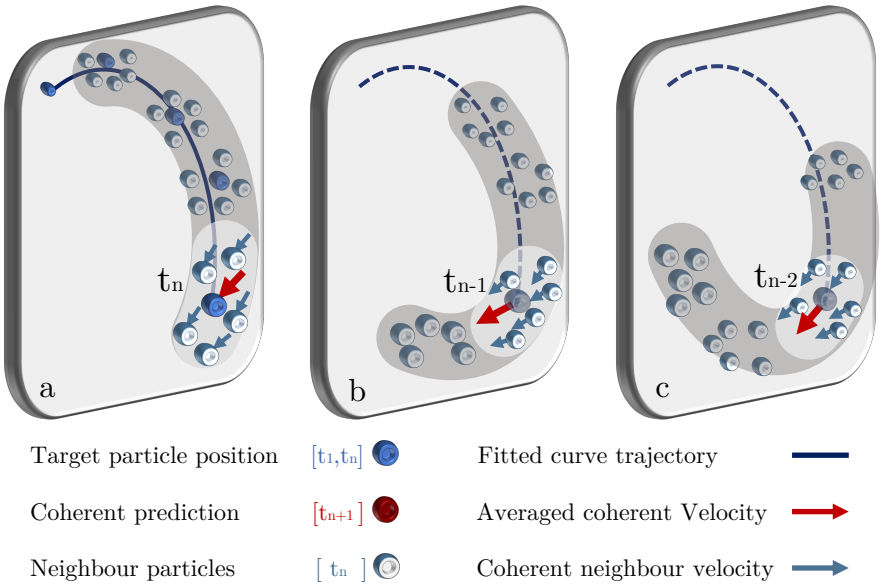

Figure 6.2 – Prediction using primary and secondary coherent particles. (a) Primary coherent. (b) Secondary coherent with one time step delay. (c) Secondary coherent with two time step delay.

time step phase delays mean that there are groups of particles that were spatially located in the neighbourhood of the target particle at t_{n-1} and t_{n-2}, respectively. Then the FTLE function determines secondary coherent neighbours between the target particle at t_n and the secondary particles at t_{n-p} where p is the time delay. In the case of steady flow, secondary coherent particles show the exact trajectory of the target particle; however, the uncertainty of relying on information obtained from the secondary coherent neighbours increases by having more unsteadiness in the flow.

The proposed multi-pass approach contains a minimum of three prediction/optimisation steps. The first pass takes primary and secondary coherent neighbours into a forward prediction (in time) from t_n to t_{n+1}, as shown in figure 6.3. The second pass takes newly tracked particles, resulted from the first pass, to the coherent detector operation (2nd forward prediction/optimisation). On the other hand, updated information is extracted if any groups of newly tracked particles are found to be located in the neighbourhood of untracked particles with one time step phase delay (i.e., t_{n+1}). This phase delay means new tracked particles at time step t_{n+1} are locally coherent with one specific untracked particle at time step t_n. In the third pass, we use backward prediction to reduce the

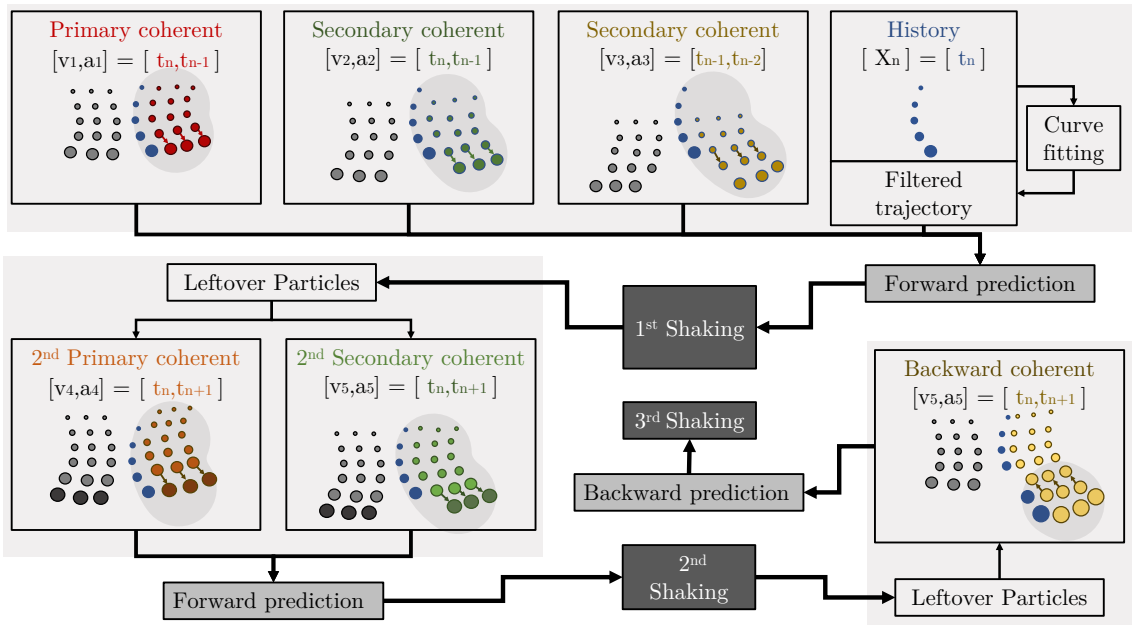

Figure 6.3 – Multi pass prediction working principle.

number of untracked particles, which is well established in classic 2D-PTV schemes such as the nearest neighbour (see, e.g., [103]). A schematic of backward prediction in 2D pair vortices starting from t_{n-4} to t_{n+3} is shown in figure 6.4. We implemented the backward predictor to search for additional information from the coherent particles to estimate in reverse pace followed by optimisation. Surrounding information of an untracked particle can provide the least signal to predict at a backward pace. In addition, this treatment can also connect spilt tracklets for reconstructing longer particle trajectories. This multi-pass process is iterative, meaning that every forward step is embedded with a series of backward estimations.

6.2 2D homogeneous isotropic turbulent evaluation

We first evaluated our proposed prediction function with 2D synthetic Lagrangian trajectories. The 2D-HIT synthetic data, discussed in section 4.3, is employed as the ground truth particle positions. Numerous flow dynamics such as saddle points, shear flows, and vortices occur inside the 2D-HIT case, bringing more challenges in accurately predicting the flow motion. We are interested in analysing the impact of using Lagrangian

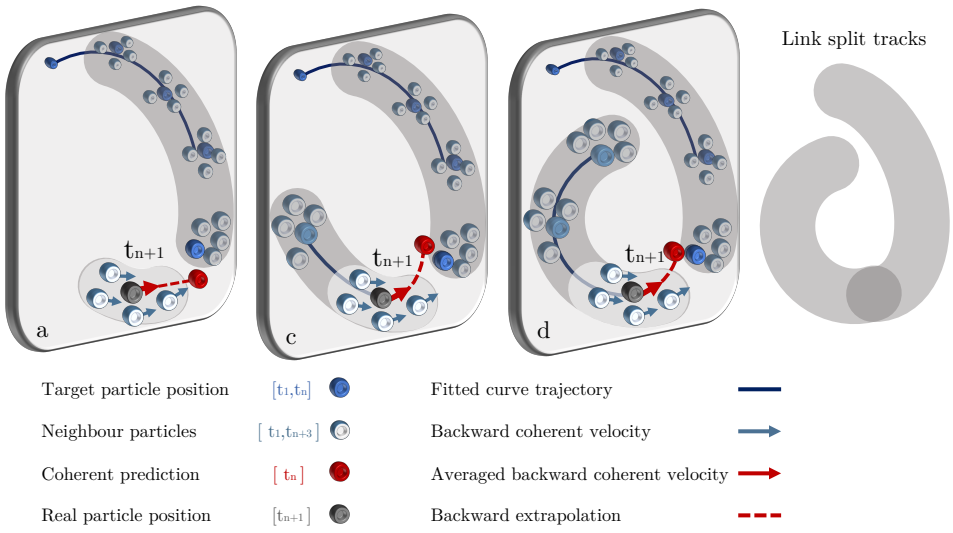

Figure 6.4 – Schematic of backward prediction. (a) Using coherent velocity of a lost particle (in grey colour). (b), (c) Backward prediction of a split track using its neighbour velocities.

coherency in 2D tracking cases. The current assessment uses three predictor functions: polynomial, Wiener filter, and coherent predictor. As mentioned earlier, 2D-HIT carries a range of complex flow motions inside where numerous vortices interact with each other. Figure 6.5.a shows one example of two trajectories extracted from 2D-HIT. The first one is for a smooth motion, where all predictor functions can estimate the next position with a negligible bias error. However, the bias error can significantly increase without knowing the surrounding flow motions as soon as a particle starts rotating with both velocity and acceleration changes. As shown in figure 6.5.b, both lower and higher order polynomial functions as well as the Wiener filter off predict high variational dynamics of particles. The third order polynomial predictor estimated the correct direction of the particle at time step t_{n+1}. However, right direction estimation does not necessarily lead to a proper prediction. Off prediction in the third order polynomial, mainly caused by lack of correct acceleration estimation. Two other polynomial cases showed less accurate estimations. On the other hand, coherent predictor has correct acceleration and direction estimations due to imposed additional constraints in its cost function. In the present study, further assessments and comparisons are conducted with the third order polynomial predictor function. We found that the third order polynomial function best compromises the bias accuracy and the uncertainty level, which will be addressed in the following sections.

In the further step, we examine the performance of the proposed predictor functions in

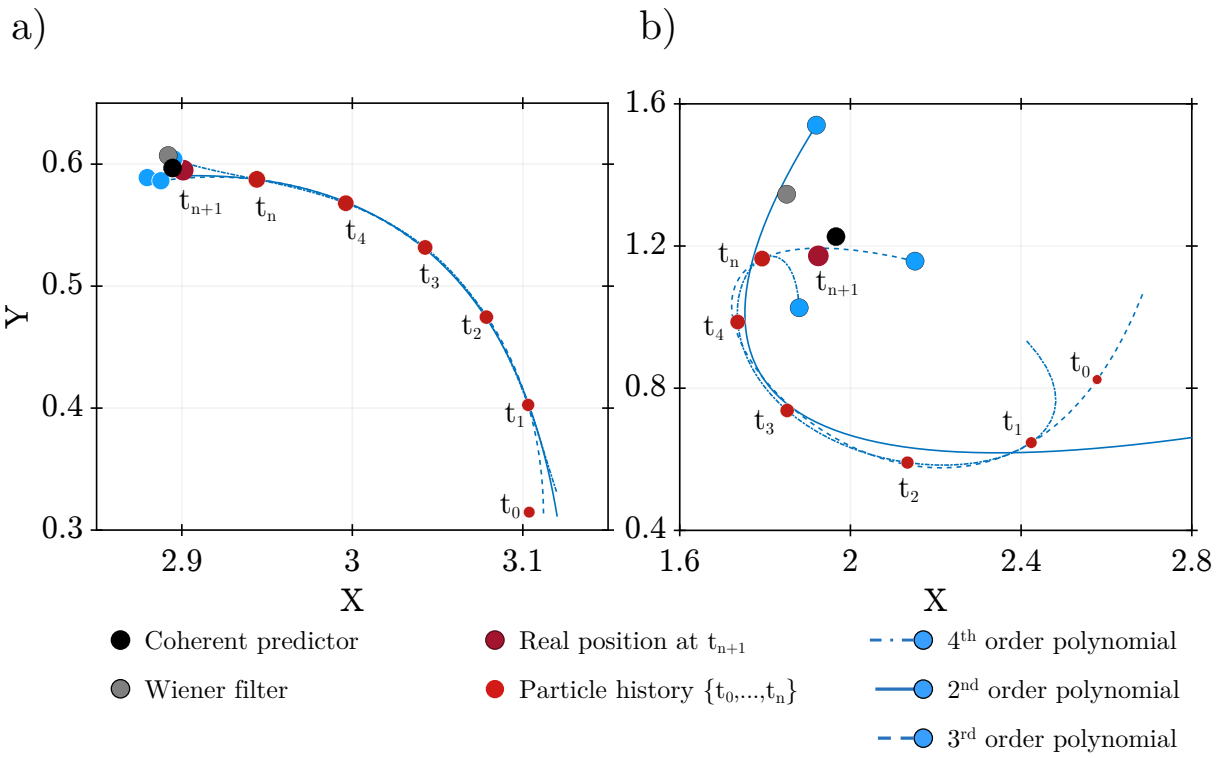

Figure 6.5 – Prediction comparison for single trajectories in 2D-HIT. (a) Smooth trajectory. (b) Highly curved trajectory.

the form of 2D-STB. We compared four open access PTV techniques with three predictor functions in 2D-STB (seven techniques in total). The first technique is named TracTrac [103]. This technique initiates with the nearest neighbour approach, then looks for the best forward/backward match from t_{n-1} to t_{n+1}. The key point in this technique is to use a predictor function based on the nearest known velocity around the untracked particles. The TracTrac code is able to reconstruct more than $10,000$ tracks per second with 0.01 pixel resolution accuracy [103]. This technique was evaluated with the PIV challenge cases [104]. Part2Track [105] is the second technique used in the current assessment. It is a 2D polynomial predictive tracking technique. It can be said that Part2Track is a simplified 2D version of STB. The code is well-organised and robust in terms of particle density. Another open access code that we employed is 2D Enhanced Track Initialisation (4BE-ETI [46]) as a representative of four frame based techniques. 4BE-ETI looks for all probabilities around the target particle, followed by creating two consecutive predictions in the following four frames. Any particle close to the predicted position is considered for the prediction of the next frame (see section 5.1). A solution is considered reconstructed if one unique

Table 6.1 – Scenarios for trajectory assessments

Case	1	2	3	4	5
Particle concentration (ppp)	0.025	0.05	0.08	0.1	0.2
Noise ratio (%)	0	15	30	45	60
Temporal scale ($\times dt_{DNS}$)	20	40	60	80	100

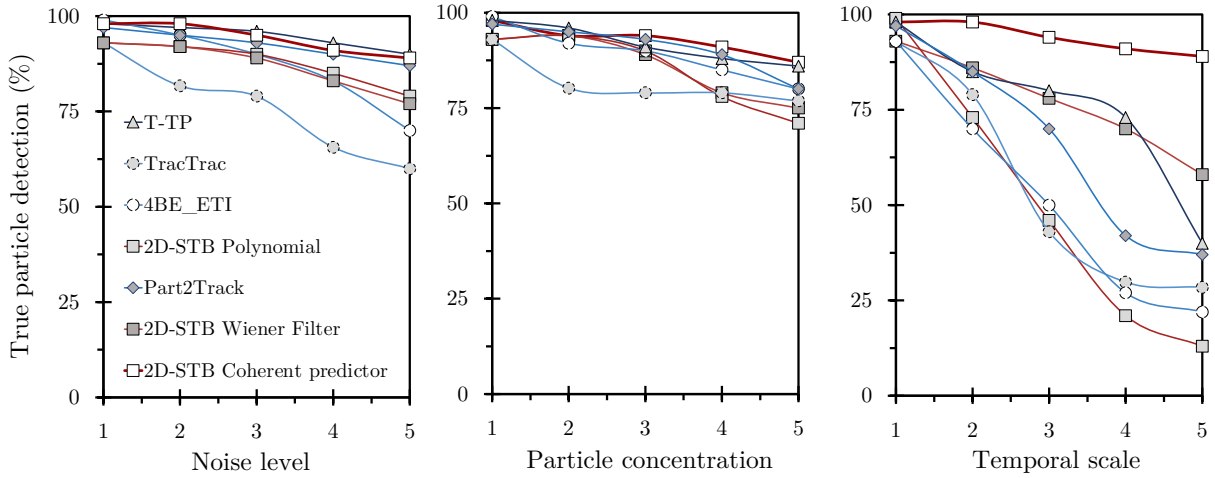

Figure 6.6 – Comparison performances of 2D tracking techniques in terms of fraction of true particle detection by changing each characteristic parameter.

track is found after four frames. Topology-based particle tracking [92] is the last PTV algorithm for the present assessment. The aforementioned technique generates particle descriptors (feature vector) of nearest neighbour particles for each frame. Thereafter, for each particle, groups of nearest neighbours are stored in the descriptor by binning these particles into a gridded bin, assuming that particles tend to remain within the same bin in the next time step. Eventually, it performs an iterative wrapping scheme to track large particle motions. This method has been evaluated for biological flow motions [92].

All the mentioned techniques were assessed based on three characteristic parameters, particle concentration, temporal scale, and noise level. In the case of having low particle density, a simple optimisation technique would lead to build true trajectories. However, more particles interact and move close to each other by increasing density, which requires a more sophisticated algorithm to detect more true tracks. Adding noise level creates a more realistic situation in synthetic image studies, since noises are inevitable in experi-

ments due to their nature. Therefore, the algorithm robustness over different noise levels would provide valuable information to determine which technique is appropriate for a particular experiment. As discussed in section 4.3, the DNS time step is smaller than the smallest timescale of turbulence, which is the order of Kolmogorov timescale. This means the transport of particles between two DNS time steps is smooth enough to reach true prediction even with linear extrapolation. However, the experiment time step is multiple times higher than the DNS time step, depending on the acquisition setup. To reach a realistic condition, five time steps starting from every 20 to 100 DNS time steps are considered. Table 6.1 shows all scenarios we designed to assess the tracking accuracy of the mentioned techniques. It is assumed that all techniques receive the same particle reconstruction accuracy. Finally, we compare the deviation of the final detected positions with the ground truth data. Algorithms track true particles if the deviation is in the same order as the reconstruction accuracy. Case 1 is the starting point for each technique. Then we increase each parameter individually within five scenarios. Figure 6.6 shows the fraction of true reconstructed tracks over the total number of particles. By increasing the noise ratio up to 60 % noisy reconstruction, Part2Track, TP-P, and Coherent predictor tend to keep their robustness. Meanwhile, other techniques faced significant drops, losing nearly half of the true particles. Among all techniques, TracTrac has the most sensitivity to the noise ratio. Figure 6.6 shows that particle concentration has almost the same impact on all techniques. By increasing the time step, less information is available, and then the prediction would be more challenging. In all mentioned techniques, relying only on a single particle as a single signal to find its true track and losing information in the middle causes more wrong tracks. However, even a weak signal of coherent particle behaviour would lead to correct direction and prediction. Results showed that when adding more spatial and temporal coherent information, the prediction function stayed robust for up to 85 % in all situations, while other techniques suffered from lack of information.

6.3 3D turbulent wake flow synthetic study

To evaluate our novel position prediction scheme in a 3D complex flow, we used a DNS simulation of the wake behind a smooth cylinder at Reynolds number equal to 3900 computed by an open-access code named `Incompact3d` [80]. As discussed in section 4.3, particles are transported by every 10 DNS time step using the fourth order Runge Kutta temporal and trilinear spatial schemes. In the synthetic case, particle trajectories are

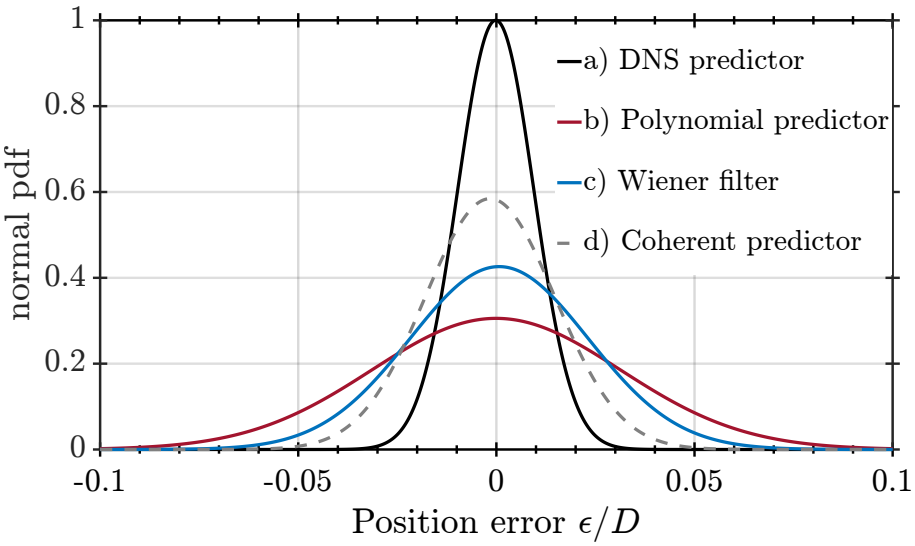

Figure 6.7 – Normal pdf of particle position estimation error before the optimisation process in x direction of four predictor functions.

smooth and predictable when the synthetic temporal scale is with the same order of the DNS time step due to the small travelling distance between two time steps (less than the Kolmogorov timescale). To mimic a real experiment, we created around $150,000$ ground truth trajectories associated with noise for every 20 DNS time step. Similar to the 2D-HIT case, by increasing the temporal scale, less temporal information is available, and then the prediction would become more challenging.

In this section, we compared the position prediction of four schemes with the ground truth particle trajectories (see table 6.2). For the first scheme, the DNS predictor was defined as a reference using the Euler equation to transport particle positions by the ground truth DNS velocity. In such a scenario, we can estimate the minimum bias error achieved in this sparse temporal scale. Both Wiener filter and polynomial predictors are also selected to be compared with the LCS based predictor (i.e., coherent predictor). The prediction error can be decomposed into two general sources, the bias error caused by flow dynamics and the system error caused by the measurement uncertainties. The bias error is the position deviation, sourced from the predictor function, with ground truth positions when there is no noisy position reconstruction. We decomposed these two terms to better understand the predictor functions in the upcoming sections.

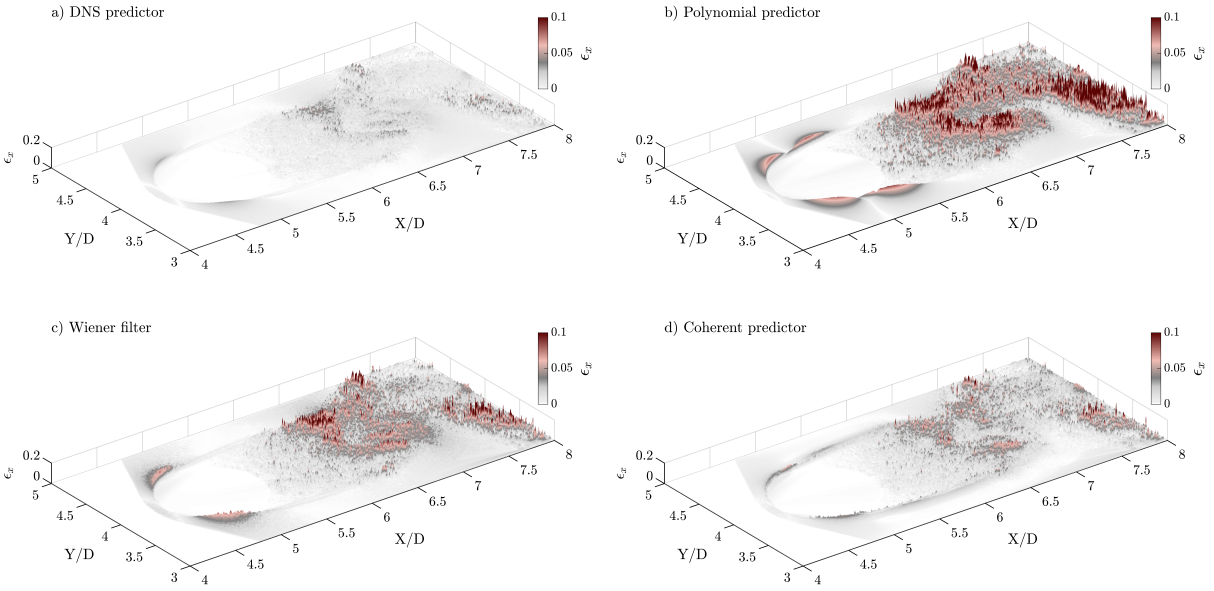

Figure 6.8 – Instantaneous position estimation error before the optimisation process averaged in z direction. (a) DNS predictor. (b) Polynomial Predictor. (c) Wiener filter. (d) Coherent predictor.

6.3.1 Bias error

The bias error is directly linked with the flow behaviour where position, velocity, and acceleration uncertainties are omitted. The bias error will increase due to the lack of accuracy in the prediction if there is an increased variation in the flow dynamics. Figure 6.7 shows normal pdf of the predicted position error in x direction of four schemes. Position error in x direction shows that the deviations of the coherent predictor stay virtually below $\epsilon/\mathrm{D} = 0.05$, where D is the cylinder diameter. On the contrary, a significant number of particles are mispredicted in both polynomial and Wiener filter techniques. Similar significant improvements by using coherent predictor are observed in y and z directions. Figure 6.8 shows the projected distribution of the bias error on xy plane for each predictor function. Interestingly, the prediction bias error is highly correlated with the flow acceleration in all schemes. Although the DNS predictor (see figure 6.8.a) uses known ground truth velocity information, the travelling distance is large enough to introduce minor errors, particularly inside the wake region. As shown in figure 6.8.b, the third order polynomial has the worst prediction error, which can be up to $\epsilon/\mathrm{D} = 0.2$ around the cylinder leading edge and inside the wake region. The polynomial prediction error distribution is thoroughly shaped by the flow motion (i.e., topology), meaning that any

Table 6.2 – Prediction function formulations.

Method	Fit parameters	Cost function	Prediction
a) DNS predictor	-	-	$y_{n+1} = \dot{X}_{DNS} \cdot t_{n+1}$
b) Polynomial predictor	$\sum_{j=0}^{\ell} a_j.t_i^j = y_i$	$\mathcal{J} = \frac{1}{n}\sum_{i=1}^{n}(X_i - y_i)^2$	$y_{n+1} = \sum_{j=0}^{\ell} a_j.t_{n+1}^j$
c) Wiener filter	$\sum_{j=1}^{\ell} w_j.u_n = y_n$	$\mathcal{J} = \sum_{i=1}^{n}(X_i - y_i)^2$	$y_{n+1} = \sum_{j=2}^{\ell+1} w_j.u_n$
d) Coherent predictor	$\sum_{j=0}^{\ell} a_j.t_i^j = y_i$	$\mathcal{J} = \frac{1}{n}\sum_{i=1}^{n}(X_i - y_i)^2$	$y_{n+1} = \sum_{j=0}^{\ell} a_j.t_{n+1}^j$
-	$\sum_{j=1}^{\ell} a_j.(j).t_n^{j-1} = \dot{y}_n^c$	$\cdots + (\dot{X}_n - \dot{y}_n^c)^2$	
-	$\sum_{j=2}^{\ell} a_j.(j).(j-1).t_n^{j-2} = \ddot{y}_n^c$	$\cdots + (\ddot{X}_n - \ddot{y}_n^c)^2$	

variations inside the flow create a huge estimation error. Overall and local performance of the Wiener filter is better than the polynomial predictor. The Wiener filter succeeded to reduce the prediction error in most of the peak regions (see figure 6.8.b.c). The error significantly increases inside the wake region, where the turbulence intensity level is relatively higher than the rest of the regions. Error distribution reveals that coherent predictor has the best performance locally and globally compared to Wiener and polynomial predictors in a 3D turbulent flow.

6.3.2 Monte Carlo uncertainty quantification (MC-UQ)

For each individual trajectory, we perform a Monte Carlo simulation to quantify the uncertainty level of the prediction function. As mentioned in section 6.1, a predictor function takes positions of the tracked particles from either the initialisation or the optimisation steps. In Monte Carlo uncertainty quantification (MC-UQ), the parameter distributions of models are sampled randomly, followed by statistics calculated on the output model. Figure 6.9 shows the probability distribution of the predicted positions as a function of distributed input uncertainties.

To start the MC-UQ simulation, we need to quantify the uncertainty level of the input parameters that are fed into the predictor function. As mentioned in section 2.1, a classic 4D-PTV process starts with IPR. The uncertainty level of IPR can be utilised as an input parameter for uncertainty quantification of the prediction function. This can be

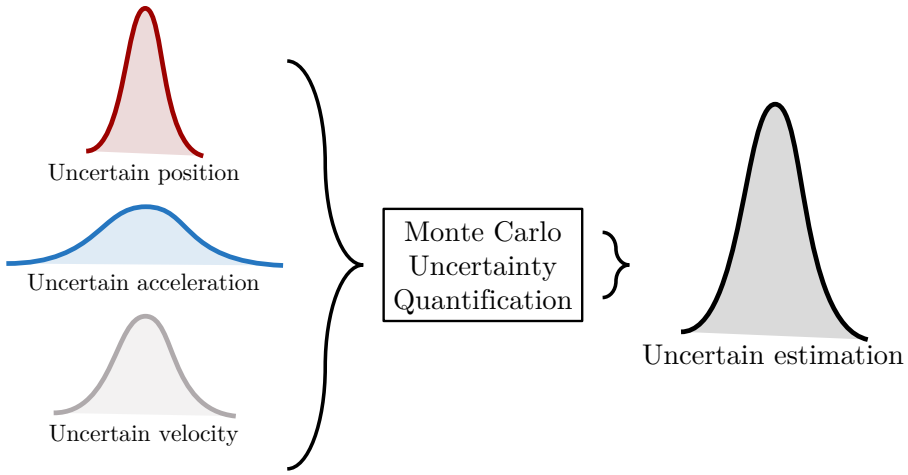

Figure 6.9 – Schematic of the Monte Carlo uncertainty quantification (MC-UQ) algorithm with distributed input parameters.

obtained from numerical or analytical IPR performance analyses reported by Wieneke [20] and Jahn et al. [33]. However, these values are optimistic and might differ in practical conditions due to the tuning issue. Instead, we averaged the estimation errors of all participants in the LPT challenge 2020 [43] to mimic practical and generic uncertainty levels that might be introduced for a predictor function. To this end, we estimated the normal probability distribution of position, velocity and acceleration input variables by using the LPT challenge reported estimation errors. As a result, we can quantify the output uncertainty level of predictor functions using MC-UQ with estimated input normal distributions.

MC-UQ process of four prediction functions, second-order polynomial, third order polynomial, Wiener filter, and coherent predictor, for nearly $10,000$ trajectories, are shown in figure 6.10. We need to subtract the bias error from the predicted position error obtained from uncertain input parameters to decompose the impact of uncertainty with the impact of flow motion behaviour. Referring to section 6.3.1, the coherent predictor showed better bias error than both Wiener filter and polynomial predictors. MC-UQ requires nearly $10,000$ iterations per trajectory to achieve a smooth Gaussian distribution in the output. As a result, the total number of 100 million $(10,000 \times 10,000)$ predictions was computed for each predictor function. The results in figure 6.10.a.b show that the uncertainty level in position estimation at t_{n+1} increases by adding order of magnitudes in the polynomial predictor from $\epsilon/D = 0.004$ to $\epsilon/D = 0.032$. This indicates an inverse correlation between the bias error and the uncertainty level in using polynomial predic-

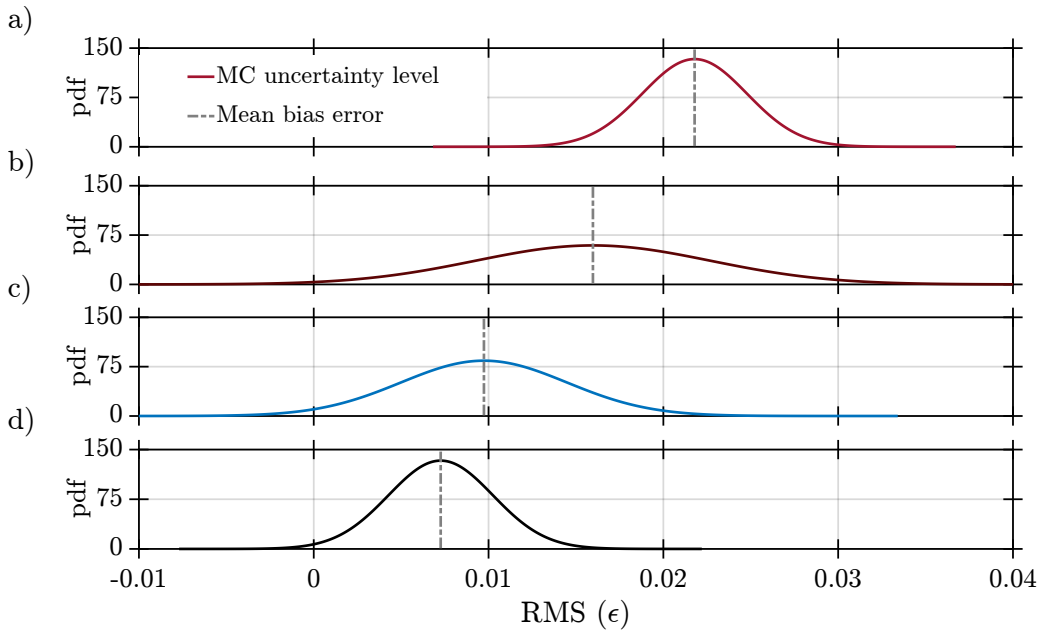

Figure 6.10 – Probability distribution around the bias error obtained from the MC-UQ of four predictor functions. (a) Second-order polynomial. (b) Third order polynomial predictor. (c) Wiener filter. (d) Coherent predictor. Blue dashed lines represent the averaged bias error over $10,1000$ Lagrangian trajectories.

tors. It was found that the third order polynomial keeps better overall accuracy and uncertainty performance compared to the second order polynomial. The uncertainty level of the coherent predictor was found to be minimum and at the same level as the second order polynomial. The Wiener filter reached a better bias error and narrow uncertainty distribution than both polynomial functions. As a result of the bias error and uncertainty level computations, the coherent predictor showed a better balance between the position bias error and output uncertainty with respect to all the mentioned predictors.

6.4 Generic cost function minimisation

In sections 6.2 and 6.3, we showed that the cost function obtained from three terms of position, velocity, and acceleration could significantly reduce the bias error and the uncertainty level caused by the flow complexities and the measurement uncertainties, respectively. Despite the mentioned improvements, an estimated position in a real experiment needs to be applicable to a wide range of experiments. To this end, we address how to formulise a generic non-dimensional form of the proposed cost function in equa-

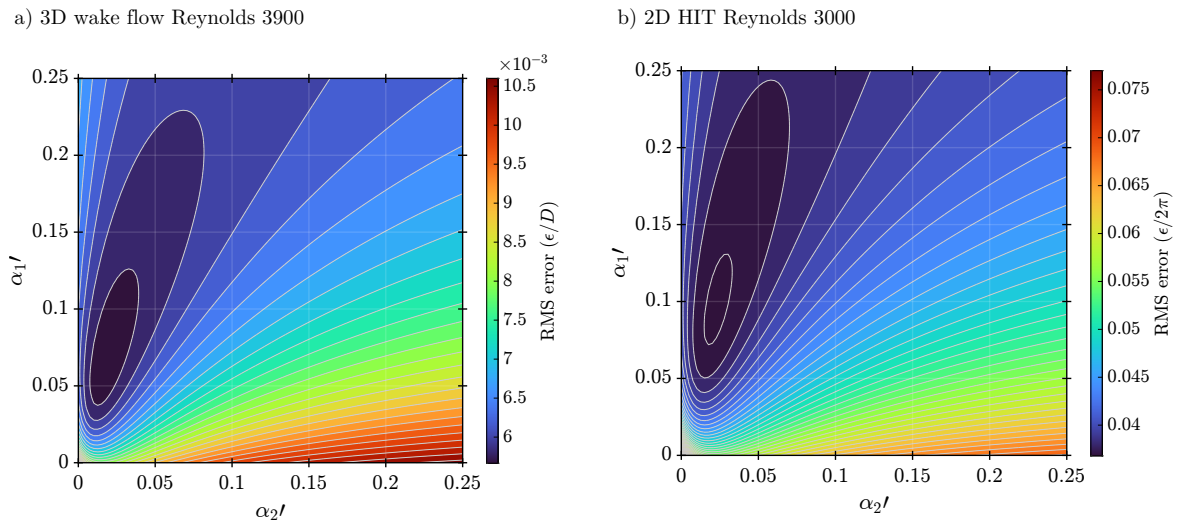

Figure 6.11 – Contour plot of the estimation error with respect to α_1' and α_2' weighting terms. The synthetic trajectories were generated based on the 1st LPT challenge estimation errors. (a) 3D wake behind a cylinder at a Reynolds number equal to 3900. (b) 2D homogeneous isotropic turbulent flow at a Reynolds number equal to 3000.

tion (6.6). To start, we define weighting parameters to the cost function to reach the minimum estimation bias error. The weighted cost function can be written as

$$\mathcal{J} = \frac{1}{n}\sum_{i=1}^{n}(X_i - y_i)^2 + \alpha_1(\dot{X}_n - \dot{y}_n)^2 + \alpha_2(\ddot{X}_n - \ddot{y}_n)^2, \tag{6.8}$$

where X_i are the estimated positions based on known y_i observations in time. α_1 and α_2 are dimensional velocity and acceleration weights, respectively. Similar to equation (6.6), the generic cost function contains three terms. The first is the least mean square minimisation problem of the polynomial predictor based on the history of particles. The second and the third terms are neighbouring coherent velocity and accelerations. In Chapter 5, we showed that coherent velocity and acceleration terms could be computed by using LCS metric [106]. Equal weights of α_1 and α_2 mean that the impact of the neighbouring variations is at the same level as the history of the target particle. However, the particle history should be the most significant signal in the estimation process. So weighting would help to determine each term's impact. Additionally, the derived cost function in equation (6.6) has different dimensional terms (position, velocity, and acceleration). To achieve a generic form, these terms require being non-dimensionalised based on turbulent

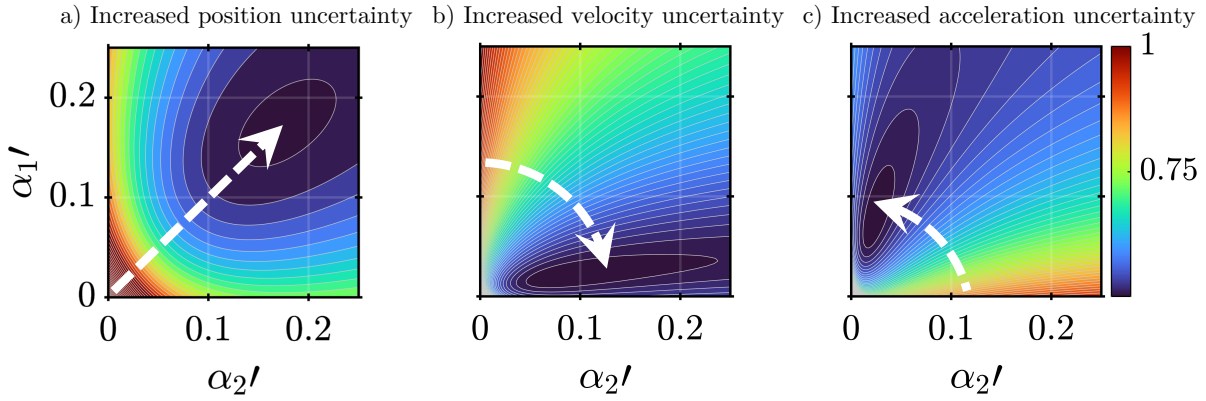

Figure 6.12 – Contour plot of the estimation error as a function of observations uncertainty levels. White arrows show the changing direction of optimal solutions (i.e., minimum estimation error) by increasing each observation uncertainty.

integral scales as

$$\begin{aligned} x' = \frac{x}{D} \ , \ y' = \frac{y}{D} \\ \dot{x}' = \frac{\dot{x}}{U} \ , \ \dot{y}' = \frac{\dot{y}}{U} \\ \ddot{x}' = \ddot{x}\ \frac{D}{U^2} \ , \ \ddot{y}' = \ddot{y}\ \frac{D}{U^2}, \end{aligned} \tag{6.9}$$

where D is an integral length scale, and U is the velocity reference. Therefore, the modified cost function will become

$$\mathcal{J} = D^2\ (\frac{1}{n}\sum_{i=1}^{n}(X_i' - y_i')^2) + \alpha_1 U^2\ (\dot{X}_n' - \dot{y}_n')^2 + \alpha_2 \frac{U^4}{D^2}\ (\ddot{X}_n' - \ddot{y}_n')^2, \tag{6.10}$$

which can be simplified as

$$\mathcal{J}' = \underbrace{\frac{1}{n}\sum_{i=1}^{n}(X_i' - y_i')^2}_{\text{position history}} + \underbrace{\alpha_1'\ (\dot{X}_n' - \dot{y}_n')^2}_{\text{coherent velocity}} + \underbrace{\alpha_2'\ (\ddot{X}_n' - \ddot{y}_n')^2}_{\text{coherent acceleration}}, \tag{6.11}$$

where

$$\alpha_1' = \alpha_1(\frac{U}{D})^2 \ , \ \alpha_2' = \alpha_2(\frac{U}{D})^4 \ , \text{ and } \mathcal{J}' = \frac{\mathcal{J}}{D^2}. \tag{6.12}$$

Two non-dimensional α_1' and α_2' weights determine how much velocity and acceleration signals can constrain the overall cost function minimisation process. In equation (6.11), weight of the target position history is directly linked with two α_1' and α_2' values. If both

terms are set for any range below one, the history will have the most significant impact on the prediction function. We need to minimise the derived cost function for finding the optimal solution for the predictor function. The minimisation process of $\mathcal{J}'$ starts by solving $\frac{\partial \mathcal{J}'}{\partial a} = 0$. Mathematics of the cost function minimisation is addressed in Appendix B. The derived minimised cost function of equation (6.11) is

$$\left(\frac{1}{n} \sum_{i=1}^{n} \begin{bmatrix} t_i^6 & t_i^5 & t_i^4 & t_i^3 \\ t_i^5 & t_i^4 & t_i^3 & t_i^2 \\ t_i^4 & t_i^3 & t_i^2 & t_i \\ t_i^3 & t_i^2 & t_i & 1 \end{bmatrix} + \alpha_1{\prime} \begin{bmatrix} 9t_n^4 & 6t_n^3 & 3t_n^2 & 0 \\ 6t_n^3 & 4t_n^2 & 2t_n & 0 \\ 3t_n^2 & 2t_n & 1 & 0 \\ 0 & 0 & 0 & 0 \end{bmatrix} + \alpha_2{\prime} \begin{bmatrix} 36t_n^2 & 12t_n & 0 & 0 \\ 12t_n & 4 & 0 & 0 \\ 0 & 0 & 0 & 0 \\ 0 & 0 & 0 & 0 \end{bmatrix} \right) \begin{bmatrix} a_3 \\ a_2 \\ a_1 \\ a_0 \end{bmatrix}$$
$$= \left(\frac{1}{n} \sum_{i=1}^{n} \begin{bmatrix} y_i t_i^3 \\ y_i t_i^2 \\ y_i t_i \\ y_i \end{bmatrix} + \alpha_1{\prime} \begin{bmatrix} 3\dot{y}_n t_n^2 \\ 2\dot{y}_n t_n \\ \dot{y}_n \\ 0 \end{bmatrix} + \alpha_2{\prime} \begin{bmatrix} 6\ddot{y}_n t_n \\ 2\ddot{y}_n \\ 0 \\ 0 \end{bmatrix} \right), \tag{6.13}$$

where t_i are the input time steps, and a_i are the solution coefficients. The optimal solution of the minimised cost function leads to the minimum estimation error of the predictor function. Now, we have the minimised cost function of equation (6.11), and the question is how to set two α' weights optimally. To this end, we need to perform prediction for a range of α' weights and determine the optimal solution. Since a real experiment is associated with uncertainties and inaccuracies, it is crucial to have an appropriate uncertainty estimation of each observation in the cost function, i.e., the positions y'_i, the coherent velocity $\dot{y}'_n$, and the coherent acceleration $\ddot{y}'_n$. To this end, we employed data reported by the 1st LPT challenge [5] as a reference starting point to estimate inaccuracies that might be introduced into a predictor function. The 1st LPT challenge assessed position estimation accuracy of six time-resolved tracking algorithms, including the coherency based tracking [6] for particle densities from 0.05 to 0.2 ppp. In this section, the non-dimensionalised position ϵ_X/D, velocity $\epsilon_{\dot{X}}/U_\infty$, and acceleration $\epsilon_{\ddot{X}} D/{U_\infty}^2$ errors were employed to create the synthetic data at each particle density. As a result of the LPT challenge, the averaged RMS position error was 0.005 mm where the integral scale was $D = 10$ mm at the density of 0.12 ppp, which gives $\epsilon_X/D = 5.10^{-4}$. The averaged velocity and acceleration errors at the same density were found to be $\epsilon_{\dot{X}}/U_\infty = 0.01$ and $\epsilon_{\ddot{X}} {U_\infty}^2/D = 0.3$, respectively. This shows that the acceleration estimation has at least

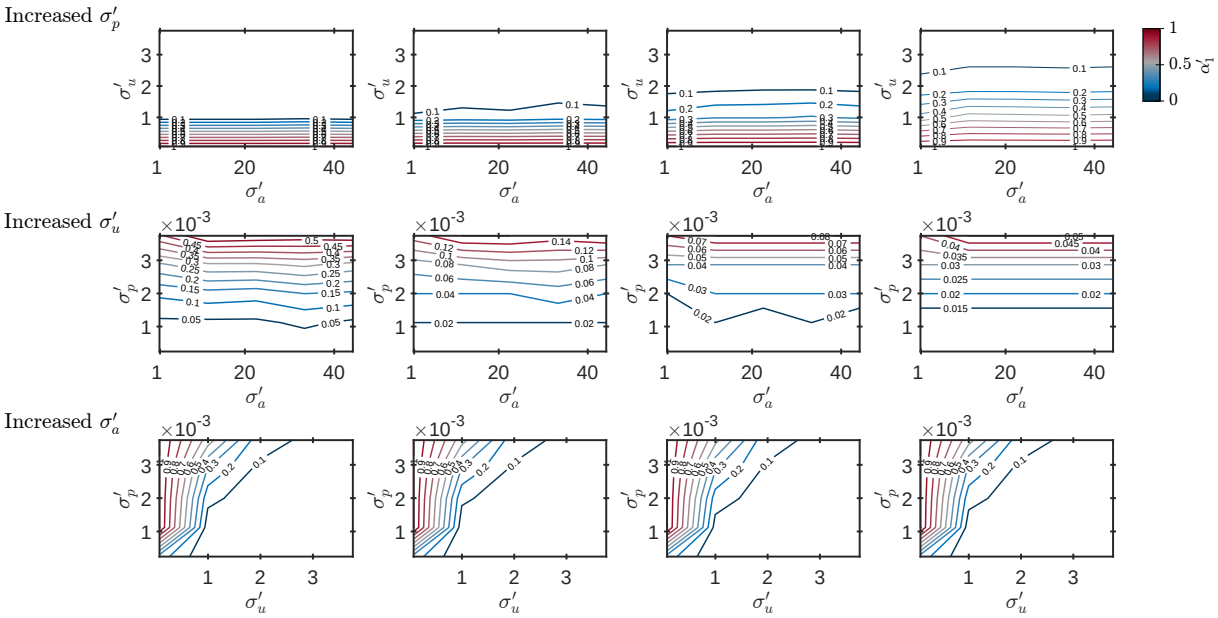

Figure 6.13 – Contour plot of the optimal value for α'_1 as a function of measurement uncertainties.

an order of magnitude higher estimation error than other terms. We introduced these errors as input uncertainties into the Lagrangian trajectories of 2D-HIT and 3D cylinder wake flow and then computed the correlation of the final estimation error and α' weights. For such a scenario, we can expect the optimal solution should have less α'_2 weight than α'_1 because of having more acceleration estimation error than other terms. Therefore, we plot the prediction RMS error in a range of α' weights to find the optimal solution in figure 6.11. Since the acceleration error is higher than other terms in both synthetic data, the minimum error happens with relatively lower α'_2 values (i.e., $\alpha'_1/\alpha'_2 >> 1$). Both weighting parameters are found to be significantly smaller than $<< 1$. This means that the history of the target particle with unit weight is the most valuable signal in such a scenario. Comparing the error behaviour in 2D-HIT and 3D cylinder wake flow cases shows that both cases need similar weighting parameters and require $\alpha'_1/\alpha'_2 >> 1$ with small weighting magnitudes $\alpha' << 1$.

The result of the minimised cost function from two synthetic test cases suggests that the optimal solution can be directly linked with input observations uncertainty levels. Therefore, we designed three further parametric test cases to determine the mentioned statement. As shown in figure 6.12, we increased the uncertainty level of each parameter solely while other terms are fixed to assess how the optimal solution behaves concerning

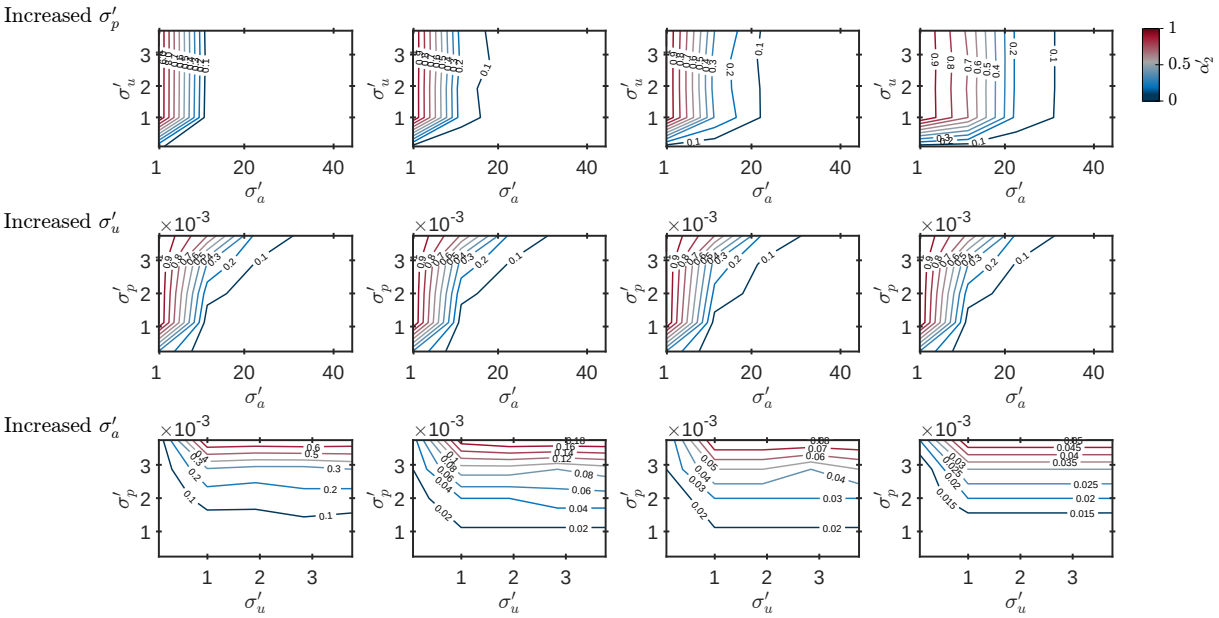

Figure 6.14 – Contour plot of the optimal value for α'_2 as a function of measurement uncertainties.

three position, velocity, and acceleration uncertainties. The optimal solution tends to linearly move away toward higher weighting magnitude with increased position uncertainty (see figure 6.12.a). If we fix the position uncertainty, the optimal solution rotates with the same distance around the coordinate centre, depending on which parameter is increased (see figure 6.12.b.c). As a result of this assessment, an appropriate estimation of three uncertainty levels would provide enough information to set weighting parameters. We can model the correlation between two weighting terms. Generally, magnitudes of both gains increase by increased position uncertainty, and the slope for α_2/α_1 is a function of relative velocity and acceleration uncertainties. The subsequent step is to quantitatively model the cost function weights as a function of input uncertainties. Assuming the optimal values of α' weights are written as

$$\begin{aligned} \alpha'_1 &= f(\sigma'_p, \sigma'_u, \sigma'_a) \\ \alpha'_2 &= g(\sigma'_p, \sigma'_u, \sigma'_a), \end{aligned} \tag{6.14}$$

where $\sigma'_p, \sigma'_u, \sigma'_a$ are non-dimensional position, velocity, and acceleration uncertainties. The non-dimensionalisation was performed with the same approach in equation (6.9) as $\sigma'_p = \sigma_p/D$, $\sigma'_u = \sigma_u/U_\infty$ and $\sigma'_a = \sigma_a\ D/U_\infty^2$. Then we can fit a numerical model over the range of α' weights by changing all three uncertainty levels. $10 \times 10 \times 10$ scenarios were

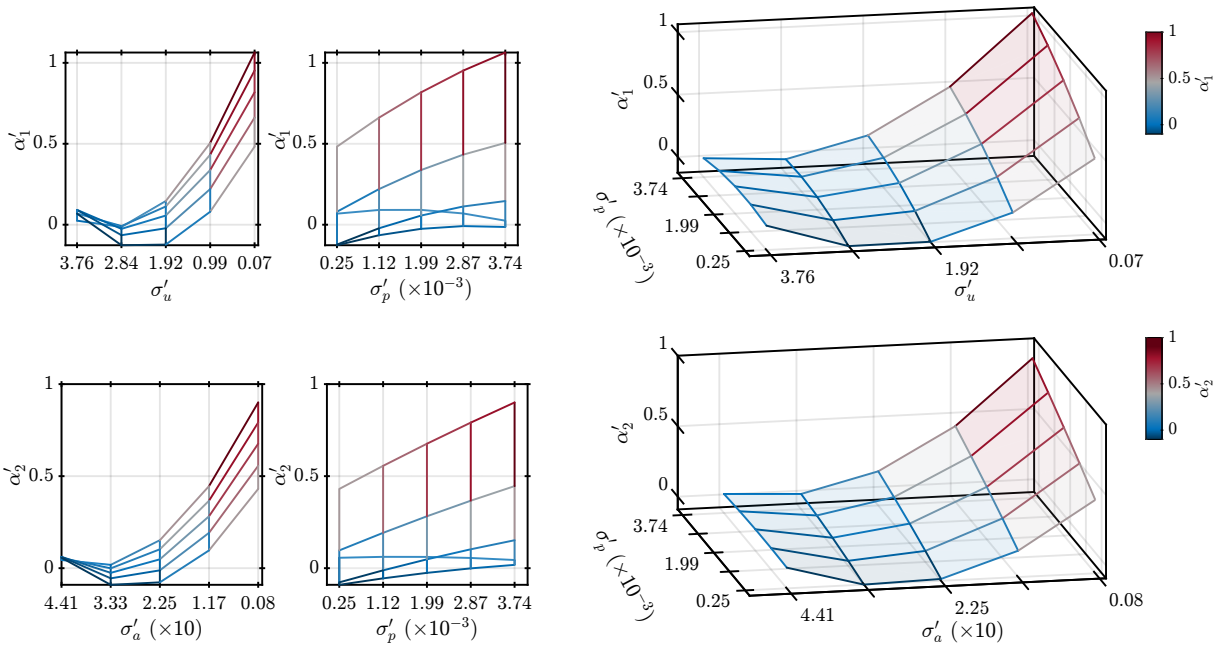

Figure 6.15 – The optimal α'_1 and α'_2 weighting terms to reach the minimum prediction error as a function of uncertainty levels fitted by quadratic surfaces.

performed to record the optimal weights of each scenario. The contour plots of figure 6.13 and figure 6.14 show that the optimal values for α'_1 and α'_2 raise by increased position uncertainty, which is in agreement with the estimated model in figure 6.12. We need to set smaller α'_1 gain if the velocity estimation is uncertain. However, α'_1 stays almost constant as acceleration uncertainty increases. With a similar behaviour, we need more α'_2 gain by increased position uncertainty. And the acceleration uncertainty has a reverse relation with α'_2 while the velocity uncertainty has almost no impact on the optimal value for α'_2. Independencies of α'_1 to the acceleration uncertainty and α'_2 to the velocity uncertainty, suggest that the models in equation (6.14) can become a 2D problem as

$$\begin{aligned} \alpha'_1 &= f(\sigma'_p, \sigma'_u) \\ \alpha'_2 &= g(\sigma'_p, \sigma'_a). \end{aligned} \tag{6.15}$$

On the other hand, we can model the optimal solution by roughly estimating position, velocity, and acceleration uncertainties by fitting quadratic surfaces over the minimum α'_{12} values. The generic model of each weight is illustrated in figure 6.15. The model suggests that $\alpha'_1 \propto {\sigma'_u}^2$ and $\alpha'_2 \propto {\sigma'_a}^2$. In addition, both weights have roughly linear relation to the position uncertainty $\alpha'_{12} \propto \sigma'_p$. As a result, we can estimate the optimal solution of the

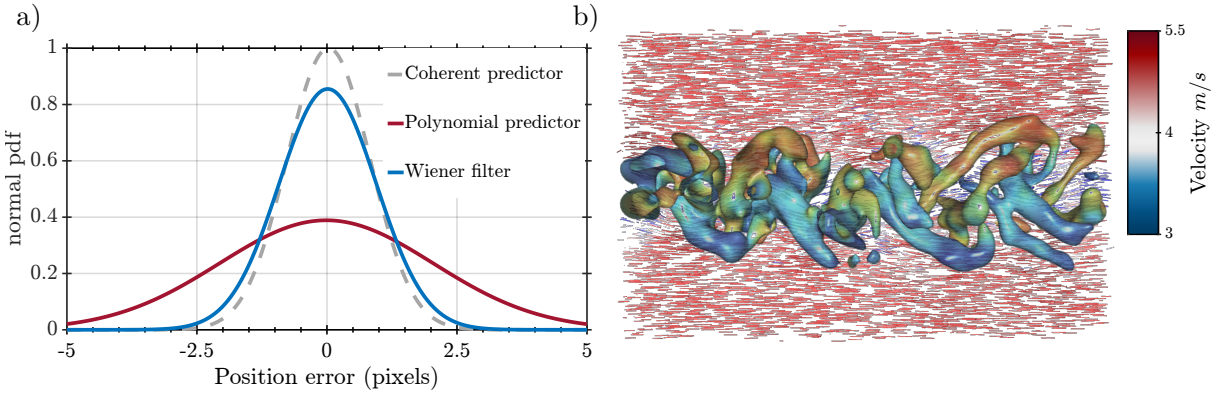

Figure 6.16 – The cylinder wake flow at Reynolds 3900. (a) Experiment normal pdf results of particle position error in x direction of three predictors. Each predictor is compared with final optimised positions of STB Davis. (b) Side view of particle trajectories superimposed by vorticity iso-surfaces.

cost function by knowing uncertainty levels.

6.5 Experimental evaluation

To quantify the results of different schemes, we compared predictions with optimised positions obtained from STB Davis. As a result of the experiment, STB successfully built nearly 12000 particles. Trajectory results of the current experiment with superimposed vorticity iso-surfaces are shown in figure 6.16.b. Noisy particle reconstruction of four time steps was used as an input of the prediction functions. We compared three techniques, polynomial, Wiener filter, and coherent predictors, with final optimised positions. The deviation of position estimated of each technique is shown in figure 6.16.a. The distribution shows that the coherent predictor has more accurate estimations within 1 pixel deviation from the optimised positions. Position estimations of Wiener filter and coherent predictors stay below 2.5 pixels deviation for nearly all particles. On the contrary, the polynomial predictor has maximum deviation with STB Davis. Statistic analyses of the current wake flow experiment for nearly 4000 time steps are discussed in Chapter 7.

6.6 Conclusions

We proposed a robust technique to predict particle positions based on their local temporal and spatial coherent motions. LCS can classify and divide the coherent neighbour motions. We imposed first and second-order derivatives of the neighbour coherent motions into the predictor function in addition to the particle history. To assess the proposed method named coherent predictor, we performed the synthetic analysis of the 2D-HIT flow at Reynolds number equal to 3000 and the wake behind a smooth cylinder at Reynolds number equal to 3900. We compared three predictor functions. Polynomial predictor showed maximum deviation with the ground truth data, whereas coherent predictor provided the most accurate position estimation. We found that the flow regions highly impact the estimation error. Inside the wake region, particularly the vortex formation zone and the two sideward shear layers, cause more challenges in prediction. These mentioned regions are featured by high acceleration and 3D directional motions. We also performed the 4D-PTV experiment of the wake flow behind a cylinder at the same Reynolds number. It was found that the coherent predictor is reliable to estimate particle positions very close to the optimised positions.

Chapter 7

4D-PTV to Study Lagrangian Statistics

Recent advances in tracking highly concentrated tracer particles over long trajectories extend the possibility of exploring the Lagrangian viewpoint of turbulent properties. The recent work of Viggiano et al. [107] showed how we could obtain fundamental Lagrangian turbulence quantities, particularly the Lagrangian structure function scaling constant C_0, from anisotropic and inhomogeneous dynamics of a jet flow by normalising the trajectories based on local Eulerian scales. The C_0 constant in the Lagrangian framework is in a similar role as the Kolmogorov constant in the Eulerian framework [107]. In the present study, we are interested in examining the stationarisation process proposed by Viggiano et al. [107] in the wake behind a smooth cylinder and studying Lagrangian statistics from Lagrangian trajectories.

7.1 Lagrangian diffusion properties

We performed Lagrangian statistical analysis on nearly 12000 trajectories for 4000 time steps. Taylor's turbulent diffusion theory [108] has been used widely to study homogeneous isotropic turbulent (HIT) flows. In a given time τ, Taylor's theory computes the Lagrangian two-point correlation function $R^L_{uu}(\tau)$ for an ensemble of particle trajectories based on the mean square displacements of particles $\sigma^2(\tau)$ that can be written as

$$\frac{\mathrm{d}^2\sigma^2}{\mathrm{d}\tau^2}(\tau) = 2R^L_{uu}(\tau). \tag{7.1}$$

The turbulent diffusion process to Lagrangian statistical properties of particle trajectories can be linked if we assume that particles in the present study act as a tracer [107]. This means that all the inertial effects are neglected, and particles perfectly follow the flow motion. Therefore, we can compute the Lagrangian second order structure-function

as

$$S_2^L(\tau) = \langle [u(t+\tau) - u(t)]^2 \rangle = 2\left(R_{uu}^L(0) - R_{uu}^L(\tau)\right), \tag{7.2}$$

where the Lagrangian trajectories were obtained from three-dimensional particle tracking velocimetry (4D-PTV). Therefore, we can compute the Lagrangian universal constant C_0 for the Lagrangian second order structure function. This constant was found to be strongly sensitive to the Reynolds number, large-scale anisotropy and inhomogeneity of flow [107]. This means that computation of the C_0 constant is complicated in anisotropic and inhomogeneous turbulent cases. In the wake behind a cylinder, turbulent length and time scales evolve as flow goes downstream, creating non-stationary anisotropic and inhomogeneous dynamics. Batchelor's diffusion theory [109] as an extension of Taylor's theory, proposed using the Lagrangian stationarisation idea for inhomogeneous cases such as the wake flow. Stationarisation is a process based on Eulerian self-similarity properties that stationarises the Lagrangian dynamics.

7.2 Lagrangian structure function scaling constant

Recently, Viggiano et al. [107] investigated the highly anisotropic and inhomogeneous case in a free shear turbulent jet. Viggiano et al. [107] characterised the inertial-range dynamics and the Lagrangian universal constant C_0 by the Lagrangian stationarisation idea. Two Lagrangian second order structure function and two-point correlation function statistics needs to be computed. The Lagrangian second order structure function can be written as

$$S_2^L(\tau) = \left\langle [u_i(t+\tau) - u_i(t)]^2 \right\rangle = C_0 \frac{\varepsilon_i \tau}{\sigma_{u_i}^2}, \tag{7.3}$$

where ε is the turbulent cost dissipation. To stationarise the Lagrangian in-stationarity of the wake flow, as proposed by [107], we compute the Eulerian mean velocity by fine-scale reconstruction (VIC# [110]) from Lagrangian trajectories. Then the deviation between the instantaneous and the mean components non-dimensionalised by the Reynolds stress terms is as follows

$$\tilde{u}_i(\tau) = \frac{u_i(\tau) - \bar{u}_i(x(\tau))}{\sigma_{u_i}(x(\tau))}. \tag{7.4}$$

We can achieve a stationarised flow field with non-dimensionalised fluctuations through the entire spatial domain for every time step. With the same derivation spirit discussed

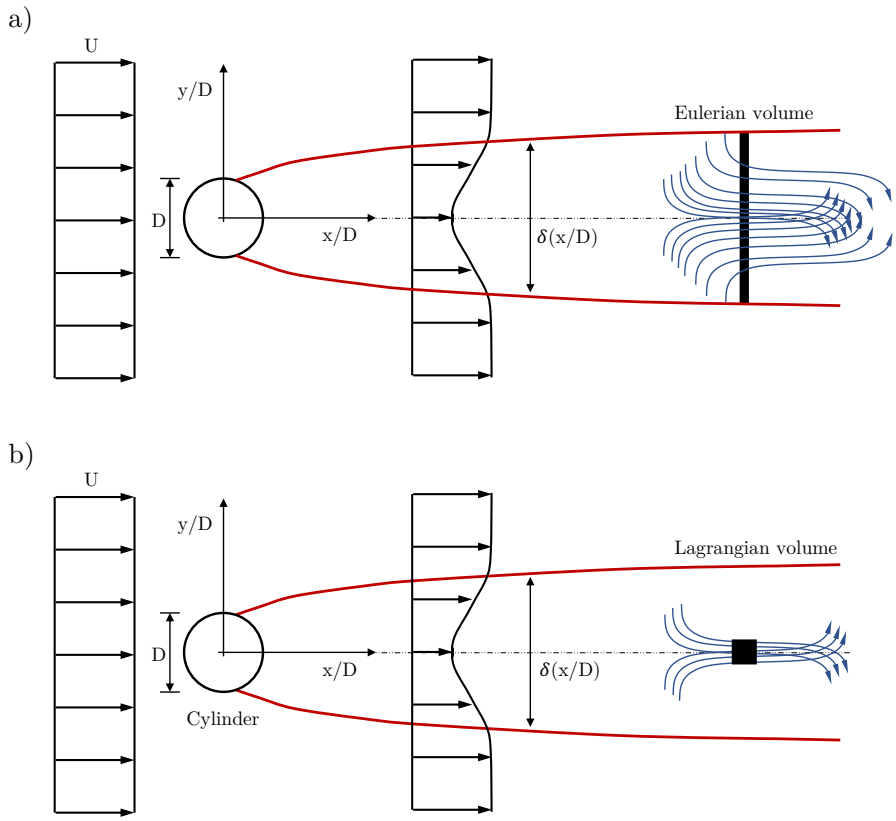

Figure 7.1 – Computation of the wake flow statistics from Lagrangian trajectories. (a) Eulerian statistics at a certain downstream x/D over all trajectories passing the Eulerian volume. (b) Lagrangian statistics at a certain downstream x/D over all trajectories passing the Lagrangian volume.

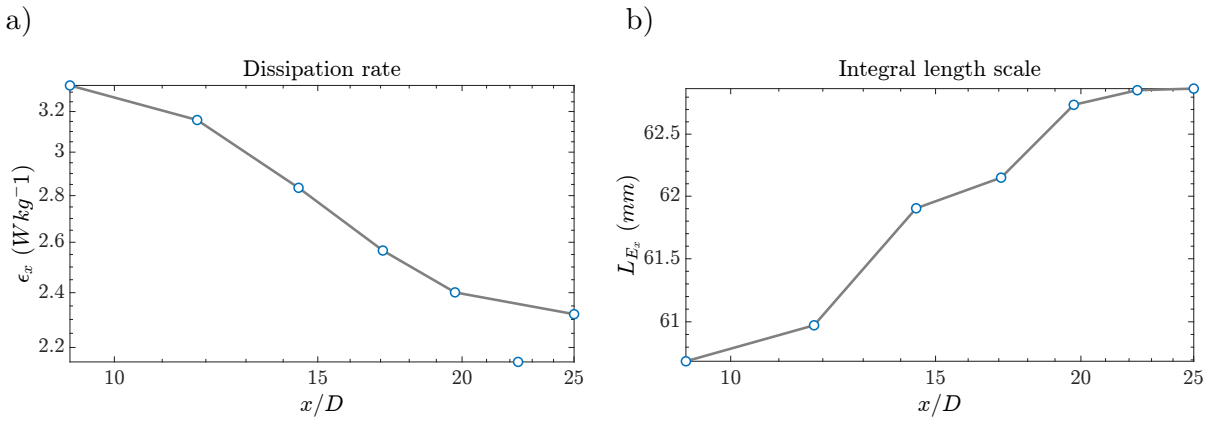

Figure 7.2 – Computation of Eulerian statistics. (a) Decay of the dissipation rate ε_x. (b) Evolution of the integral length scale L_{E_x}.

in [107], [111], we are interested in exploring Lagrangian properties for the wake behind a cylinder.

7.3 Wake flow statistics

The velocity component of each trajectory was computed after fitting a curve over noisy reconstructed positions. The Eulerian fields were computed using fine-scale reconstruction (VIC# [110]) between trajectories to achieve gridded velocity fields. Thereafter, time-averaged mean $\bar{u}_i(x(\tau))$ and Reynolds stress $\sigma_{u_i}(x(\tau))$ terms can be computed by averaging all instantaneous Eulerian velocity fields to start the process in equation (7.4). Schematic of the wake flow self similar behaviour downstream of the cylinder is shown in figure 7.1. Due to the loss of momentum cases by the cylinder, the wake velocities are smaller than the free stream region. The wake thickness increases as the flow travels downstream of the cylinder. We can compute the Eulerian statistics within the area of the wake. Ensemble of all trajectories passing a virtual volume inside the wake at a certain x/D is considered to achieve statistically converged Eulerian properties as shown in figure 7.1. The Eulerian volume has the dimension of $\delta(x/D) \times 2D$ in y and z directions with 0.5mm depth in x direction as suggested by Viggiano et al. [107]. Therefore, we can compute the Eulerian second order structure function over the ensemble of spatial velocity increments of each pair trajectories passing the Eulerian volume. Velocity components were stationarised with equation (7.4). We computed the Eulerian turbulent properties in seven downstream positions varying from $x/D = 9$ to 25 as listed in table 7.1. Nearly constant values of the Taylor microscale Re_λ shows that the stationarisation process suggested by Batchelor [109] is valid for the self similar wake flow far downstream of the wake flow. Decay of the dissipation rate ε_{u_x} toward downstream is also in with power-law decay in self-similar flows. Both Kolmogorov η_x, and integral L_{E_x} length scales are growing as flow goes far downstream.

The evolution of Eulerian dissipation rate ε_{u_x}, Kolmogorov length scale η_x, and integral scale T_{E_x} will be used to compute Lagrangian statistical properties. To compute the Lagrangian second order statistics, we assume a small cube volume inside the wake with the length of $\delta(x/D)/3$ (suggested by Viggiano et al. [107]) and index all trajectories passing the volume. Following equation (7.3), we compute temporal velocity increments on each individual trajectory. The ensemble of computed temporal increments is then averaged to compute the Lagrangian second order structure function. By solving the left

Table 7.1 – Eulerian parameters for various x/D positions.

x/D	σ_{u_x} (m s^{-1})	ε_z $\left(\text{ W kg}^{-1}\right)$	η_z (μm)	τ_{η_z} (ms)	λ_z (μm)	Re$_\lambda$	L_{E_z} (mm)	T_{E_z} (ms)
9	0.31	3.33	17.65	2.1	255.2	53.97	60.7	19.39
11	0.30	3.15	17.90	2.2	255.3	52.54	61	20.02
14	0.29	2.83	18.38	2.3	258.8	51.15	61.9	21.16
17	0.28	2.56	18.85	2.4	267.1	51.81	62.1	21.65
19	0.27	2.40	19.16	2.5	267.8	50.40	62.7	22.52
22	0.26	2.15	19.70	2.6	273.6	49.78	62.9	23.34
25	0.26	2.31	19.33	2.5	266.9	49.21	62.9	23.04

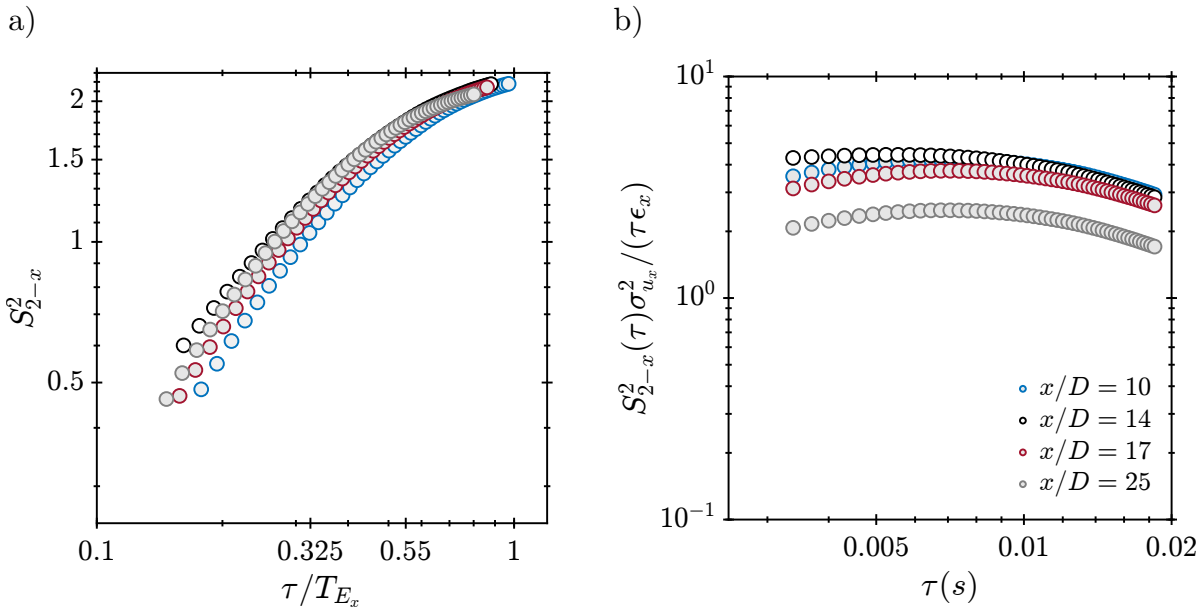

Figure 7.3 – Lagrangian second order structure function of the streamwise direction at four downstream locations. (a) Non-dimensional $S^L_{2,x}$ as a function of non-dimensional timescale. (b) Re-dimensionalised structure function representing the C_0 constant.

side of equation (7.3), we can compute the C_0 constant where ε_i and $\sigma^2_{u_i}$ are the Eulerian dissipation rate and the averaged velocity standard deviation over the Lagrangian volume.

The Lagrangian second order structure function at four downstream locations is plotted in figure 7.2. The result of non-dimensional $S^2_{2,x}$ in far downstream shows that the Lagrangian statistics becomes independent of the downstream position ($x/D > 10$). In the present study, we were unable to reach converged statistics for $x/D < 10$. We also observe that the non-dimensional $S^2_{2,x}$ has linear relation with τ where $\eta_x < \tau < T_{E_x}$. These findings are in agreement with the free jet self-similar case [107].

7.4 Conclusions

Lagrangian statistics of the wake flow experiment showed that the Lagrangian statistics becomes independent of the downstream position in far downstream $x/D > 10$ (see figure 7.3). These findings are in agreement with the free jet self-similar case ([107]). Figure 7.3.b suggests the C_0 value, which should stay nearly constant in the inertial range. C_0 is found to be between $2 - 4$ for the selected downstream locations. Based on the modelling suggested by Sawford [112], C_0 should be around 2.6 for the corresponding Taylor microscale Reynolds number. Therefore, the estimated C_0 of the present study is in the same order as Sawford's model.

Chapter 8

Application of Lagrangian Coherency in PIV

In this chapter, we study the possibility of improving the estimation accuracy of classic PIV experiments using Lagrangian coherent motions. We present a novel approach to adjust shapes of the interrogation windows (IW) in 2-PIV measurements as a function of temporal and spatial local coherent motions. LCS has been widely utilised to determine local flow boundaries. We propose using FTLE to quantify LCS separatrix boundaries (i.e., ridges) and adjust the interrogation window. We integrated the proposed method with a local optical flow PIV algorithm. The evaluation was performed using synthetic particle images of 2D homogeneous isotropic turbulence obtained from Direct Numerical Simulation (DNS). The results showed significant improvements in regions with complex flow behaviours, particularly shear, vortex and hyperbolic motions. We studied improvements of the velocity estimation in a real experiment of the wake flow behind a cylinder at Reynolds number equal to 3900. It was found that optical flow featured by coherency based interrogation window (coherent optical flow) reveals detailed vector field estimations in regions with complex behaviours inside the wake flow.

In 2D-PIV algorithms, both correlation-based and local optical flow techniques rely on the interrogation windows. The importance of interrogation window has been studied widely for obtaining effective methods of adapting the window size and shape, which directly impacts the spatial accuracy of velocity estimation [113], [114]. Since the flow behaviour inside the interrogation window has clusters of small and large scale coherent motions, PIV techniques involve window size reduction to avoid those non-coherent areas and increase the maximum achievable spatial resolution. Generally, the interrogation window size is gradually reduced based on empirical precalculations and tunings, while this empirical approach can be adjusted by temporal and local spatial information. This means flow behaviour in different times and spaces would result in different interrogation window shapes, which is the main objective of this chapter. To demonstrate the performance of

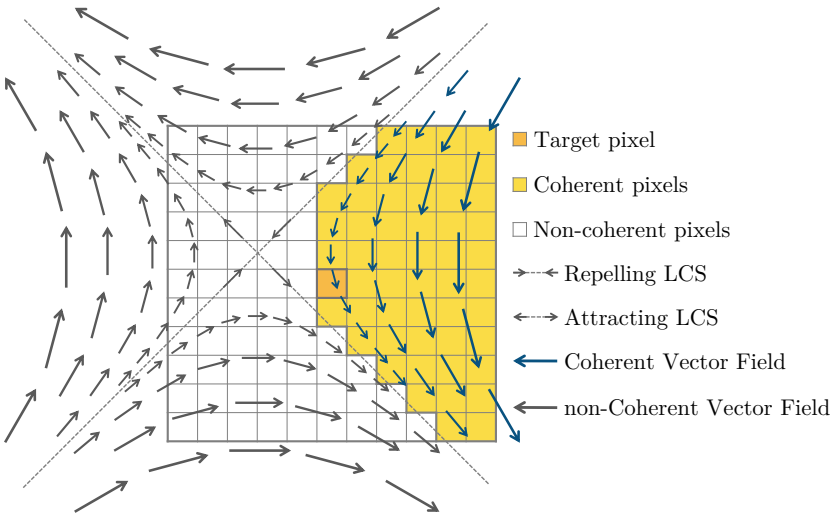

Figure 8.1 – Schematic of Window adjusting based on Lagrangian coherency to calculate velocity for a centre pixel (dark grey pixel), attracting and repelling separatrix lines, grey pixels are coherent with the centre pixel and coherent pixels.

the proposed method, we integrated the adjustable interrogation window with the local optical flow PIV algorithm. In the local optical flow approach, all pixels inside the window are considered for calculating a single-pixel velocity at the centre of the window. However, to estimate more accurate motions, it is crucial to ignore areas that are non-coherent with the centre pixel. This study seeks to adjust the interrogation window shape in motion estimation by calculating locally coherent and non-coherent areas. We propose performing LCS by looking for the local separatrix ridges that divide the flow field into clusters of coherent regions [3]. The idea of applying LCS in PIV/PTV algorithms was demonstrated by Khojasteh et al. [6]. To this end, all neighbour pixels inside the interrogation window must be classified as coherent or non-coherent with the centre pixel. Similar interrogation window adjustment can be implemented in cross correlation-based PIV techniques.

8.1 Local optical flow

Classic optical flow works under the intensity consistency assumption of the acquired images that is inspired by Horn and Schunck [115] formulation. It can also be written in terms of the Optical Flow Constraint equation (OFCE) as follows,

$$\frac{df}{dt} = \frac{\partial f}{\partial t} + v.\nabla f, \tag{8.1}$$

where v is the desired velocity of one time step and f is the image intensity. The operator Δ denotes gradient over 2D area. On the other hand, we minimise the energy function with the intensity consistency assumption. However, real PIV images are featured with temporal changes of intensity between consecutive images due to illumination and trigger setup. So this assumption can be violated in PIV applications. Schuster et al. [116] improved the intensity inconsistency problem by introducing stochastic optical flow formulation. The Eulerian flow velocity field is decomposed into a large-scale smooth component and a small-scale turbulent component in the stochastic approach. In the present study, we use the same stochastic approach implemented into the Lucas-Kanade optical flow estimator [116]. In theory, optical flow provides one velocity vector for each pixel of two consecutive images based on spatial and temporal variations of the image intensities. While cross correlation based PIV techniques result in coarse resolution estimation. Therefore, optical flow PIV techniques might provide more details of the flow behaviour in turbulent flows.

8.2 Coherent interrogation window

Lagrangian Coherent Structures (LCS) divide the local flow field into regions of coherent motions [3]. LCS is also known as the skeleton of flow that can be utilised as a deterministic criterion to shape the interrogation window. We computed the LCS separatrix ridges using Finite-Time Lyapunov Exponent (FTLE) by employing modified versions of two open-access codes named LCS kit [117] and LCS tool [118]. FTLE is a scalar value that measures the amount of spatial stretching over a finite time. In this study, the spatial region is determined by the interrogation window to compute the FTLE value locally. Khojasteh et al. [6] showed that using FTLE in the local spatial regions over sparse neighbour particles can reveal signs of local ridges that can be employed in the velocimetry algorithms. FTLE analysis provides spatial and temporal flow field behaviour. We propose to adjust the interrogation window based on separatrix ridges, resulting in different window shapes in space and time. The window shape will not change if the area is entirely coherent. On the other hand, the shape of the interrogation window does not change if all pixels are coherent with the target pixel. The major problem happens when the interrogation window consists of multi-scale dynamics. Figure 8.1 is a classic

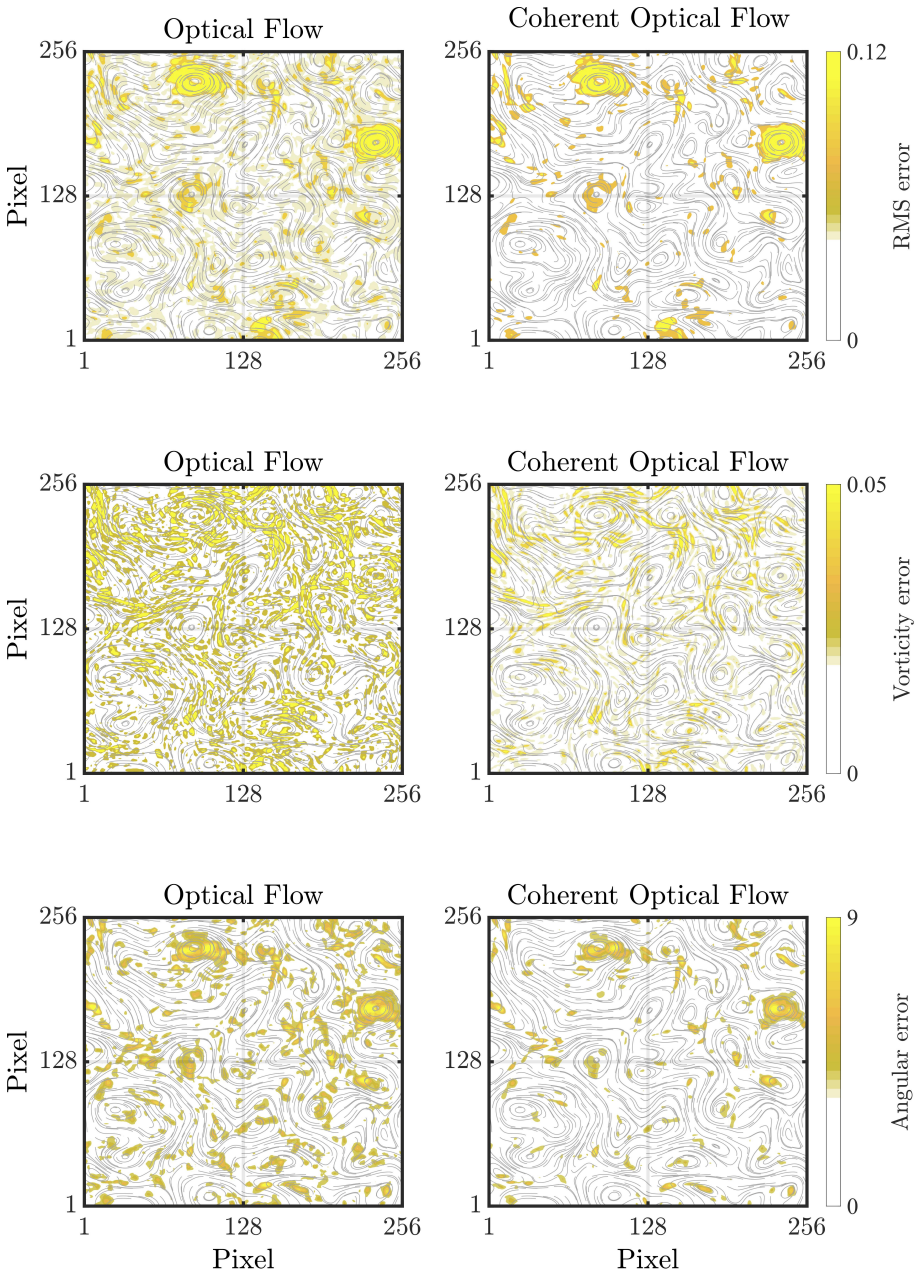

Figure 8.2 – Angular error comparison between local optical flow with and without coherent adjustable window in global view. Only high values of angular error are shown.

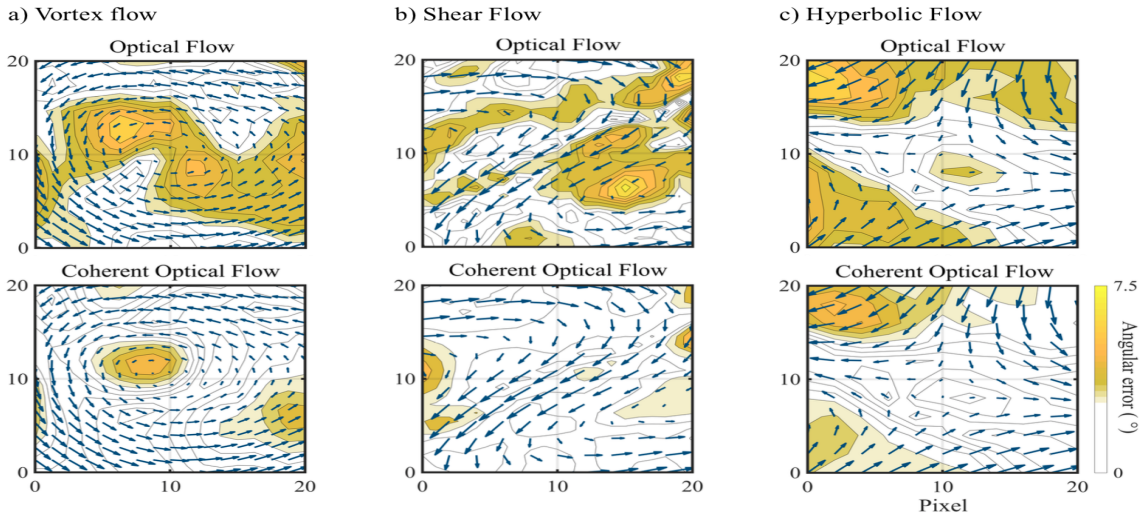

Figure 8.3 – Angular error local comparison between local optical flow with and without coherent adjustable window in three scenarios locally selected from 2D isotropic homogeneous turbulence. (a) vortex flow. (b) shear flow. (c) hyperbolic flow. Only high values of angular error are shown.

example of hyperbolic flow when two or more vortices interact with each other in 2D turbulent flows. Forward and backward FTLE calculations determine two attracting and repelling lines, where flow particles do not cross these lines. Flow motions in between these boundaries have coherent motions. Depending on the centre location, coherent flow motions (in the blue vector field) and regions (in yellow pixels) are on one side of these lines (see figure 8.1). Any pixel inside the coherent region is considered for the spatial and temporal gradient of intensity computation. We need to have prior knowledge about the velocity field to compute the FTLE map. The minimisation process in the optical flow is an iterative approach. We found that it is unnecessary to compute the whole iterative process with additional LCS computations since it is costly in time. Therefore, we introduce the LCS computation in the last three iterations of the minimisation process. In this way, we provide near to the final solution vector field for the first Lagrangian separatrices computation.

8.3 Results and evaluation

8.3.1 Synthetic evaluation

We performed synthetic analyses to examine the performance of the proposed technique. The synthetic PIV images were generated from Direct Numerical Simulation (DNS) of a 2D homogeneous isotropic turbulent flow. The boundary condition of each side of the domain was set at periodic. The DNS resolution was 256×256 mesh cells. We created the synthetic particle trajectories using linear Euler transport function in time and linear velocity interpolation in space. More details of the DNS simulation can be found in [119]. We assessed improvements of using coherent interrogation window in velocity estimation results of local optical flow technique. As a result, three terms, including RMS (representing the magnitude of velocity estimation), vorticity, and angular errors, were defined to quantify the local and overall performances of the proposed technique. In an overall view, as shown in figure 8.2, we gained around 5 % global increase in velocity estimation accuracy compared with the classic local optical flow. However, it should be noted that the main objective here was to increase the resolution and accuracy around separation and non-coherent areas. Without using adjustable windows, cross-correlation and optical flow techniques would result in up to 50 % false estimation at those separation and non-coherent areas. In detail view, Figure 8.3 shows improvements in three specific flow behaviours, vortex, shear and hyperbolic flows selected locally from 2D synthetic data. These three regions are intentionally picked to illustrate differences in detailed motions. We found that local optical flow with square IW suffers from inaccurate angular estimation compared with the DNS reference in the core vortex regions when the interrogation scale is larger than the vortex scale. Disagreement hits over 7 degrees of angular vector field misestimation, with over 50 % angular error. Figure 8.3 and figure 8.4 show significant local improvements in such a region if an adjustment is performed. Similar motion refinements were also observed when high shear or hyperbolic behaviour occurred. We found that coherent optical flow has better velocity estimation in complex local regions. These local improvements impact the overall assessment of the technique in a global view.

8.3.2 Experiment case study

We performed a 2D2C PIV experiment of the wake behind a cylinder in the wind tunnel to study the capability of the proposed technique on real experiment images. The

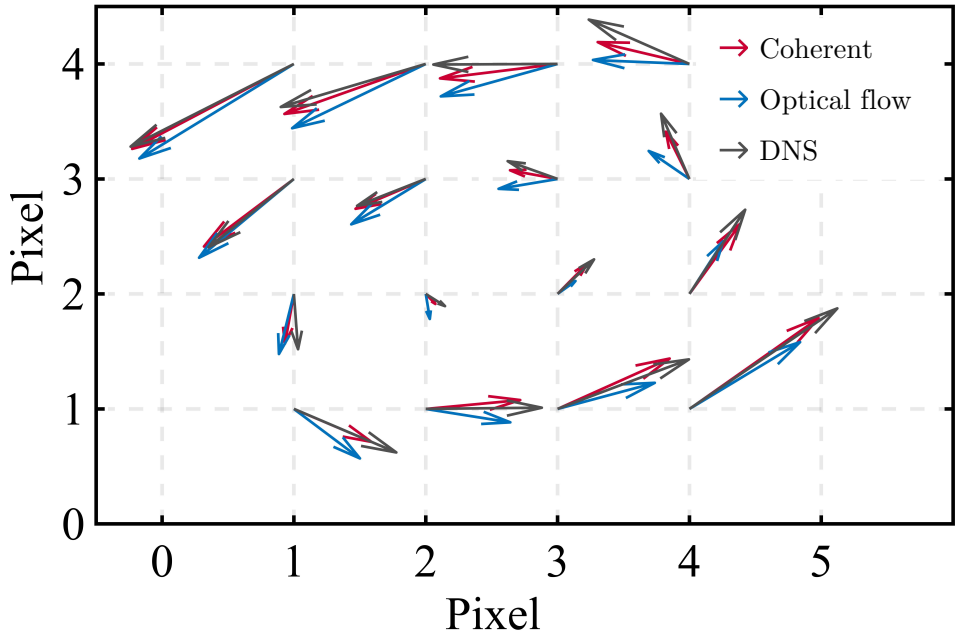

Figure 8.4 – Vector estimation of a vortex i 2D-HIT.

Reynolds number corresponding to the cylinder with 12 mm diameter was set at 3900. An sCMOS camera with 2560 × 2160 pixels was employed to acquire images in 49.2 Hz frequency. The measurement plane was illuminated using a 200 mJ laser (EverGreen from Quantel). The disparity of the velocity estimation between optical flow with and without adjustable interrogation window of the current experiment is shown in figure 8.5. As mentioned in Section 8.2, the window shape stays unchanged if the flow motion is coherent inside the interrogation window. This means that disparity should be almost zero in the majority of freestream regions. In agreement with the synthetic analysis, coherent adjustable window only refined velocity estimations of complex motions such as shear, wake, and mixing regions (see figure 8.5).

We, therefore, compared our proposed technique with the cross-correlation results obtained from Davis software (10.1.2 version). A snapshot of the instantaneous vorticity and vector fields are shown in figure 8.6 that illustrates the existence of complex mixing and vortex generations downstream of the cylinder. The vorticity field shows signs of strong shears in two sidewards of the wake immediately downstream of the cylinder ($x/D < 4$).

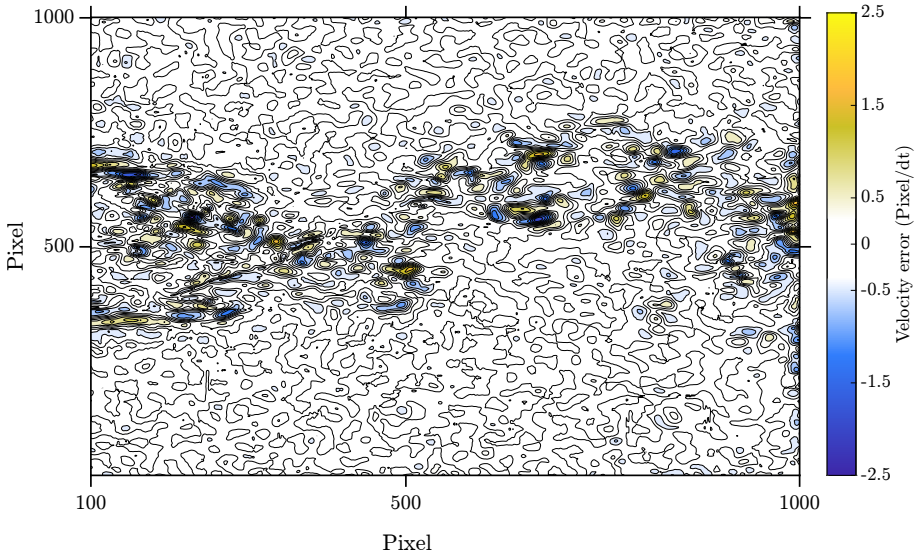

Figure 8.5 – Deviation of velocity estimation using local optical flow with and without adjustable interrogation window for the cylinder wake flow at 3900 Reynolds number.

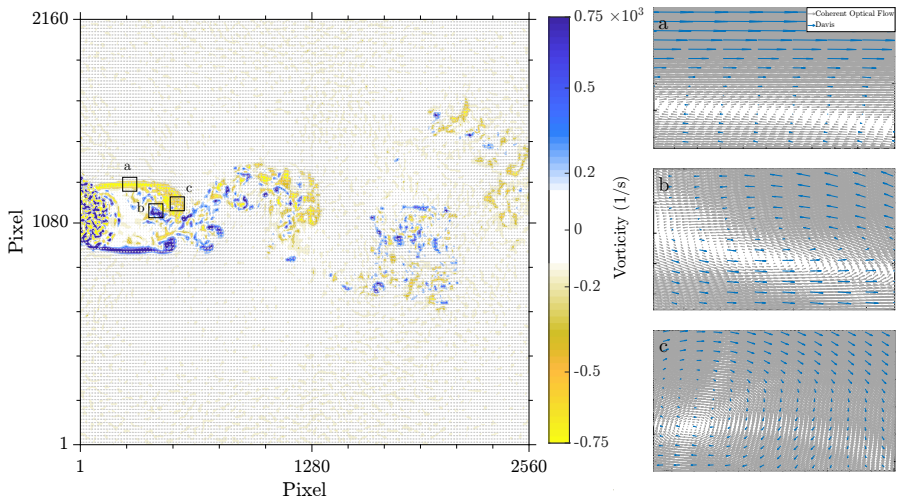

Figure 8.6 – Instantaneous snapshot of vorticity and vector fields obtained from the PIV experiment at a Reynolds number equal to 3900. (a) Local view of the vector field estimation comparison between coherent optical flow and Davis cross correlation in high shear region. (b) Comparison of vector estimation inside the wake region. (c) Comparison of vortex estimation.

These regions are featured by high velocity and acceleration gradients. We compared the cross-correlation results with coherent optical flow, knowing that the synthetic analysis showed significant misestimation in such regions (see figure 8.6.a). A 2D sliding average filter was used for both techniques for the image pretreatment. The cross-correlation final spatial resolution was 16 pixels with multi-pass vector calculations starting from 64×64 down to 16×16 and 75% overlap. As mentioned in Section 8.1, the resolved resolution of coherent optical flow is the same as the camera resolution. Therefore, the comparison was performed between high resolution coherent optical flow and coarse resolution cross-correlation results. The vector field estimations of coherent optical flow and cross-correlation PIV techniques captured shear with high gradient vector change. In contrast, coherent optical flow estimated detailed vector change in normal to shear direction with smooth change of vectors representing more physics of the flow behaviour. Figure 8.6.b shows complex vortex and mixing inside the wake region. We found that the centre of the vortex is not aligned in two techniques. There is roughly 3 pixels shift between two estimations. Coherent optical flow maintained smooth rotation with a stretch in diagonal directions. Moreover, the vector field is decreasing gradually toward the vortex centre. However, the cross-correlation technique only captured the large scale motion with a weak signature of stretching in the diagonal direction. The third local comparison is in the formation region with a strong vortex (see figure 8.6.c). Similarly, we observed disagreement in the vortex centre estimation between the two techniques while the large scale motions are almost equal. The vortex's upper right corner is near the large velocity motions (see figure 8.6.c). By contrast, the vortex centre is located inside the wake, with drastically lower velocity values. Such a gradient associated with the flow rotation creates a complex local region for PIV estimation. Comparison of two techniques shows that using a coherent adjustable interrogation window resolves more flow field details than the classic cross-correlation techniques.

8.4 Conclusion

A novel approach is proposed to adjust the PIV interrogation windows based on local spatial and temporal coherent motions. We quantify the coherent and non-content regions using Lagrangian Coherent Structures (LCS) as skeletons of flow. The synthetic analysis showed that coherent optical flow locally improves the velocity estimation accuracy up to 50%. The main advantage of the proposed technique was the improvement in angular

estimation in regions with high velocity and acceleration gradients. We also demonstrated our coherent optical flow performance in a real PIV experiment of the wake behind a cylinder at Reynolds number equal to 3900. The experiment case study revealed well-resolved velocity estimations in complex motions such as high shear, wake, and mixing regions.

Chapter 9

Conclusions and Outlook

In this thesis, we have studied how the temporal and spatial coherency of the Lagrangian particles can improve the efficiency of tracking algorithms. We constrained the algorithm to follow the physics-based information from coherent motions since Lagrangian tracer particles locally move and behave coherently with their neighbours. We used the concept of Lagrangian Coherent Structures (LCS) over sparse Lagrangian trajectories to determine local coherent motions of turbulent flows. LCS has line/surface ridges (boundaries) in 2D/3D flows that separate flow regions with dynamically different trajectories. Therefore, we can quantify coherent and non-coherent neighbour trajectories depending on LCS ridges. In this thesis, the idea of using local coherent motions of Lagrangian particles has been discussed in three velocimetry algorithms. We showed how coherent motions could increase the robustness of the track initialisation techniques. Then, the idea was employed to improve the prediction performance. The application of the proposed approach in classic PIV algorithms was also discussed.

9.1 Conclusions

In Chapter 5, we proposed a novel four (or multi) frame initialisation technique by leveraging the temporal and local spatial coherency of neighbour tracks. Our proposed technique is called "Lagrangian Coherent Track Initialisation (LCTI)". Knowing that Lagrangian trajectories do not cross these ridges, the idea is to constrain the possible solution for a single particle based on coherent motions bounded by LCS ridges. It was found that the 4D-PTV process fails if the number of true initialised tracks is not sufficient, particularly in complex flow dynamics. We showed that multi-frame initialisation techniques lose their efficiencies if flow characteristics, temporal scale, particle concentration, and noise ratio increase. Three test cases, cylinder wake flow, jet impingement, and wall bounded wake flow, were employed to qualitatively and quantitatively assess the performance of the proposed method. In the synthetic study of the wake behind a

cylinder, LCTI showed robust and accurate behaviour in detecting more true tracks with less untracked and wrong tracks. The proposed initialisation technique was also examined in a jet impingement 4D-PTV experiment. Such a case contains numerous complex flow structures from the moment particles leave the nozzle until they bounce from the solid wall. Only reconstructed positions were used as an input for this experiment assessment. LCTI (without further prediction and optimisation) was capable of reconstructing trajectories. Complex jet impingement flow structures such as vortex ring around the jet and secondary vortices were observed from the LCTI reconstruction. We concluded this chapter by noting that the LCS factor can help the tracking algorithm follow coherent structures even in high gradient and complex 3D dynamics.

In Chapter 6, we argued that the recent predictor functions in 4D-PTV suffer from a lack of information to predict the particle positions in regions with high motion gradients. The problem is that these functions solely rely on particle history as the only signal to estimate the particle position in the next time step. Following the spirit of using coherent motions, a new prediction function has been introduced, namely coherent predictor. To this end, we first designed a cost function based on three terms dealing with history, coherent velocity, and coherent acceleration. As a result of the synthetic study, the proposed cost function outperformed the recent predictor functions with lower bias error, particularly in complex regions. To quantify the uncertainty level of the proposed function, we performed Monte Carlo simulations. Coherent predictor showed narrow output uncertainty distribution compared to Wiener filter and third order polynomial predictors. The performance of the mentioned predictor functions was examined in a cylinder wake flow 4D-PTV experiment. The predicted positions from coherent predictor showed minimum deviation with the optimised positions, compared with other predictor functions. As a result of both synthetic and experimental studies, it can be said that the prediction process becomes more accurate with less uncertainty by adding velocity and acceleration coherent values.

It is interesting to extend the proposed cost function in Chapter 6 to a generic prediction form. Therefore, we introduced a non-dimensional cost function with weighted terms. The position, velocity, and acceleration terms were non-dimensionalised based on turbulent integral scales. In this way, it is possible to minimise a generic cost function applicable in various turbulent flows. We found that the measurement uncertainty directly impacts the optimal solution for the minimised predictor cost function. We employed two synthetic turbulent cases, 2D homogeneous isotropic turbulent (HIT) and the wake

behind a cylinder, with the same measurement uncertainty levels. The optimal solution of the cost function for both cases showed similar weighting configurations. This suggests that the weighting parameters can be modelled as a function of measurement uncertainties. We, therefore, performed further parametric studies and quantified a model that receives the measurement uncertainties to design the optimal cost function.

4D-PTV algorithms are ultimately designed to explore the physics of coherent structures, statistics, and fundamental turbulent characteristics in the Lagrangian framework. Interestingly, recent advances in Lagrangian experiments opened new possibilities to investigate fundamental turbulent relations in real experiments. Therefore, we performed a Lagrangian statistical analysis of the wake flow experiment in Chapter 7. We stationarised the anisotropic Lagrangian trajectories based on mean flow and local standard deviation of the velocity. The objective was to obtain turbulent characteristics and compare them with self-similar wake flow properties. Computed decay in the Eulerian dissipation rate towards downstream satisfies wake flow expectations from fundamental free shear studies. We observed increases in the Eulerian turbulent length scale, which agrees well, knowing that the wake size constantly increases. The second-order Lagrangian structure-function showed good agreement with fundamental relations far downstream of the wake. We computed the Lagrangian universal constant C_0 for the inertial-range dynamics. This constant in the Lagrangian framework plays a similar role as the Kolmogorov constant in the Eulerian framework. We provided and validated statistical Eulerian/Lagrangian turbulent characteristics of the wake flow obtained experimentally from 4D-PTV.

Chapter 8 discussed the possibility of adjusting the interrogation window based on local coherent motions. LCS ridges, also known as the skeleton of flow, divide the local flow field into regions of coherent motions. We shaped the interrogation window only to compute vector fields based on coherent motions. We locally and globally examined the proposed method with synthetic 2D-HIT and the cylinder wake flow 2D PIV experiment cases. The local synthetic assessment revealed that the adjustable interrogation window improves velocity RMS, angular, and vorticity errors in classic cases like flows in vortex, shear, and saddle point. The maximum improvement was in the angular error estimation, which requires an accurate interrogation window. Global results also showed improvements compared with the classic squared interrogation windows. The proposed technique was investigated in a 2D PIV experiment. We observed improvements, particularly in regions with small scale vortices. As a consequence of this chapter, we can suggest that adjusting the interrogation window based on local coherent motions leads to a better

vector field estimation.

9.2 Outlook

These findings provide numerous insights for future research. One suggestion is to quantify Lagrangian coherent length and time scales. It is possible to understand the physics of coherent motions by such quantification. The coherent timescale can be defined as a metric to quantify how long a group of particles stays coherent. Similarly, a coherent length scale can determine the length scale of the current local coherency. In the wake flow case, as an example, the length scale of coherent trajectories outside the wake is almost the same size as the turbulent integral scale. However, we have very small coherent length scales inside the wake. Another possible area of future research would be to investigate the introduced LCTI idea (see Chapter 5) as a PTV technique without dependency on prediction and optimisation steps. It can be interesting to define a global minimisation approach in LCTI applicable to most turbulent experiments. In addition, local segmentation of Lagrangian trajectories is an intriguing topic that could be usefully explored in future research. For example, PTV techniques can shift from single particle schemes to tracking groups of particles. Ideally, this would allow exploring coherent structures and large scale motions by tracking groups of particles. Besides the mentioned insights, a greater experimental focus is needed on Lagrangian statistics of self similar flows to establish a better fundamental understanding of physics.

As noted in Chapter 4, PIV/PTV community requires synthetic Lagrangian trajectories. To compute the transport of synthetic particles, 3D interpolations from gridded Eulerian velocity fields to particles are inevitable. It might be interesting to apply the proposed coherency based approach to only interpolate coherent elements, and achieve more accurate Lagrangian velocity estimations. In a reversed process from Lagrangian to Eulerian grids, the coherent motion idea can also be implemented in techniques such as Lagrangian PIV (LaPIV [39]) and functional binning [120] by having adjustable interpolation volumes. The adjustable interrogation window proposed in Chapter 8 needs to be investigated statistically instead of instantaneous comparisons to precisely determine its performance.

APPENDIX A, LAGRANGIAN/EULERIAN DATASET OF THE WAKE FLOW

The current dataset contains Eulerian velocity and pressure fields, and Lagrangian particle trajectories of the wake downstream of a smooth cylinder at a Reynolds number equal to 3900. The open-access Direct Numerical Simulation (DNS) code Incompact3d was used to calculate the Eulerian field around the cylinder. Trajectories of roughly 200,000 particles for two sub-domains are available. This dataset can be used as a test case for tracking algorithm assessment, exploring the physics of Lagrangian particles, statistic analyses, data assimilation and machine learning interests.

```
count=0; %counter for reading the vector file
%nx mesh size in x direction
%ny mesh size in y direction
%nz mesh size in z direction

for k=1:nz
    for j=1:ny
        for i=1:nx

            count=count+1;

            U(i,j,k)= U (count,1);
            U(i,j,k)= V (count,1);
            U(i,j,k)= W (count,1);

        end
    end
end
```

Reading snapshots

Three main categories are available in the data repository, Sub-domain-1, Sub-domain-2, and Software. The snapshots are formatted in text (.txt) and collected in compressed files (.zip). There is no particular requirement for reading and opening the data. The naming format of each snapshot is shown in figure 9.1. The Eulerian 3D snapshots are saved in vector formats. Therefore, it is necessary to extract them within three internal loops in xyz directions. The users also need to download the grid file separately to find the corresponding coordinates. The users also need to download xyz-grids separately to find the corresponding coordinates for every component. Here is an example of reading the snapshots,

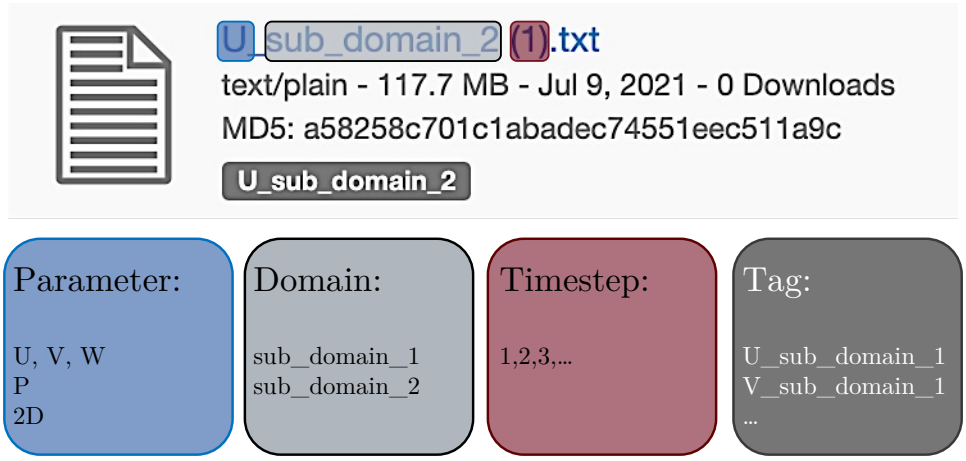

Figure 9.1 – The naming format of each snapshot in the data repository.

Finding snapshots in the repository

This file contains instructions to appropriately use the dataset. The snapshots are formatted in text (.txt) files, so there should be no requirement for reading the data. Users need to read the 3D snapshots within three internal loops because they are saved in a vector format. You can find the naming format in figure 9.1. Three 2D3c velocity snapshots for $z = [-1, 0, +1]$ are saved in a zip (.zip) file.

APPENDIX B, COST FUNCTION MINIMISATION

This appendix describes how to minimise the non-dimensional cost function of the coherent predictor. We assume that the solution is a 3rd order polynomial with unknown a_i coefficients as,

$$\sum_{j=n-m}^{n} \sum_{i=1}^{n+1} a_i . t_j^{i-1} = y_{n-m,n}. \tag{9.1}$$

We can expand the solution coefficients into the cost function as follows,

$$\begin{aligned} \mathcal{J} = \frac{1}{n} \sum_{i=1}^{n} & \left[\left(a_0 + a_1 t_i + a_2 t_i^2 + a_3 t_i^3 \right) - y_i' \right]^2 \\ & + \alpha_1' \left[\left(a_1 + 2a_2 t_i + 3a_3 t_i^2 \right) - \dot{y}_i' \right]^2 \\ & + \alpha_2' \left[(2a_2 + 6a_3 t_i) - \dot{y}_i' \right]^2 . \end{aligned} \tag{9.2}$$

The minimized solution should satisfy the partial derivative of the cost function over a_i coefficients as,

$$\frac{\partial \mathcal{J}}{\partial a_i} = 0. \tag{9.3}$$

Partials derivate of a_0 is given by,

$$\begin{aligned} \frac{\partial \mathcal{J}}{\partial a_0} = \frac{2}{n} \sum_{i=1}^{n} & \left[\left(a_0 + a_1 t_i + a_2 t_i^2 + a_3 t_i^3 \right) - y_i \right] + 0 + 0 \\ & \sum_{i=1}^{n} \left[a_0 + a_1 t_i + a_2 t_i^2 + a_3 t_i^3 \right] = y_i \end{aligned} . \tag{9.4}$$

Partial derivative of a_1 is,

$$\begin{aligned} \frac{\partial \mathcal{J}}{\partial a_1} = \frac{2}{n} \sum_{i=1}^{n} & \left[\left(a_0 + a_1 t_i + a_2 t_i^2 + a_3 t_i^3 \right) - y_i \right] \cdot t_i \\ & + 2 \cdot \left[\left(a_1 + 2a_2 t_n + 3a_3 t_n^2 \right) - \dot{y}_n \right] + 0 \end{aligned} . \tag{9.5}$$

Partial derivative of a_2 is,

$$\begin{aligned}\frac{\partial \mathcal{J}}{\partial a_2} = \frac{2}{n}\sum_{i=1}^{n}\Big[\Big(a_0 + a_1 t_i + a_2 t_i^2 + a_3 t_i^3\Big) - y_i\Big]\cdot t_i^2 \\ +2\cdot\Big[\Big(a_1 + 2a_2 t_i + 3a_3 t_i^2\Big) - \dot{y}_i\Big]\cdot(2t_i)\cdot \\ +2\cdot[(2a_2 + 6a_3 t_i) - \ddot{y}_i]\cdot(2)\end{aligned} \tag{9.6}$$

Partial derivative of a_3 is,

$$\begin{aligned}\frac{\partial \mathcal{J}}{\partial a_3} = \frac{2}{n}\sum_{i=1}^{n}\Big[\Big(a_0 + a_1 t_i + a_2 t_i^2 + a_3 t_i^3\Big) - y_i\Big]\cdot t_i^3 \\ +2\cdot\Big[\Big(a_1 + 2a_2 t_i + 3a_3 t_i^2\Big) - \dot{y}_i\Big]\cdot\Big(3t_i^2\Big)\cdot \\ +2\cdot[(2a_2 + 6a_3 t_i) - \ddot{y}_i]\cdot(6t_i)\end{aligned} \tag{9.7}$$

To linearize the solution, we set each partial derivative to zero leading. Series of partial derivatives can be written in a matrix form as,

$$\begin{aligned}&\left(\frac{1}{n}\sum_{i=1}^{n}\begin{bmatrix} t_i^6 & t_i^5 & t_i^4 & t_i^3 \\ t_i^5 & t_i^4 & t_i^3 & t_i^2 \\ t_i^4 & t_i^3 & t_i^2 & t_i \\ t_i^3 & t_i^2 & t_i & 1 \end{bmatrix} + \alpha_1{\prime}\begin{bmatrix} 9t_n^4 & 6t_n^3 & 3t_n^2 & 0 \\ 6t_n^3 & 4t_n^2 & 2t_n & 0 \\ 3t_n^2 & 2t_n & 1 & 0 \\ 0 & 0 & 0 & 0 \end{bmatrix} + \alpha_2{\prime}\begin{bmatrix} 36t_n^2 & 12t_n & 0 & 0 \\ 12t_n & 4 & 0 & 0 \\ 0 & 0 & 0 & 0 \\ 0 & 0 & 0 & 0 \end{bmatrix}\right)\begin{bmatrix} a_3 \\ a_2 \\ a_1 \\ a_0 \end{bmatrix} \\ &= \left(\frac{1}{n}\sum_{i=1}^{n}\begin{bmatrix} y_i t_i^3 \\ y_i t_i^2 \\ y_i t_i \\ y_i \end{bmatrix} + \alpha_1{\prime}\begin{bmatrix} 3\dot{y}_n t_n^2 \\ 2\dot{y}_n t_n \\ \dot{y}_n \\ 0 \end{bmatrix} + \alpha_2{\prime}\begin{bmatrix} 6\ddot{y}_n t_n \\ 2\ddot{y}_n \\ 0 \\ 0 \end{bmatrix}\right).\end{aligned} \tag{9.8}$$

On the other hand, the derived equation is in a form of $AX = B$. So a_i solutions can be solved by $X = A^{-1}B$.

BIBLIOGRAPHY

[1] D. Schanz, S. Gesemann, and A. Schröder, « Shake-The-Box: Lagrangian particle tracking at high particle image densities », *Experiments in Fluids*, vol. 57, pp. 1–27, May 2016, ISSN: 07234864. DOI: 10.1007/s00348-016-2157-1.

[2] Y. Yang and D. Heitz, « Kernelized Lagrangian particle tracking », *Experiments in Fluids*, vol. 62, *12*, pp. 1–21, Apr. 2021, ISSN: 14321114. DOI: 10.1007/s00348-021-03340-2.

[3] G. Haller, « Lagrangian coherent structures », *Annual Review of Fluid Mechanics*, vol. 47, pp. 137–162, 2015, ISSN: 00664189. DOI: 10.1146/annurev-fluid-010313-141322.

[4] S. G. Raben, S. D. Ross, and P. P. Vlachos, « Computation of finite-time Lyapunov exponents from time-resolved particle image velocimetry data », *Experiments in Fluids*, vol. 55, pp. 1–14, 2014, ISSN: 07234864. DOI: 10.1007/s00348-013-1638-8.

[5] A. Sciacchitano, B. Leclaire, and A. Schröder, « Main results of the first Lagrangian Particle Tracking Challenge », *14th International Symposium on Particle Image Velocimetry*, vol. 1, *1*, Aug. 2021, ISSN: 2769-7576. DOI: 10.18409/ispiv.v1i1.197.

[6] A. R. Khojasteh, Y. Yang, D. Heitz, and S. Laizet, « Lagrangian coherent track initialization », *Physics of Fluids*, vol. 33, *9*, p. 095 113, Sep. 2021, ISSN: 1070-6631. DOI: 10.1063/5.0060644.

[7] I. Marusic and S. Broomhall, « Leonardo da Vinci and Fluid Mechanics », *Annual Review of Fluid Mechanics*, vol. 53, pp. 1–25, Jan. 2021, ISSN: 00664189. DOI: 10.1146/annurev-fluid-022620-122816.

[8] G. I. Taylor, « The interaction between experiment and theory in fluid mechanics », *Annual Review of Fluid Mechanics*, vol. 6, pp. 1–16, 1974, ISSN: 0066-4189. DOI: 10.1146/annurev.fl.06.010174.000245.

[9] J. L. Lumley, « Some comments on turbulence », *Physics of Fluids A*, vol. 4, *2*, pp. 203–211, 1992, ISSN: 08998213. DOI: 10.1063/1.858347.

[10] M. Raffel, C. E. Willert, F. Scarano, C. J. Kähler, S. T. Wereley, and J. Kompenhans, *Particle Image Velocimetry A Practical Guide*, third. Cham: Springer International Publishing, Sep. 2018, ISBN: 978-3-319-68851-0. DOI: 10.1007/978-3-319-68852-7.

[11] C. E. Willert and J. Kompenhans, « PIV Analysis of Ludwig Prandtl's Historic Flow Visualization Films », *arXiv*, Oct. 2010. [Online]. Available: http://arxiv.org/abs/1010.3149.

[12] T. Utami and T. Ueno, « Visualization and picture processing of turbulent flow », *Experiments in Fluids*, vol. 2, *1*, pp. 25–32, Mar. 1984, ISSN: 07234864. DOI: 10.1007/BF00266315.

[13] C. E. Willert and M. Gharib, « Digital particle image velocimetry », *Experiments in Fluids*, vol. 10, *4*, pp. 181–193, 1991, ISSN: 07234864. DOI: 10.1007/BF00190388.

[14] G. E. Elsinga, F. Scarano, B. Wieneke, and B. W. Van Oudheusden, « Tomographic particle image velocimetry », *Experiments in Fluids*, vol. 41, pp. 933–947, 2006, ISSN: 07234864. DOI: 10.1007/s00348-006-0212-z.

[15] F. Scarano, *Tomographic PIV: Principles and practice*, Oct. 2013. DOI: 10.1088/0957-0233/24/1/012001.

[16] J. Westerweel, G. E. Elsinga, and R. J. Adrian, « Particle image velocimetry for complex and turbulent flows », *Annual Review of Fluid Mechanics*, vol. 45, pp. 409–436, 2013, ISSN: 00664189. DOI: 10.1146/annurev-fluid-120710-101204.

[17] H. G. Maas, A. Gruen, and D. Papantoniou, « Particle tracking velocimetry in three-dimensional flows - Part 1. Photogrammetric determination of particle coordinates », *Experiments in Fluids*, vol. 15, *2*, pp. 133–146, Jul. 1993, ISSN: 07234864. DOI: 10.1007/BF00190953.

[18] M. Novara and F. Scarano, « A particle-tracking approach for accurate material derivative measurements with tomographic PIV This article is part of the Topical Collection on Application of Laser Techniques to Fluid Mechanics 2012 », *Experiments in Fluids*, vol. 54, *8*, 2013, ISSN: 07234864. DOI: 10.1007/s00348-013-1584-5.

[19] J. F. G. Schneiders, G. C. A. Caridi, A. Sciacchitano, and F. Scarano, « Large-scale volumetric pressure from tomographic PTV with HFSB tracers », *Experiments in Fluids*, vol. 57, pp. 1–8, Nov. 2016, ISSN: 07234864. DOI: 10.1007/s00348-016-2258-x.

[20] B. Wieneke, « Iterative reconstruction of volumetric particle distribution », *Measurement Science and Technology*, vol. 24, *2*, pp. 1–14, 2012, ISSN: 13616501. DOI: 10.1088/0957-0233/24/2/024008.

[21] T. Fuchs, R. Hain, and C. J. Kähler, « Macroscopic three-dimensional particle location using stereoscopic imaging and astigmatic aberrations », 2014. DOI: 10.1364/OL.39.006863.

[22] T. Fuchs, R. Hain, and C. J. Kähler, « In situ calibrated defocusing PTV for wall-bounded measurement volumes », *Measurement Science and Technology*, vol. 27, *8*, p. 084 005, Jun. 2016, ISSN: 0957-0233. DOI: 10.1088/0957-0233/27/8/084005.

[23] K. Hoyer, M. Holzner, B. Lüthi, M. Guala, A. Liberzon, and W. Kinzelbach, « 3D scanning particle tracking velocimetry », *Experiments in Fluids*, vol. 39, *5*, pp. 923–934, Aug. 2005, ISSN: 07234864. DOI: 10.1007/s00348-005-0031-7.

[24] M. Novara, D. Schanz, N. Reuther, C. J. Kähler, and A. Schröder, « Lagrangian 3D particle tracking in high-speed flows: Shake-The-Box for multi-pulse systems », *Experiments in Fluids*, vol. 57, *8*, p. 128, 2016, ISSN: 07234864. DOI: 10.1007/s00348-016-2216-7.

[25] J. F. Schneiders and F. Scarano, « Dense velocity reconstruction from tomographic PTV with material derivatives », *Experiments in Fluids*, vol. 57, *9*, pp. 1–22, 2016, ISSN: 07234864. DOI: 10.1007/s00348-016-2225-6.

[26] T. Fuchs, R. Hain, and C. J. Kähler, « Double-frame 3D-PTV using a tomographic predictor », *Experiments in Fluids*, vol. 57, *11*, pp. 1–5, 2016, ISSN: 07234864. DOI: 10.1007/s00348-016-2247-0.

[27] S. Tan, A. Salibindla, A. U. M. Masuk, and R. Ni, « Introducing OpenLPT: new method of removing ghost particles and high-concentration particle shadow tracking », *Experiments in Fluids*, vol. 61, *2*, pp. 1–16, 2020, ISSN: 14321114. DOI: 10.1007/s00348-019-2875-2.

[28] F. Huhn, D. Schanz, P. Manovski, S. Gesemann, and A. Schröder, « Time-resolved large-scale volumetric pressure fields of an impinging jet from dense Lagrangian particle tracking », *Experiments in Fluids*, vol. 59, pp. 1–16, 2018, ISSN: 07234864. DOI: 10.1007/s00348-018-2533-0.

[29] F. Huhn, D. Schanz, S. Gesemann, U. Dierksheide, R. van de Meerendonk, and A. Schröder, « Large-scale volumetric flow measurement in a pure thermal plume by dense tracking of helium-filled soap bubbles », *Experiments in Fluids*, vol. 58, *9*, pp. 1–19, 2017, ISSN: 07234864. DOI: 10.1007/s00348-017-2390-2.

[30] S. S. Shirsath, J. T. Padding, H. J. Clercx, and J. A. Kuipers, « Cross-validation of 3D particle tracking velocimetry for the study of granular flows down rotating chutes », *Chemical Engineering Science*, vol. 134, pp. 312–323, Sep. 2015, ISSN: 0009-2509. DOI: 10.1016/J.CES.2015.05.005.

[31] J. T. Kim, D. Kim, A. Liberzon, and L. P. Chamorro, « Three-dimensional particle tracking velocimetry for turbulence applications: Case of a jet flow », *Journal of Visualized Experiments*, vol. 2016, *108*, e53745, Feb. 2016, ISSN: 1940087X. DOI: 10.3791/53745.

[32] T. Janke, R. Schwarze, and K. Bauer, « Measuring three-dimensional flow structures in the conductive airways using 3D-PTV », *Experiments in Fluids*, vol. 58, *10*, pp. 1–11, Oct. 2017, ISSN: 07234864. DOI: 10.1007/S00348-017-2407-X.

[33] T. Jahn, D. Schanz, and A. Schröder, « Advanced iterative particle reconstruction for Lagrangian particle tracking », *Experiments in Fluids*, vol. 62, *8*, p. 179, 2021, ISSN: 0723-4864. DOI: 10.1007/s00348-021-03276-7.

[34] M. Toloui, K. Mallery, and J. Hong, « Improvements on digital inline holographic PTV for 3D wall-bounded turbulent flow measurements », *Measurement Science and Technology*, vol. 28, *4*, p. 044 009, Feb. 2017, ISSN: 0957-0233. DOI: 10.1088/1361-6501/AA5C4D.

[35] Y. G. Guezennec, R. S. Brodkey, N. Trigui, and J. C. Kent, « Algorithms for fully automated three-dimensional particle tracking velocimetry », *Experiments in Fluids*, vol. 17, pp. 209–219, 1994, ISSN: 07234864. DOI: 10.1007/BF00203039.

[36] S. P. Panday, K. Ohmi, and K. Nose, « An ant colony optimization based stereoscopic particle pairing algorithm for three-dimensional particle tracking velocime-

try », *Flow Measurement and Instrumentation*, vol. 22, *1*, pp. 86–95, Mar. 2011, ISSN: 0955-5986. DOI: 10.1016/J.FLOWMEASINST.2010.12.009.

[37] Z. Dou, P. J. Ireland, A. D. Bragg, Z. Liang, L. R. Collins, and H. Meng, « Particle-pair relative velocity measurement in high-Reynolds-number homogeneous and isotropic turbulence using 4-frame particle tracking velocimetry », *Experiments in Fluids*, vol. 59, pp. 1–17, 2018, ISSN: 07234864. DOI: 10.1007/s00348-017-2481-0.

[38] D. Schanz, M. Novara, and A. Schröder, « Shake-The-Box particle tracking with variable time-steps in flows with high velocity range (VT-STB) », *3rd Workshop and 1st Challenge on Data Assimilation & CFD Processing for PIV and Lagrangian Particle Tracking*, 2020.

[39] Y. Yang and D. Heitz, « LaPIV using multigrid warping and proxy regularization », *in 14th International Symposium on Particle Image Velocimetry*, vol. 1, Paul V. Galvin Library/Illinois Institute of Technology, Aug. 2021. DOI: 10.18409/ispiv.v1i1.146.

[40] R. Humble, G. Elsinga, F. Scarano, and B. van Oudheusden, « Investigation of the Instantaneous 3D Flow Organization of a SWTBLI Using Tomographic PIV », Jun. 2007. DOI: 10.2514/6.2007-4112.

[41] F. Scarano, S. Ghaemi, G. C. A. Caridi, J. Bosbach, U. Dierksheide, and A. Sciacchitano, « On the use of helium-filled soap bubbles for large-scale tomographic PIV in wind tunnel experiments », *Experiments in Fluids*, vol. 56, pp. 1–12, Feb. 2015, ISSN: 14321114. DOI: 10.1007/s00348-015-1909-7.

[42] A. Schröder, D. Schanz, J. Bosbach, *et al.*, « Large-scale 3D flow investigations around a cyclically breathing thermal manikin in a 12 m^3 room using HFSB and STB », *14th International Symposium on Particle Image Velocimetry*, vol. 1, *1*, 2021. DOI: 10.18409/ispiv.v1i1.204.

[43] B. Leclaire, I. Mary, C. Liauzun, *et al.*, « First challenge on Lagrangian Particle Tracking and Data Assimilation: datasets description and planned evolution to an open online benchmark », *in 14th International Symposium on Particle Image Velocimetry*, Illinois, USA, 2021, pp. 1–2.

[44] M. Elagamy, « Development of 3D Turbulent Flow Reconstruction », *Thesis*, 2019.

[45] N. T. Ouellette, H. Xu, and E. Bodenschatz, « A quantitative study of three-dimensional Lagrangian particle tracking algorithms », *Experiments in Fluids*, vol. 40, pp. 301–313, 2006, ISSN: 07234864. DOI: 10.1007/s00348-005-0068-7.

[46] A. Clark, N. MacHicoane, and A. Aliseda, « A quantitative study of track initialization of the four-frame best estimate algorithm for three-dimensional Lagrangian particle tracking », *Measurement Science and Technology*, vol. 30, pp. 1–7, 2019, ISSN: 13616501. DOI: 10.1088/1361-6501/ab0786.

[47] N. A. Malik, T. Dracos, and D. A. Papantoniou, « Particle tracking velocimetry in three-dimensional flows - Part II: Particle tracking », *Experiments in Fluids*, vol. 15, pp. 279–294, Sep. 1993, ISSN: 07234864. DOI: 10.1007/BF00223406.

[48] N. Machicoane, P. D. Huck, A. Clark, A. Aliseda, R. Volk, and M. Bourgoin, « Recent Developments in Particle Tracking Diagnostics for Turbulence Research », *in Flowing Matter*, Springer, Cham, 2019, pp. 177–209, ISBN: 9783030233709. DOI: 10.1007/978-3-030-23370-9{_}6.

[49] C. Cierpka, B. Lütke, and C. J. Kähler, « Higher order multi-frame particle tracking velocimetry This article is part of the Topical Collection on Application of Laser Techniques to Fluid Mechanics 2012 », *Experiments in Fluids*, vol. 54, pp. 1–12, May 2013, ISSN: 07234864. DOI: 10.1007/s00348-013-1533-3.

[50] N. D. Cardwell, P. P. Vlachos, and K. A. Thole, « A multi-parametric particle-pairing algorithm for particle tracking in single and multiphase flows », *Measurement Science and Technology*, vol. 22, pp. 1–17, Aug. 2011, ISSN: 13616501. DOI: 10.1088/0957-0233/22/10/105406.

[51] S. Gupta and S. A. Vanapalli, « Microfluidic shear rheology and wall-slip of viscoelastic fluids using holography-based flow kinematics », *Physics of Fluids*, vol. 32, pp. 1–13, 2020, ISSN: 10897666. DOI: 10.1063/1.5135712.

[52] D. Schanz, A. Schröder, and S. Gesemann, « 'Shake The Box' - a 4D PTV algorithm: Accurate and ghostless reconstruction of Lagrangian tracks in densely seeded flows », *17th International Symposium on Applications of Laser Techniques to Fluid Mechanics*, pp. 7–10, 2014.

[53] A. Schröder, D. Schanz, D. Michaelis, C. Cierpka, S. Scharnowski, and C. J. Kähler, « Advances of PIV and 4D-PTV "shake-The-Box" for Turbulent Flow Analysis -

the Flow over Periodic Hills », *Flow, Turbulence and Combustion*, vol. 95, *2-3*, pp. 193–209, 2015, ISSN: 15731987. DOI: 10.1007/s10494-015-9616-2.

[54] D. Schanz, A. Schröder, S. Gesemann, D. Michaelis, and B. Wieneke, « ' Shake The Box ': A highly efficient and accurate Tomographic Particle Tracking Velocimetry (TOMO-PTV) method using prediction of particle positions », *in 10th International Symposium on Particle Image Velocimetry - PIV13*, Delft, The Netherlands, 2013, pp. 1–13.

[55] G. Haller and G. Yuan, « Lagrangian coherent structures and mixing in two-dimensional turbulence », *Physica D: Nonlinear Phenomena*, vol. 147, *3-4*, pp. 352–370, Dec. 2000, ISSN: 01672789. DOI: 10.1016/S0167-2789(00)00142-1.

[56] S. C. Shadden, F. Lekien, and J. E. Marsden, « Definition and properties of Lagrangian coherent structures from finite-time Lyapunov exponents in two-dimensional aperiodic flows », *Physica D: Nonlinear Phenomena*, vol. 212, *3-4*, pp. 271–304, Dec. 2005, ISSN: 01672789. DOI: 10.1016/j.physd.2005.10.007.

[57] M. A. Green, C. W. Rowley, and G. Haller, « Detection of Lagrangian coherent structures in three-dimensional turbulence », *Journal of Fluid Mechanics*, vol. 572, pp. 111–120, 2007, ISSN: 00221120. DOI: 10.1017/S0022112006003648.

[58] D. Lipinski and K. Mohseni, « A ridge tracking algorithm and error estimate for efficient computation of Lagrangian coherent structures », *Chaos*, vol. 20, *1*, 2010, ISSN: 10541500. DOI: 10.1063/1.3270049.

[59] S. Balasuriya, R. Kalampattel, and N. T. Ouellette, « Hyperbolic neighbourhoods as organizers of finite-time exponential stretching », *Journal of Fluid Mechanics*, vol. 807, pp. 509–545, 2020. DOI: 10.1017/jfm.2016.633.

[60] A. Hadjighasem, M. Farazmand, D. Blazevski, G. Froyland, and G. Haller, « A critical comparison of Lagrangian methods for coherent structure detection », *Chaos*, vol. 27, *5*, 2017, ISSN: 10541500. DOI: 10.1063/1.4982720.

[61] M. Filippi, I. I. Rypina, A. Hadjighasem, and T. Peacock, « An Optimized-Parameter Spectral Clustering Approach to Coherent Structure Detection in Geophysical Flows », *Fluids*, vol. 6, *1*, pp. 1–34, 2021, ISSN: 2311-5521. DOI: 10.3390/fluids6010039.

[62] F. A. C. Martins, A. Sciacchitano, and D. E. Rival, « Detection of vortical structures in sparse Lagrangian data using coherent-structure colouring », *Experiments in Fluids*, vol. 62, pp. 1–15, 2021. DOI: 10.1007/s00348-021-03135-5.

[63] A. Hadjighasem, D. Karrasch, H. Teramoto, and G. Haller, « Spectral-clustering approach to Lagrangian vortex detection », *Physical Review E*, vol. 93, pp. 1–17, 2016, ISSN: 24700053. DOI: 10.1103/PhysRevE.93.063107.

[64] M. Ester, H.-P. Kriegel, J. Sander, and X. Xu, « A Density-Based Algorithm for Discovering Clusters in Large Spatial Databases with Noise », *in Proceedings of the 2nd International Conference on Knowledge Discovery and Data Mining*, 1996, pp. 226–231.

[65] S. P. Lloyd, « Least Squares Quantization in PCM », *IEEE Transactions on Information Theory*, vol. 28, *2*, pp. 129–137, 1982, ISSN: 15579654. DOI: 10.1109/TIT.1982.1056489.

[66] J. Shi and J. Malik, « Normalized cuts and image segmentation », *IEEE Transactions on Pattern Analysis and Machine Intelligence*, vol. 22, *8*, pp. 888–905, 2000, ISSN: 01628828. DOI: 10.1109/34.868688.

[67] G. Bourmaud, R. Mégret, A. Giremus, and Y. Berthoumieu, « Global motion estimation from relative measurements using iterated extended Kalman filter on matrix LIE groups », *2014 IEEE International Conference on Image Processing, ICIP 2014*, vol. 22, *8*, pp. 3362–3366, 2014. DOI: 10.1109/ICIP.2014.7025680.

[68] G. C. A. Caridi, D. Ragni, A. Sciacchitano, and F. Scarano, « HFSB-seeding for large-scale tomographic PIV in wind tunnels », *Experiments in Fluids*, vol. 57, *12*, p. 190, Dec. 2016, ISSN: 07234864. DOI: 10.1007/s00348-016-2277-7.

[69] B. Gibeau and S. Ghaemi, « A modular, 3D-printed helium-filled soap bubble generator for large-scale volumetric flow measurements », *Experiments in Fluids*, vol. 59, *12*, p. 178, Dec. 2018, ISSN: 07234864. DOI: 10.1007/s00348-018-2634-9.

[70] B. Gibeau, D. Gingras, and S. Ghaemi, « Evaluation of a full-scale helium-filled soap bubble generator », *Experiments in Fluids*, vol. 61, *2*, p. 28, Feb. 2020, ISSN: 14321114. DOI: 10.1007/s00348-019-2853-8. [Online]. Available: https://doi.org/10.1007/s00348-019-2853-8.

[71] P. K. Stansby, « The effects of end plates on the base pressure coefficient of a circular cylinder », *The Aeronautical Journal*, vol. 78, *757*, pp. 36–37, 1974, ISSN: 0001-9240. DOI: 10.1017/S0001924000036319.

[72] B. Lecordier and J. Westerweel, « The EUROPIV Synthetic Image Generator (S.I.G.) », *in Particle Image Velocimetry: Recent Improvements*, 2004, pp. 145–161. DOI: 10.1007/978-3-642-18795-7{_}11.

[73] F. Huhn, A. Schröder, D. Schanz, S. Gesemann, and P. Manovski, « Estimation of time-resolved 3D pressure fields in an impinging jet flow from dense Lagrangian particle tracking », *in 18th International Symposium on Flow Visualization*, Zurich, Switzerland, Jun. 2018, pp. 1–14. DOI: 10.3929/ethz-b-000279200.

[74] M. Bobrov, M. Hrebtov, V. Ivashchenko, *et al.*, « Pressure evaluation from Lagrangian particle tracking data using a grid-free least-squares method », *Measurement Science and Technology*, vol. 32, *084014*, pp. 1–14, May 2021, ISSN: 13616501. DOI: 10.1088/1361-6501/abf95c.

[75] D. Puzyrev, K. Harth, T. Trittel, and R. Stannarius, « Machine Learning for 3D Particle Tracking in Granular Gases », *Microgravity Science and Technology*, vol. 32, *5*, pp. 897–906, Oct. 2020, ISSN: 18750494. DOI: 10.1007/s12217-020-09800-4.

[76] Y. Gim, D. K. Jang, D. K. Sohn, H. Kim, and H. S. Ko, « Three-dimensional particle tracking velocimetry using shallow neural network for real-time analysis », *Experiments in Fluids*, vol. 61, *2*, pp. 1–8, Feb. 2020, ISSN: 14321114. DOI: 10.1007/s00348-019-2861-8.

[77] Y. J. Jeon, M. Müller, D. Michaelis, and B. Wieneke, « Data assimilation-based flow field reconstruction from particle tracks over multiple time steps », *in 13th International Symposium on Particle Image Velocimetry*, 2019, pp. 1–8.

[78] S. Discetti and F. Coletti, « Volumetric velocimetry for fluid flows », *Measurement Science and Technology*, vol. 29, *4*, pp. 1–26, Mar. 2018, ISSN: 13616501. DOI: 10.1088/1361-6501/aaa571.

[79] S. Laizet and E. Lamballais, « High-order compact schemes for incompressible flows: A simple and efficient method with quasi-spectral accuracy », *Journal of Computational Physics*, vol. 228, pp. 5989–6015, 2009, ISSN: 10902716. DOI: 10.1016/j.jcp.2009.05.010.

[80] S. Laizet and N. Li, « Incompact3d: A powerful tool to tackle turbulence problems with up to O(105) computational cores », *International Journal for Numerical*

Methods in Fluids, vol. 67, pp. 1735–1757, Dec. 2011, ISSN: 02712091. DOI: 10.1002/fld.2480.

[81] D. Michaelis, C. Poelma, F. Scarano, J. Westerweel, and B. Wieneke, « A 3D Time-resolved cylinder wake survey by Tomographic PIV », *in 12th International Symposium on Flow Visualisation*, 2006, pp. 1–11.

[82] C. He and Y. Liu, « Proper orthogonal decomposition-based spatial refinement of TR-PIV realizations using high-resolution non-TR-PIV measurements », *Experiments in Fluids*, vol. 58, pp. 1–22, 2017, ISSN: 07234864. DOI: 10.1007/s00348-017-2371-5.

[83] A. Booysen, P. Das, and S. Ghaemi, « Shake-the-Box PTV in the Wake of an Ahmed Body Using Helium Filled Soap Bubbles », *in 13th International Symposium on Particle Image Velocimetry*, 2019, pp. 301–310.

[84] A. Schröder, C. E. Willert, D. Schanz, *et al.*, « The flow around a surface mounted cube: a characterization by time-resolved PIV, 3D Shake-The-Box and LBM simulation », *Experiments in Fluids*, vol. 61, pp. 1–22, Sep. 2020, ISSN: 14321114. DOI: 10.1007/s00348-020-03014-5.

[85] T. W. Fahringer, K. P. Lynch, and B. S. Thurow, « Volumetric particle image velocimetry with a single plenoptic camera », *Measurement Science and Technology*, vol. 26, pp. 1–25, Sep. 2015, ISSN: 13616501. DOI: 10.1088/0957-0233/26/11/115201.

[86] Cfdforpiv.dlr.de, *3rd Workshop and 1st Challenge on Data Assimilation & CFD Processing for PIV and Lagrangian Particle Tracking*, 2020. [Online]. Available: http://cfdforpiv.dlr.de/.

[87] M. Miozzi, A. Capone, C. Klein, and F. D. Felice, « Integrating high-frequency , time resolved TSP surface maps and wake flow Lagrangian description to investigate sub critical regime in a crossflow cylinder », *in 11th International Symposium on Particle Image Velocimetry*, 2015, pp. 1–6.

[88] Z. Sun and C. Brücker, « Investigation of the vortex ring transition using scanning Tomo-PIV », *Experiments in Fluids*, vol. 58, *4*, p. 36, 2017, ISSN: 07234864. DOI: 10.1007/s00348-017-2322-1.

[89] N. J. Neeteson, S. Bhattacharya, D. E. Rival, D. Michaelis, D. Schanz, and A. Schröder, « Pressure-field extraction from Lagrangian flow measurements: first experiences with 4D-PTV data », *Experiments in Fluids*, vol. 57, pp. 1–18, 2016, ISSN: 07234864. DOI: 10.1007/s00348-016-2170-4.

[90] D. Violato and F. Scarano, « Three-dimensional evolution of flow structures in transitional circular and chevron jets », *Physics of Fluids*, vol. 23, *12*, pp. 1–25, 2011, ISSN: 10706631. DOI: 10.1063/1.3665141.

[91] R. Hain, C. J. Kähler, and D. Michaelis, « Tomographic and time resolved PIV measurements on a finite cylinder mounted on a flat plate », *Experiments in Fluids*, vol. 45, pp. 715–724, 2008, ISSN: 07234864. DOI: 10.1007/s00348-008-0553-x.

[92] M. Patel, S. E. Leggett, A. K. Landauer, I. Y. Wong, and C. Franck, « Rapid, topology-based particle tracking for high-resolution measurements of large complex 3D motion fields », *Scientific Reports*, vol. 8, pp. 1–14, 2018, ISSN: 20452322. DOI: 10.1038/s41598-018-23488-y.

[93] C. He, Y. Liu, and L. Gan, « Instantaneous pressure determination from unsteady velocity fields using adjoint-based sequential data assimilation », *Physics of Fluids*, vol. 32, pp. 1–15, 2020, ISSN: 10897666. DOI: 10.1063/1.5143760.

[94] S. Krishna, M. A. Green, and K. Mulleners, « Flowfield and force evolution for a symmetric hovering flat-plate wing », *AIAA Journal*, vol. 56, pp. 1360–1371, 2018, ISSN: 00011452. DOI: 10.2514/1.J056468.

[95] X. Ma, Z. Tang, and N. Jiang, « Eulerian and Lagrangian analysis of coherent structures in separated shear flow by time-resolved particle image velocimetry », *Physics of Fluids*, vol. 32, pp. 1–12, 2020, ISSN: 10897666. DOI: 10.1063/5.0008664.

[96] S. Rafati and N. T. Clemens, « Frameworks for investigation of nonlinear dynamics: Experimental study of the turbulent jet », *Physics of Fluids*, vol. 32, pp. 1–18, 2020, ISSN: 10897666. DOI: 10.1063/5.0014939.

[97] S. Qin, H. Liu, and Y. Xiang, « On the formation modes in vortex interaction for multiple co-axial co-rotating vortex rings », *Physics of Fluids*, vol. 30, pp. 1–15, 2018, ISSN: 10897666. DOI: 10.1063/1.4998698.

[98] T. K. Alligood, D. T. Sauer, and A. J. Yorke, « CHAOS: An Introduction to Dynamical Systems », *Springer*, pp. 193–228, 1996. DOI: 10.1201/b16036-23.

[99] A. R. Khojasteh, D. Heitz, Y. Yang, and S. Laizet, « Lagrangian Coherent Track Initialisation », *in 3rd Workshop and 1st Challenge on Data Assimilation & CFD Processing for PIV and Lagrangian Particle Tracking*, 2020.

[100] S. Tan, A. Salibindla, A. Ullah, and M. Masuk, « An open-source Shake-the-Box method and its performance evaluation », *in 13th International Symposium on Particle Image Velocimetry*, vol. i, 2019.

[101] A. Schröder, D. Schanz, R. Geisler, S. Gesemann, and C. E. Willert, « Near-wall turbulence characterization using 4D-PTV Shake-The-Box », *in 11th International Symposium on Particle Image Velocimetry*, 2015.

[102] T. Knopp, N. Reuther, M. Novara, *et al.*, « Experimental analysis of the log law at adverse pressure gradient », *Journal of Fluid Mechanics*, vol. 918, p. 17, 2021, ISSN: 14697645. DOI: 10.1017/jfm.2021.331.

[103] J. Heyman, « TracTrac: A fast multi-object tracking algorithm for motion estimation », *Computers and Geosciences*, vol. 128, *February*, pp. 11–18, 2019, ISSN: 00983004. DOI: 10.1016/j.cageo.2019.03.007.

[104] C. J. Kähler, T. Astarita, P. P. Vlachos, *et al.*, « Main results of the 4th International PIV Challenge », *Experiments in Fluids*, vol. 57, *6*, pp. 1–71, 2016, ISSN: 07234864. DOI: 10.1007/s00348-016-2173-1.

[105] T. Janke, R. Schwarze, and K. Bauer, « Part2Track: A MATLAB package for double frame and time resolved Particle Tracking Velocimetry », *SoftwareX*, vol. 11, p. 100 413, Jan. 2020, ISSN: 23527110. DOI: 10.1016/j.softx.2020.100413.

[106] A. R. Khojasteh, D. Heitz, Y. Yang, and L. Fiabane, « Particle position prediction based on Lagrangian coherency for flow over a cylinder in 4D-PTV », *in 14th International Symposium on Particle Image Velocimetry*, Illinois, USA, 2021, pp. 1–9.

[107] B. Viggiano, T. Basset, S. Solovitz, *et al.*, « Lagrangian diffusion properties of a free shear turbulent jet », *Journal of Fluid Mechanics*, vol. 918, p. 25, 2021, ISSN: 14697645. DOI: 10.1017/jfm.2021.325.

[108] G. I. Taylor, « Diffusion by continuous movements », *Proceedings of the London Mathematical Society*, vol. s2-20, *1*, pp. 196–212, Jan. 1922, ISSN: 1460244X. DOI: 10.1112/plms/s2-20.1.196.

[109] G. K. Batchelor, « Diffusion in free turbulent shear flows », *Journal of Fluid Mechanics*, vol. 3, *1*, pp. 67–80, 1957, ISSN: 14697645. DOI: 10.1017/S0022112057000488.

[110] Y. J. Jeon, J. F. Schneiders, M. Müller, D. Michaelis, and B. Wieneke, « 4D flow field reconstruction from particle tracks by VIC+ with additional constraints and multigrid approximation », *18th International Symposium on Flow Visualization*, 2018.

[111] N. T. Ouellette, « Extending the reach of Lagrangian analysis in turbulence », *Journal of Fluid Mechanics*, vol. 924, p. 1, 2021, ISSN: 14697645. DOI: 10.1017/jfm.2021.493.

[112] B. L. Sawford, « Reynolds number effects in Lagrangian stochastic models of turbulent dispersion », *Physics of Fluids A*, vol. 3, *6*, pp. 1577–1586, 1991, ISSN: 08998213. DOI: 10.1063/1.857937.

[113] B. Wieneke and K. Pfeiffer, « Adaptive PIV with variable interrogation window size and shape », *in 15th International Symposium on Applications of Laser Techniques to Fluid Mechanics*, Lisbon, 2010.

[114] R. Theunissen, F. Scarano, and M. L. Riethmuller, « An adaptive sampling and windowing interrogation method in PIV », *in Measurement Science and Technology*, vol. 18, Institute of Physics Publishing, Jan. 2007, pp. 275–287. DOI: 10.1088/0957-0233/18/1/034.

[115] B. K. Horn and B. G. Schunck, « Determining optical flow », *Artificial Intelligence*, vol. 17, *1-3*, pp. 185–203, 1981, ISSN: 00043702. DOI: 10.1016/0004-3702(81)90024-2.

[116] R. Schuster, D. Heitz, and E. Mémin, « Motion Estimation Under Location Uncertainty, Application To Large-Scale Characterization Of A Mixing Layer », *in 19th International Symposium on the Application of Laser and Imaging Techniques to Fluid Mechanics*, 2018, pp. 16–19.

[117] S. C. Shadden, J. O. Dabiri, and J. E. Marsden, « Lagrangian analysis of fluid transport in empirical vortex ring flows », *Physics of Fluids*, vol. 18, *4*, pp. 1–11, 2006, ISSN: 10706631. DOI: 10.1063/1.2189885.

[118] K. Onu, F. Huhn, and G. Haller, « LCS Tool: A computational platform for Lagrangian coherent structures », *Journal of Computational Science*, vol. 7, pp. 26–36, 2015, ISSN: 18777503. DOI: 10.1016/j.jocs.2014.12.002.

[119] D. Heitz, E. Mémin, and C. Schnörr, « Variational fluid flow measurements from image sequences: synopsis and perspectives », *Experiments in Fluids*, *3*, p. 48, 2010. DOI: 10.1007/s00348-009-0778-3.

[120] P. Godbersen and A. Schröder, « Functional binning: Improving convergence of Eulerian statistics from Lagrangian particle tracking », *Measurement Science and Technology*, vol. 31, *9*, p. 13, 2020, ISSN: 13616501. DOI: 10.1088/1361-6501/ab8b84.

[121] E. v. Sebille, S. M. Griffies, R. Abernathey, *et al.*, « Lagrangian ocean analysis: Fundamentals and practices », *Ocean Modelling*, vol. 121, pp. 49–75, Jan. 2018, ISSN: 14635003. DOI: 10.1016/j.ocemod.2017.11.008.

[122] Y. Li, E. Perlman, M. Wan, *et al.*, « A public turbulence database cluster and applications to study Lagrangian evolution of velocity increments in turbulence », *Journal of Turbulence*, vol. 9, *31*, pp. 1–29, Jan. 2008, ISSN: 14685248. DOI: 10.1080/14685240802376389.

[123] P. Chandramouli, D. Heitz, S. Laizet, and E. Mémin, « Coarse large-eddy simulations in a transitional wake flow with flow models under location uncertainty », *Computers and Fluids*, vol. 168, pp. 170–189, 2018, ISSN: 00457930. DOI: 10.1016/j.compfluid.2018.04.001.

[124] A. R. Khojasteh, S. Laizet, D. Heitz, and Y. Yang, « Lagrangian and Eulerian dataset of the wake downstream of a smooth cylinder at a Reynolds number equal to 3900 », *Data in Brief*, vol. 40, 2022, ISSN: 23523409. DOI: 10.1016/j.dib.2021.107725.

[125] R. M. Samelson, « Lagrangian motion, coherent structures, and lines of persistent material strain », *Annual Review of Marine Science*, vol. 5, pp. 137–163, 2012, ISSN: 19411405. DOI: 10.1146/annurev-marine-120710-100819.

[126] P. Bartholomew, G. Deskos, R. A. Frantz, F. N. Schuch, E. Lamballais, and S. Laizet, « Xcompact3D: An open-source framework for solving turbulence problems on a Cartesian mesh », *SoftwareX*, vol. 12, pp. 1–9, Jul. 2020, ISSN: 23527110. DOI: 10.1016/j.softx.2020.100550.

Alphabetical Reference Index

N

O

P

Q

R

S

T

U

NOMENCLATURE

Abbreviations and Acronyms

ppη^3 particles per cubic Kolmogorov scale

ppD^3 particles per cubic Integral scale

4BE four frame best estimate

CCD charge coupled device

DBSCAN density based spatial clustering of applications with noise

DNS direct numerical simulation

DPIV digital particle image velocimetry

ETI enhance track initialisation

FFT fast Fourier transform

FIR finite impulse response

FTLE finite-time Lyapunov exponent

GUI graphic user interface

HFSB helium filled soap bubbles

HIT homogeneous isotropic turbulent

HWA hot wire anemometry

IBM immersed boundary method

IPR iterative particle reconstruction

IW interrogation winow

KLPT kernelized Lagrangian particle tracking

LCS Lagrangian coherent structure

LCTI Lagrangian coherent track initialisation

LDA laser Doppler anemometry

LDV laser Doppler velocimetry

LED light emitting diode

LOS line of sights

LPT Lagrangian particle tracking

MC-UQ Monte Carlo uncertainty quantification

Nd:YAG Neodym-YAG

NNI nearest neighbour initialisation

NN nearest neighbour

NR noise ratio

OFCE optical flow Constraint equation

OTF optical transfer function

pdf probability density function

PIV particle image velocimetry

ppp particles per pixel

PTV particle tracking velocimetry

RMS root mean square

sCMOS scientific CMOS

SIG synthetic image generator

STB shake the box

VIC vortex-in-cell

VSC volume-self-calibration

Greek

α	cost function weight
$\delta\mathbf{x}$	vector displacement
$\mathbf{\Delta}$	right Cauchy-Green tensor
ℓ	order of predictor function
ϵ	estimation error
η	Kolmogorov length scale
$\mathbf{\Lambda}$	FTLE value
$\mathbf{\Phi}$	particle flow map
$\sigma_{\mathbf{u}}$	Reynolds stress
σ	uncertainty level
$\tau_{\mathbf{p}}$	response time
τ_η	Kolmogorov time scale
$\varepsilon_{\mathbf{i}}$	turbulent dissipation rate
$\varepsilon_{\mathbf{u_x}}$	turbulent dissipation rate

Symbols

$\mathcal{J}$	cost function
$\tilde{\mathbf{u}}$	stationarised velocity
$\mathbf{a}$	predictor coefficients
$\mathbf{C_0}$	Lagrangian universal constant
$\mathbf{dt}$	time step
$\mathbf{D}$	integral length scale
$\mathbf{I}$	image intensity
$\mathbf{L_E}$	Eulerian integral length scale
$\mathbf{l}$	Taylor length scale
$\mathbf{R^L_{uu}}$	Lagrangian two-point correlation function
$\mathbf{Re}$	Reynolds number
$\mathbf{S^L_2}$	Lagrangian second order structure-function
$\mathbf{t_0}$	first time step
$\mathbf{T_D}$	integral time scale
$\mathbf{T_E}$	Eulerian integral time scale
$\mathbf{T}$	interval time
$\mathbf{t}$	time step
$\mathbf{U}_\infty$	freestream velocity
$\mathbf{U}$	flow velocity vector
$\mathbf{x}, \mathbf{y}, \mathbf{z}$	coordinate system
$\mathbf{y_i}$	measurement observed positions

UNIVERSITÉ DE RENNES 1

Titre : Mouvements cohérents lagrangiens pour suivre les trajectoires des particules dans les écoulements turbulents

Mot clés : Vélocimétrie par suivi de particules, structures cohérentes lagrangiennes, mouvements cohérents lagrangiens

Résumé : Dans cette thèse, nous avons étudié comment la cohérence temporelle et spatiale des particules lagrangiennes peut améliorer l'efficacité des algorithmes de suivi. Nous avons contraint l'algorithme à suivre l'information basée sur la physique des mouvements cohérents puisque les particules traceuses lagrangiennes se déplacent localement et se comportent de manière cohérente avec leurs voisins. Nous avons utilisé le concept de structures cohérentes lagrangiennes (LCS) sur des trajectoires lagrangiennes éparses pour déterminer les mouvements cohérents locaux des flux turbulents. Les LCS présentent des crêtes de ligne/surface (frontières) dans les écoulements 2D/3D qui séparent les régions d'écoulement ayant des trajectoires dynamiquement différentes. Par conséquent, nous pouvons quantifier les trajectoires cohérentes et non cohérentes des voisins en fonction des crêtes LCS. Dans cette thèse, l'idée d'utiliser les mouvements cohérents locaux des particules lagrangiennes a été discutée dans trois algorithmes de vélocimétrie. Nous avons montré comment les mouvements cohérents peuvent augmenter la robustesse des techniques d'initialisation des trajectoires. Ensuite, l'idée a été employée pour améliorer la performance de la prédiction. Enfin, l'approche proposée a été adpatée et appliquée aux algorithmes classiques de PIV.

Title: Lagrangian coherent motions to track particle trajectories in turbulent flows

Keywords: Particle Tracking Velocimetry, Lagrangian Coherent Structures, Coherent motions

Abstract: We present here a study that attempts to improve velocimetry algorithms by using the temporal and spatial coherency of Lagrangian particles. As Lagrangian tracer particles move and behave coherently with their neighbours, we constrained the algorithm to comply with physics-based information. In order to determine local coherent motions of turbulent flows, we utilized Lagrangian Coherent Structures (LCS) over sparse Lagrangian trajectories. In 2D/3D flows, LCS has line/-surface ridges separating regions with dynamically different trajectories. Based on LCS ridges, we can quantify coherent and non-coherent neighbour trajectories. Three velocimetry algorithms are discussed in this thesis using the idea of local coherent motions of Lagrangian particles. Through coherent motions, we demonstrated how the track initialization techniques in time-resolved three-dimensional particle tracking velocimetry (4D-PTV) can become more robust. This idea was then used to improve prediction performance. We also explored how to apply this approach to classic PIV algorithms.